UCLA
UCLA Electronic Theses and Dissertations

Title
Achieving High Efficiency Organic Solar Cells by Device Structure Engineering

Permalink
https://escholarship.org/uc/item/5tp535t9

Author
Chang, Sheng-Yung

Publication Date
2019

Peer reviewed|Thesis/dissertation

eScholarship.org Powered by the California Digital Library
University of California

UNIVERSITY OF CALIFORNIA

Los Angeles

Achieving High Efficiency Organic Solar Cells by Device Structure Engineering

A dissertation submitted in partial satisfaction of the

requirements for the degree Doctor of Philosophy

in Materials Science and Engineering

by

Sheng-Yung Chang

2019

© Copyright by

Sheng-Yung Chang

2019

ABSTRACT OF THE DISSERTATION

Achieving High Efficiency Organic Solar Cells by Charge Transport layer Engineering

by

Sheng-Yung Chang

Doctor of Philosophy in Materials Science and Engineering

University of California, Los Angeles, 2019

Professor Dwight C. Streit, Co-Chair

Professor Yang Yang, Co-Chair

Photovoltaics technology, or solar cell, has been developed for more than a half century. This idea that utilizes energy from an infinite resource is indeed fascinating and drives scientists and engineers to devote themselves to this field. It is one of the major renewable energy types which accounts for 2% of the global total electricity consumption in 2018 and this percentage is still growing in a steady trend. According to a publicized prediction, the solar power could supply 20% of the total electricity demand in 2030 because of drastically dropping price per watt. Although a brilliant future of solar cell is projected, there are still many unknown physical phenomena and engineering difficulties nonetheless. These challenges in photovoltaics are thus of our interest to work on.

The state of art highest efficiency photovoltaics is multi-junction inorganic solar cell, which is used in astronautic application. Yet the complicated fabrication processes and high cost limit its usage. It is the reason that silicon solar cell with moderate efficiency and process rules

the whole solar cell market. However, the world still needs a different type of solar cell to fulfill the requirements of low weight, flexible, transparent, non-toxic and solution process compatibility to accustom to the other environment conditions. Organic solar cell is one of the strong candidates for reaching this target.

In this dissertation, I aim to achieve high efficiency organic solar cells in single-junction and multi-junction structure with different strategies. There are the modification of charge transport layer and interconnecting layer for a better Ohmic contact and fermi level pining as well as the sub-cell current matching by third photo-active component.

In Chap. 3, the project for improving the transport properties of single junction devices has been explored. A high mobility Indium Oxide In_2O_3 as an universal electron transport layer was chosen and improved the original device efficiencies for 10%. The physical fundamentals for efficiency improvement have been found that the crystalline In_2O_3 with highly aligned nanocrystallites can induce the crystallization of polymer into a preferential molecular packing for the charge transport and the charge extraction in the crystalline In_2O_3 devices is significantly faster than its counterpart devices.

Based on the work principle of Fermi level pinning, organic tandem solar cells with a tunnel junction consisted of zirconium (IV) acetylacetonate (Zr-Acac) has been developed and discussed in Chap. 4. The Zr-Acac has a suitable low work function to pin the Fermi level of the interconnecting layer and hence, can effectively behave as the charge recombination function for the tandem device. Furthermore, Zr-Acac requires a least harmful preparation process method in the tandem devices. Comparing to the reference device, the Zr-Acac interconnecting layer can effectively enhance the efficiency by 20%.

The other strategies to improve the tandem organic solar cells with the ternary structure have been discussed in Chap. 5 and Chap. 6. Broadening the light absorption spectrum needs the optimization of current matching among different sub-cells with good interconnecting layer. Herein, it is firstly discovered that using ternary blend sub-cell in tandem device can finely optimize the current matching via tuning the materials composition in the ternary blend. The voltage-current trade-off in the tandem devices can be achieved. Due to the amorphous nature of the used small molecular, the phase separation in this ternary blend upon heating is sufficiently suppressed, resulting in a good thermal stability and viable for a better environment of interconnecting layer preparation.

The device efficiency measured in the lab has reached 13% and the certified device efficiency is 11.5% by NREL, which achieves the world record as of October 2018.

My conclusion and future perspective of these works on organic solar cells are summarized in Chap. 7.

The dissertation of Sheng-Yung Chang is approved.

Xiangfeng Duan

Dwight C. Streit, Committee Co-Chair

Yang Yang, Committee Co-Chair

University of California, Los Angeles

2019

To my family for their love

and pursuit of higher education opportunities for me

Table of Content

Chapter 1 Introduction **1**

1.1 Development History of Solar Cells **2**

1.2 Working Principles of Solar Cells **4**

1.3 Overview of Thin Film Solar Cells **7**

1.4 Organic Solar Cells **8**

1.5 Challenges for Organic Solar Cells **11**

1.5.1 Transport of Exciton and Charge Carriers 11

1.5.2 Shockley−Queisser limit ..... **Error! Bookmark not defined.**

1.5.3 Absorption Spectrum ..... **Error! Bookmark not defined.**

References **16**

Chapter 2 Principles for Enhancing Power Conversion Efficiency **19**

2.1 Fermi Level Pinning by Interface Modification **20**

2.2 Enhancing Absorption Spectrum by Using Tandem Solar Cells **23**

2.3 Enhancing Absorption Spectrum by Using Ternary Solar Cells **24**

2.4 Organic Tandem Solar Cells **27**

2.5 Challenges **29**

References **31**

Chapter 3 High Mobility Indium Oxide Electron Transport Layer in Organic Photovoltaics **33**

3.1 Motivation **35**

3.2 Result and discussion **36**

3.2.1 Optical Property and Crystallographic Analysis of In_2O_3 Thin Film 36

3.2.2 Electrical Properties of Indium Oxide Thin Films 40

3.2.3 Device Performances 42

3.2.4 Device Transport Properties Analysis by Crystallographic Data 47
3.2.5 Mobility Analysis of Electron Transport Layers 52
3.3 Summary 55
3.4 Experimental method 56
3.4.1 Chemicals 56
3.4.2 Device Preparation 56
3.4.3 Device Characterization 57
References 59
Chapter 4 High-Efficiency Organic Tandem Solar Cells with Effective Transition Metal Chelates Interconnecting Layer 63
4.1 Motivation 64
4.2 Result and discussion 66
4.2.1 Wide and Low Bandgap Photoactive Materials 66
4.2.2 Physical Properties of Transport Materials 70
4.2.3 Light Field Simulation for Optimized Tandem Devices 74
4.2.4 Solar Cells Performance 76
4.3 Summary 79
4.4 Experimental method 80
4.4.1 Chemicals 80
4.4.2 Device Preparation 80
4.4.3 Device Characterization 81
References 83
Chapter 5 Chapter 5 High Performance Organic Tandem Solar Cells Based on Ternary Sub-Cells 86
5.1 Motivation 87

5.2 Result and discussion **88**

5.2.1 Active Layer Materials for Tandem Solar Cell 88

5.2.2 Morphological Analysis of Fullerene and Non-Fullerene Acceptors 91

5.2.3 Current Matching Design of The Front Cell 93

5.2.4 Morphological Analysis of Third Component in Active Layer 96

5.3 Summary **102**

5.4 Experimental Design Method **104**

5.4.1 Chemicals 104

5.4.1 Device fabrication 104

5.4.3 Characterization 105

References **106**

Chapter 6 Chapter 6 High Performance Organic Tandem Solar Cells Based on Ternary Sub-Cells-2 ..... **107**

6.1 Motivation **108**

6.2 Result and discussion **108**

6.2.1 Front and Rear Sub-cells for Tandem Solar Cell 108

6.2.2 Molecular Packing Behaviors of the Active Materials 112

6.2.3 Current Matching Design of The Tandem Solar Cells 115

6.2.4 Simulation Results of Tandem Solar Cells 120

6.3 Summary **121**

6.4 Experimental Design Method **122**

6.4.1 Chemicals 122

6.4.1 Device fabrication 122

6.4.3 Characterization 123

References **126**

Chapter 7 Conclusion and Future Outlooks 129

References 132

List of Figures

Figure 1-1 The energy efficiency chart by National Renewable Energy Laboratory.[4] 4

Figure 1-2 Basic solar cell device structure.[5] 6

Figure 1-3 Current-Voltage (I-V) characteristics of an typical solar cell under illumination. 6

Figure 1-4 The operating mechanism of a polymer solar cell.[10]**Error! Bookmark not defined.**

Figure 1-5 Conceptual morphology model with bicontinuous interpenetration network of the polymer and the acceptor.[10] 12

Figure 1-6 Theoretical Shockley-Queisser detailed-balance efficiency limit as a function of band gap (black line) and 75% and 50% of the limit (gray lines). The record efficiencies for different materials are plotted for the corresponding band gaps.[20] 14

Figure 2-1 Energy level alignment at the interface of TMO and C60. HOMO edge offset (ΔEH) of C60 is plotted against the work function (Φsub) of underlying TMOs. Three regimes can be identified. The energy positions of key parameters in each scenario are shown in the schematics beside each region. [5] 21

Figure 2-2 (a) Current density–voltage characteristics of a PEDOT:PSS/Spiro-TAD/MoO3 hole-only device with and without a TCTA (5 nm) interlayer between the Spiro-TAD (163 nm) transport layer and MoO3. Negative bias corresponds to hole injection from the PEDOT:PSS, positive bias to hole injection from MoO3. The inset shows the molecular structure of Spiro-TAD. (b) Schematic energy-band diagram showing the effective injection

barrier (φ b) between MoO3and the hole-transport layer (HTL). Introducing an interlayer (IL) with a higher IE realigns the Fermi level with the IE of the HTL. [Nature Materials., 2018, 17, 329..... 22

Figure 2-3 The comparison of thermal loss and spectrum loss issues in single and tandem solar cells.. 24

Figure 2-4 Schematic diagrams of different models for charge transfer. [12]..... 25

Figure 2-4 Simplified band diagram of a tandem cell made of two sub-cells connected in series via a recombination layer. [16] 28

Figure 3-1 Molecular structure of PTB7-Th, $PC_{71}BM$, and IEICO-4F. (b) Schematic of the inverted organic solar cell based on a structure of ITO/In_2O_3/PEIE/active layer/MoO_3/Ag. .....**Error! Bookmark not defined.**

Figure 3-2 Optical properties and morphology of In_2O_3 thin film. (a) Transmittance spectra of c-In_2O_3 film on the glass substrate. (b) Scanning electron microscope (SEM) image of c-In_2O_3 film on the ITO coated glass. (c) Lab-based X-ray diffraction (XRD) spectra of the c-In_2O_3 film. (d) Grazing incidence wide-angle X-ray scattering (GIWAXS) pattern of the c-In2O3 film.....**Error! Bookmark not defined.**

Figure 3-3 Electrical properties of In2O3 thin film. (a) Electrical performance of c-In_2O_3 thin-film transistors (TFT). The device structure is bottom-gate and top-contact, and the c-In_2O_3 thin film is annealed at 300 °C, (b) The saturation mobility of In_2O_3 TFT as a function of annealing temperature. (c) X-ray photoelectron spectroscopy (XPS) O 1s spectra of c-In_2O_3 and a-In_2O_3. (d) Ultraviolet photoelectron spectroscopy (UPS) spectra of c-In2O3 modified with and without PEIE. 41

Figure 3-4 Device performance of PTB7-Th–$PC_{71}BM$ organic solar cells based on various ETLs: ZnO, c-In_2O_3, and a-In_2O_3. (a) Current density–voltage (J-V) curve and (b) external quantum efficiency (EQE) spectra.....**Error! Bookmark not defined.**

Figure 3-5 Power conversion efficiency of organic solar cells based on the In_2O_3 ETL with different annealing temperatures.....**Error! Bookmark not defined.**

Figure 3-6 Device performance of PTB7-Th:IEICO-4F organic solar cells based on various ETLs: ZnO, c-In_2O_3 and a-In_2O_3. (a) Current density-voltage (J-V) curve and (b) external quantum efficiency (EQE) spectra.....**Error! Bookmark not defined.**

Figure 3-7 2D GIWAXS scattering patterns of PTB7-Th–$PC_{71}BM$ blend on different ETLs: (a) ZnO, (b) c-In_2O_3, and (c) a-In_2O_3. (d) Pole figures of the polymer (100) peak..... 49

Figure 3-8 Line scattering profiles of blend based on different ELTs cut from 2D GIWAXS patterns: (a) out-of-plane (OOP) direction and (b) in-plane (IP) direction..... 51

Figure 3-9 Photocurrent decay of organic solar cells based on three different ETLs: ZnO, c-In_2O_3, and a-In_2O_3 undrr light illumination. 53

Figure 4-1 (a) Normalized UV–vis absorption spectra of PBDTTBO and PDTP-DFBT thin films. (b) Schematic of device structure. (c) Band diagram of PBDTTBO and PDTP-DFBT tandem solar cells. 67

Figure 4-2 (a) The structure of inverted single junction device. (b) (c) The J-V curves of PBDTTBO:$PC_{71}BM$ and PDTP-DFBT:$PC_{71}BM$ devices with different active layer thickness..... 68

Figure 4-3 (a) The chemical structure of Zr-Acac and (b) transmittance comparison of Zr-Acac and ZnO thin film. (c) Ultraviolet photoelectron spectroscopy (UPS) of Zr-Acac thin film on ITO glass substrate..... 71

Figure 4-4 AFM and SEM images of thin films of (a and c) ZnO nano particle and (b and d) Zr‐Acac..... 72

Figure 4-5 Grazing incident wide angle X-ray scattering patterns of PDTP-DFBT/$PC_{71}BM$ on substrate of (a) ZnO and (b) Zr-Acac. (c) 1D profile cut from 2D scattering pattern along the out-of-plane (OOP) direction. 74

Figure 4-6 The light field simulation (Left) Light field distribution and (Right) generation current of active layer for (a) 80 and 130 nm (b) 100 and 100 nm (c) 130 and 80 nm . **Error! Bookmark not defined.**

Figure 4-7(a) J‐V curves and (b) EQEs of PBDTTBO and PDTP‐DFBT tandem solar cells with different front and rear sub‐cell thickness..... 78

Figure 4-8 (a) J-V curves and (b) EQEs of PBDTTBO and PDTP-DFBT single junction and tandem solar cells with ZnO (dashed line) and Zr-Acac (solid line) as interconnecting layer. 78

Figure 5-1 (a) Chemical structures of PDBT-T1, TPH-Se, PBDBT and ITIC. (b) UV-vis spectra of PDBT-T1, TPH-Se, PBDBT and ITIC films. (c) Schematic of the organic tandem solar cells. 90

Figure 5-2 (a) Device performance of PDBT-T1 based fullerene and non-fullerene organic solar cells. (b) Evolution of normalized efficiency of PDBT-T1 based fullerene and non-fullerene organic solar cells. The devices were thermally aged at 120 °C. 91

Figure 5-3 2D GIWAXS patterns of (a) as-cast PDBT-T1:$PC_{71}BM$, (b) thermal-annealed PDBT-T1:$PC_{71}BM$, (c) as-cast PDBT-T1:TPH-Se and (d) thermal-annealed PDBT-T1:TPH-Se. The blends are thermally annealed at 120°C for 3 mins..... 93

Figure 5-4 Device performance of tandem solar cells based on PDBT-T1/TPH-Se/ITIC ternary front sub-cells. (a) Average device efficiency of tandem solar cells as a function of ITIC ratio (in total acceptor) in the front sub-cell. (b) Short circuit current of tandem solar cells as a function of ITIC ratio in the front sub-cell. (c) Current density-Voltage (J-V) curve in the best tandem devices. (b) External quantum efficiency of the best tandem devices. 95

Figure 5-5 (a) Average device efficiency of single junction PDBT-T1/TPH-Se/ITIC ternary solar cells as a function of ITIC ratio. (b) External quantum efficiency spectra single junction PDBT-T1/TPH-Se/ITIC ternary solar cells as a function of ITIC ratio. 2D GIWAXS patterns of PDBT-T1/TPH-Se binary blend and PDBT-T1/TPH-Se/ITIC (1:0.9:0.1) ternary blend. 97

Figure 5-6 (a) Photovoltaic characteristics of PDBT-T1:TPH-Se binary solar cells and PDBT-T1:TPH-Se:ITIC (1:0.9:0.1) ternary solar cells. (b) Thermal stability of PDBT-T1:TPH-Se binary solar cells and PDBT-T1:TPH-Se:ITIC (1:0.9:0.1) ternary solar cells. The devices are thermally aged at 120°C. 98

Figure 5-7 1D GIWAXS line profile of PDBT-T1:TPH-Se:ITIC with different ratios: (a) out-of-plane and (b) in-plane. 99

Figure 5-8 (a) Chemical structures of PTB7-Th and IEICO-4F films. (b) UV-vis absorption spectra of PTB7-Th:IEICO-4F blend. (c) I-V curves of triple-junction organic tandem solar cells (front sub-cell: PDBT-T1:TPH-Se:ITIC, middle sub-cell: PBDBT:ITIC and rear sub-cell: PTB7-Th:IEICO-4F). 100

Figure 6-1 (Molecular structures and film absorption (a) Molecular (donor) structures of PBDB-T and PTB7-Th. (b) Molecular (acceptor) structures of IT-M, FOIC and F8IC. (c) Film absorptions spectra of PBDB-T, PTB7-Th, IT-M, FOIC and F8IC. 109

Figure 6-2 (a) J–V curves of single-junction devices under illumination of an AM 1.5G solar simulator, 100 mW/cm^2. (b) EQE spectra of single-junction devices. 111

Figure 6-3 (a) LUMO and (b) HOMO energy levels of FOIC/F8IC mixed acceptors used in Rear 1 to 5. (c) Thermal stability tests of front sub-cell (PBDB-T/IT-M) and rear sub-cell (Rear 3: PTB7-Th:FOIC:F8IC)..... 112

Figure 6-4 2D GIWAXS patterns of PTB7-Th/FOIC/F8IC blends in different rear sub-cells and F8IC as well as FOIC..... 114

Figure 6-5 (a) Out-of-plane and (b) in-plane 1D GIWAXS profiles of PTB7-Th/FOIC/F8IC blends in different rear sub-cells. .....**Error! Bookmark not defined.**

Figure 6-6 Device structure, energy alignments and photovoltaic characteristics of tandem devices (a) Device structure. (b) Energy levels of donor and acceptor materials, and work functions of inter layers. (c) J–V curve of tandem device (based on Rear 3 sub-cell) under illumination of an AM 1.5G solar simulator, 100 mW/cm^2. (d) EQE spectra of tandem device (based on Rear 3 sub-cell). € Photovoltaic characteristics of tandem device (based on Rear 3 sub-cell) with the NREL certification (asymptotic scans on encapsulated devices). 117

Figure 6-7 The work function data of different transport layers..... 118

Figure 6-8 EQE spectrum of (a) front sub-cell and (b) rear sub-cell tested by NREL. 119

Figure 6-9 (a) The light field distribution of tandem device based on Rear 3 (125 nm for front sub-cell and 80 nm for rear sub-cell). (b) Generation rate of tandem device based on Rear 3 (125 nm for front sub-cell and 80 nm for rear sub-cell). 120

List of Tables

Table 3-1 Average Device Performance of Organic Solar Cells Based on Various ETLs 44

Table 3-2 The fitted full width at half maximum (FWHM) of in-plane polymer (100) peak 50

Table 4-1 The average device data of PBDTTBO:$PC_{71}BM$ and PDTP-DFBT:$PC_{71}BM$ devices with different active layer thickness. 69

Table 4-2: The average device performance parameters of tandem solar cell based on Zr-Acac interconnecting layer with different front and rear sub-cell thickness. 77

Table 4-2: The average device performance parameters of tandem solar cells based on ZnO and tandem solar cells based on ZnO interconnecting layer. 78

Table 5-1 Photovoltaic parameters of organic solar cells based on the PDBT-T1 wide bandgap polymer. 91

Table 5-2 Device performance of the champion double junction organic tandem solar cells based on different front sub-cells. 96

Table 6-1 Photovoltaic characteristics of single-junction devices. 111

Table 6-2 Photovoltaic characteristics of tandem devices. 118

Table 6-2 Photovoltaic characteristics of tandem devices based on Rear 3 with different combinations of front/rear sub-cell thickness. 119

Acknowledgments

It finally reaches this stage. I never imagined what a person I will be after ten years when I was still an undergraduate student. Tracing back to that time, the whole scenario until now is like an adventure.

The road to my Ph.D. in UCLA would not be accomplished without the help from my lovely family, wonderful colleagues and the other supporters. I want to thank all the people who substantial my faith and guide my research in the past years.

Prof. Yang Yang, my first and last PI in the UCLA, guides my research and affects my value of life through the whole Ph.D. life. I weren't able to survive the super competing environment without all his help. "Dream big" and "help others", which he always tells me and the others, deeply carve my academic target and actions. Although Prof. Yang is so tough in many aspects, he cares our thoughts and needs so much. Awards often come after challenges he brought, no matter in which forms and whether they succeed or not. I cannot express more to demonstrate my gratitude to his help to me.

I like to thank my committee members, Prof. Dwight Streit, Prof. Jaime Marian, and Prof. Xiangfeng Duan for their useful suggestion to make my research target and content better.

I am a lucky boy to join the YYLab. In the very beginning, my first mentor, Dr. Jingbi You, who is now an outstanding leading researcher in Chinese Academy of Sciences (CAS), had given me the first idea how to make a successful solar cell device. Dr. Lei Meng, who obtained his doctoral degree with excellent performance and also serve in CAS later, taught me every important process detail to achieve a sophisticated photovoltaic device. Prof. Yang Yang (Michael), who was selected as a Young Thousand Talented and now host a thriving lab in

Zhejiang University, guided me in advanced optics experiments of organic solar cells. I might have failed in the first difficult year without these smart minds helping me.

In my doctoral pursuing route, I want to show my greatest gratitude to Prof. Gang Li and Dr. Zirou Hong to share their profound knowledge on organic semiconductor devices without any reservation. I truly appreciate our organic solar cell team leaders Dr. Wenchao Huang and Dr. Pei Cheng and my partner Yuqiang Liu for our cooperation to achieve many important works on organic solar cells. With our cooperation, we broke the world record again! I also want to nominate the contribution of Dr. Bowen Zhu and Mr. Yu-Che Lin for their sharing of knowledge for interdisciplinary study.

Speaking of interdisciplinary research, it is my luck to participate in Dr. Yao-Tsung Hsieh and Prof. Qifeng Han's outstanding CIGS/Perovskite tandem solar cell. The working experience with them deeply inspired me for their patience and steel will to make a failed item become workable. I am grateful to work with every research fellows, post-docs and graduate students in the YYLab: thank Prof. Yaowen Li, Prof. Mingqui Wang, Prof. Kung-Hwa Wei, for sharing me their profound knowledge and insightful comments; Dr. Tze-Bin Song, Dr. Chun-Chao Chen, Dr. You Seung Rim, Dr. Yongsheng Liu, Dr. Wei-Hsuan Chang, Dr. Lijian Zuo, Dr. Letian Dou, Dr. Hsin-Sheng Duan, Dr. Huanping Zhou and Dr. Qi Chen, Dr. Tae-Hee Han, Dr. Jin-Wook Lee, Dr. Meng Dong, Dr. Hangbo Yang, Dr. Le Cai and Dr. Guangwei Xu for providing valuable solutions and guidance to technical problems; thank Dr. Huajun Chen, Dr. Sanghoon Bae, Dr. Pengyu Sun, Mr. Nicholas De Marco, Ms. Shiqi Dong, Mr. Zhanlue Yang, Mr. Hongxiang Zhao, Mr. Rui Wang, Ms. Jingjing Xue, Mr. Zhengxu Wang, Mr. Oliver Lin, Mr. Mr. Tianyi Huang, Ms. Selbi Nuryyeva, Mr. Shaun Tan, Mr. Bowen Xuan and Mr. Chaochen Wang many other lovely people for every kind of help in the lab.

I have to thank all my collaborators for our excellent works, which will be addressed later in different chapters in this thesis. Chapter 3 is based on the version of "High Mobility Indium Oxide Electron Transport Layer for Efficient Charge Extraction and Optimized Nano-Morphology in Organic Photovoltaics" by Wenchao Huang, Bowen Zhu, Sheng-Yung Chang, Shuanglin Zhu, Pei Cheng, Yao-Tsung Hsieh, Lei Meng, Rui Wang, Chaochen Wang, Chenhui Zhu, Christopher R McNeill, Mingkui Wang, Yang Yang. *Nano Lett.* 18, 5805−5811(2018); Chapter 4 is based on a version of "High-Efficiency Organic Tandem Solar Cells With Effective Transition Metal Chelates Interconnecting Layer" by Sheng-Yung Chang, Yu-Che Lin, Pengyu Sun, Yao-Tsung Hsieh, Lei Meng, Sang-Hoon Bae, Yu-Wei Su, Wenchao Huang, Chenhui Zhu, Gang Li, Kung-Hwa Wei and Yang Yang. *Solar RRL*, 1 (10), 1700139 (2017); Chapter 5 is based on the version of "High Efficiency Non-fullerene Organic Tandem Photovoltaics Based on Ternary Blend Subcells" by Wenchao Huang, Sheng-Yung Chang, Pei Cheng, Dong Meng, Bowen Zhu, Selbi Nuryyeva, Chenhui Zhu, Lijun Huo, Zhaohui Wang, Mingkui Wang, Yang Yang. *Nano Lett,* 18 (12), 7977–7984 (2018); Chapter 6 is based on the version of "Efficient Tandem Organic Photovoltaics with Tunable Rear Sub-cells" by Pei Cheng, Yuqiang Liu, Sheng-Yung Chang, Tengfei Li, Pengyu Sun, Rui Wang, Hao-Wen Cheng, Tianyi Huang, Lei Meng, Selbi Nuryyeva, Chenhui Zhu, Kung-Hwa Wei, Baoquan Sun, Xiaowei Zhan, Yang Yang. *Joule*, in press; Joule; Chapter 7, also the last chapter is based on on the version of "Transparent Polymer Photovoltaics for Solar Energy Harvesting and Beyond" by Sheng-Yung Chang, Pei Cheng, Gang Li, Yang Yang. *Joule*, *2*(6), 1039-1054 (2018)

I appreciate Dr. Wenbing Yang for providing me an internship at Lam research and I like to thank my intern mentor Dr. Yiwen Fan and many people there. This first intern experience in the industry is important and memorable to my future career.

I am so lucky to have so many fantastic friends in Los Angeles. I thank Mr. Andy Hsu to host me when I arrived LA for first time. Mr. Tien-Shu Chang and Mr. Asa Chan are my super good roommates and we had a peaceful time before we departed. I have to thank Mr. Shin-Hung Tsai, Dr. Yu-Sheng Kuo, Dr. Ting-Chiang Lin, Ms. Yi-Hsuan Hsiao, Dr. David Chang, Ms. Sandy Kuo, Ms. Iris Chang, Ms. Chia-Ying Shen, Mr. Cheng-His Lin, Dr. Jeff Chang, Mr. Joey Chou, Mr. Yueh-Ning Ku, Dr. Hui-Ying Shiu, Dr. Chiao Chang, Mr. Leo Chiu and Dr.. Eric Young for all the hanging-out times and sharing of happiness.

Last, I would like to thank my dearest parents, my siblings and other family members in Taiwan. Their support is the main driving force for me to study aboard. I have special thanks to Phoebe Tsai, who have substantiated my spirit during these memorable years. If I have not accompanied by you, everything could not be successful.

Thank you!

VITA

2006-2010	Bachelor of Science, Department of Physics, National Taiwan University, Taiwan
2010-2012	Master of Science, Department of Physics, National Taiwan University, Taiwan
2013-2014	Research Assistant, Institute of Physics at Academia Sinica, Taiwan
2018	Process R&D Engineer Intern, Lam Research, California, USA
2014-2019	Graduate Student Researcher,

Publications

1. Huang, W.; Zhu, B.; Chang, S.Y.; Zhu, S.; Cheng, P.; Hsieh, Y.T.; Meng, L.; Wang, R.; Wang, C.; Zhu, C.; McNeill, C.; Wang, M.; Yang, Y. (2018) High mobility indium oxide electron transport layer for efficient charge extraction and optimized nano-morphology in organic photovoltaics. *Nano Lett.* 18, 5805−5811

2. Chang, S.Y.; Lin, Y.C.; Sun, P.; Hsieh, Y.T.; Meng, L.; Bae, S.H.; Su, Y.W.; Huang, W.; Zhu, C.; Li, G.; Wei, K.H.; Yang, Y. (2017) High-efficiency organic tandem solar cells with effective transition metal chelates interconnecting layer. *Solar RRL* 1 (10), 1700139

3. Huang, W.; Chang, S.Y.; Cheng, P.; Meng, D.; Zhu, B.; Nuryyeva, S.; Zhu, C.; Huo, L.; Wang, Z.; Wang, M.; Yang, Y. (2018) "High efficiency non-fullerene organic tandem photovoltaics based on ternary blend subcells" *Nano Lett* 18 (12), pp 7977–7984

4. Cheng, P.; Liu, Y.; Chang, S.Y.; Li, T.; Sun, P.; Wang, R.; Cheng, H.W.; Huang, T.; Meng, L.; Nuryyeva, S.; Zhu, C.; Wei, K.H.; Sun, B.; Zhan, X.; Yang, Y. (2018) Efficient tandem organic photovoltaics with tunable rear sub-cells. *Joule,* in press

5. Chang, S.Y.; Cheng, P.; Li, G.; Yang, Y. (2018) Transparent polymer photovoltaics for solar energy harvesting and beyond. *Joule 2*(6), 1039-1054

Chapter 1 Introduction

In the 21st century, the demand for massive and diverse energy supply becomes more urgent because of the growing human population, which has increased from 1.5 to 7.3 billion in just 100 years. Traditional energy materials like coal, oil and nature gas, which are still the main stream for providing power, are much more likely to be prone to depletion. Furthermore, severe emissive pollutions resulted from consuming these fossil fuels have become a lethal issue in some biggest economics like China and India. Due to their population and industrial scale, the negative influence will not only impact locale people but global environments. As a result, several alternative energy technologies have been eagerly developed. Among all of them, solar cell is the most important one.

The average value of solar energy absorbed by surficial water bodies and lands on the earth is 89 petawatts, which is more than 10,000 times the Human's total energy use. Inventing a more efficient method to utilize the solar energy is the key to achieve a more sustainable civilization. In the first chapter, a history and working principle of solar cells will be introduced and followed by an overview of thin film solar cells. Our focus, organic solar cell and its bottlenecks will be then reviewed and the corresponding research topics are going to be presented in the next chapter.

1.1 Development History of Solar Cells

The first photovoltaic effect was discovered by a French scientist Edmond Becquerel in 1839. It revealed that some materials can develop electrical voltage when illuminating it with light.[1] In 1876 and 1879, British engineer and scientists respectively found the photoconductivity of selenium and an ability of electricity generation from selenium without thermal or mechanical sources.[2] In 1883, an American inventor successfully manufactured the first working solar cell by using selenium as light absorber coated with a thin layer of gold to achieve 1% efficiency.[1-3] In 1887, a German physicist observed the photoelectric effect for the first time, disclosing the idea that light can be used to release electrons from the solid surface and a shorter wavelength light (ultraviolet) is more capable to stimulate electrons than a visible light.[2] The photoelectric effect was later elaborated by Albert Einstein in 1904 and its experimental proof to support the theory was achieved until 1916 by Robert Millikan. It eventually lead in Albert Einstein's Nobel Prize in 1921. [1-3]

In 1954, Daryl Chapin, Calvin Fuller and Gerald Pearson three scientists in Bell Laboratories, developed the first silicon solar cell with 6% efficiency. The key improvement was the doping in semiconductor material by the diffusion of boron into silicon to create suitable charge carrier density. It was a milestone for a practical solar cell.[2,3] During late 1950s to 1960s, the silicon solar cells efficiency had been quickly enhanced from 6% to 14% thanks to the strong demand of the space race. Not until the energy crisis in 1970s was the solar cell considered to be a major power supplier because of the extremely high cost (about $150 per watt). The fear for oil shortage drove the development of solar cell technology for commercial use. Reducing the fabrication cost of solar cell and simultaneously increasing the efficiency

became to be the first concern. Before talking more on the development of solar cell, we need to know the fundamental physics

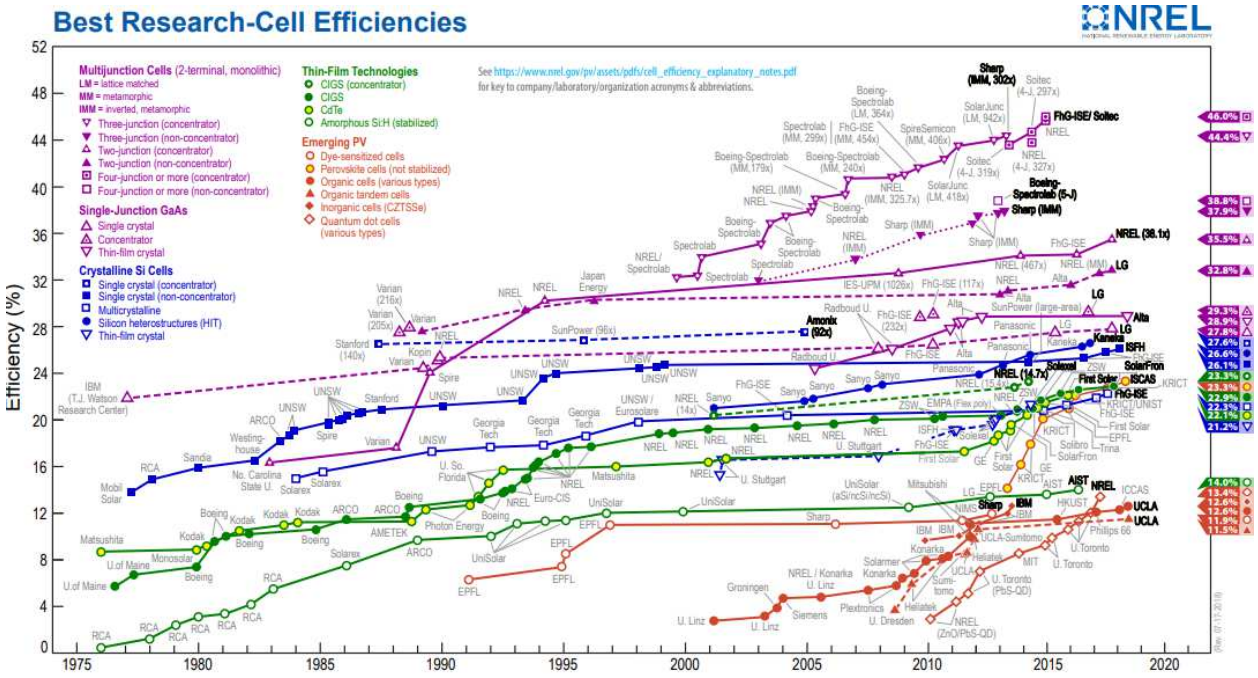

Figure 1-1 The energy efficiency chart by National Renewable Energy Laboratory.[4]

1.2 Working Principles of Solar Cells

A typical solar cell is composed of a semiconductor p-n junction (photoactive layer), anode and cathode, and the external circuit that have been designed to absorb and convert photon into electricity as shown in **Figure 1.2**.[5] When the incident light with energy higher than the bandgap of the p-type or n-type semiconductor materials, the light can be absorbed and excite electrons from the valence band to the conduction band, and then form electron-hole pairs (excitons). Consequently, excitons can be dissociated by the built-in potential when they reach the p-n junction so that the separated charges turn into the free charge carriers. The contact electrodes then transfer these free charge carriers from the photoactive layer into an external circuit. The electric power can then be facilitated from the circuit. The quality of the semiconductor and conductive materials and their interfaces are critical to achieve a good solar cell.

The solar cell performance is determined by the power conversion efficiency (PCE), which can be obtained by a light-exposed solar cell. The major parameters of a solar cell are J_{SC}, V_{OC}, FF and P_{MAX}. The definition of PCE is:

$$PCE = \frac{P_{max}}{P_{in}} = \frac{voltage \times current\ density\ at\ \text{maximum}\ power\ point}{Incoming\ light\ energy\ per\ unit\ area}$$

$$= \frac{Voc \times Jsc \times FF}{incoming\ light\ energy\ \ per\ unit\ area}$$

A typical solar cell J-V curve is shown in **Figure 1-3**. It can be considered the behavior of a diode under dark and light illumination. The term V_{OC} stands for the open circuit voltage,

meaning the voltage at the open circuit point (V_{total}=0). V_{OC} is related to the degree of recombination, such as the saturation current density, in a solar cell device. As the condition of V_{OC} represents there is no net current flowing through the external circuit, the definition of V_{OC} can be written as below:

$$Voc = \frac{kT}{q} ln\left[\frac{J_{Photon}}{J_0} + 1\right] \cong \frac{kT}{q} ln\left[\frac{J_{Photon}}{J_0}\right]$$

The approximation comes from that the J_{Photo} is usually much larger than J_0.

The term J_{SC} stands for the short circuit current density, which means the current density at the short circuit point (V_{ext}=0). J_{SC} is determined by the absorbed photons of the solar cell, which is closely related to the light spectrum. The most important parameters affecting J_{SC} is the diffusion length of minority carriers in each of the semiconductor material. The net current density can be expressed as:

$$J\,(V) = J_0\left[exp\left(\frac{qV}{kT}\right) - 1\right] - J_{Photon}$$

where V = applied voltage across the diode, J_0 = dark saturation current density, q = electric charge, k = Boltzmann's constant, T = temperature, J_{Photo} = light generation current density.

The FF, which means the fill factor, is obtained from the ratio between $V_{MAX} \times J_{MAX}$ divided by $V_{OC} \times J_{SC}$. The maximum power point is determined at the point where the product of the maximum voltage and current density.

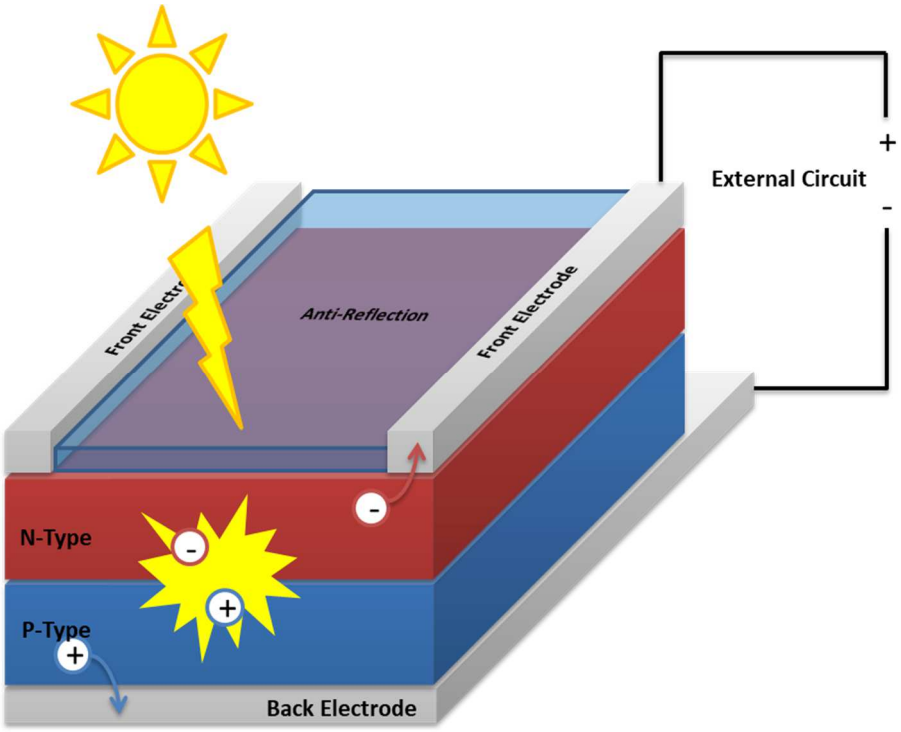

Figure 1-2 Basic solar cell device structure.

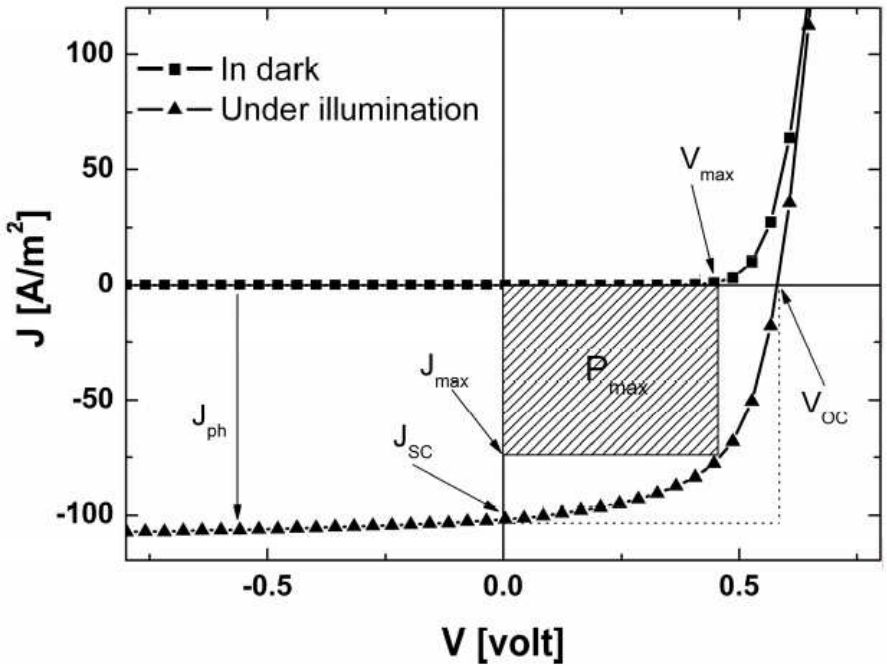

Figure 1-3 Current density-Voltage (J-V) characteristics of a typical solar cell under illumination.

1.3 Overview of Thin Film Solar Cells

Silicon solar cell is deemed as the currently most stable solar cell type. The single crystalline silicon solar cell can demonstrate a certified efficiency at 26%. Yet there are some intrinsic disadvantages like thick active layer (more than 100 um) that has to be fabricated by the high temperature furnace process and sharply reduced efficiency in dim environment due to the bad light extinguishing coefficient.

In order to compensate these disadvantages, thin film photovoltaic technologies, include micro/polycrystalline silicon, amorphous silicon, III-V group solar cells, copper indium gallium diselenide (CIGS), cadmium telluride (CdTe), dye-sensitized solar cells (DSC), hybrid organic-inorganic perovskite solar cells and organic solar cells have been developed. Nevertheless, there are many challenges for these emerging types of solar cells. The main issue of amorphous and polycrystalline silicon is prone to the worse device efficiency than the single crystalline one and high vacuum tools as well as high temperature process are still needed. III-V group solar cells like GaAs-based one can achieve very high efficiency but the cost and complexity of film growth are also the highest. The key components in CIGS and CdTe are scarce and toxic: Indium, gallium and tellurium are rare and also frequently used in other electronic applications. Cadmium has a strong negative impact to the environment and human body. For the DSC solar cells, the major disadvantage is also low efficiency and unstable liquid electrolyte material. Recent perovskite solar cell has a comparable efficiency to silicon based one but it suffers the same issue of material toxicity (Lead contained) and long term stability.

For serving as an alternative energy source compare to single crystalline silicon solar cell People should emphasize the advantages of these technologies like low production cost,

environment-friendly process and large scale printing technique compatibility. Generally speaking, organic solar cell, which uses polymers, small molecules or dyes as absorber, is the main stream in solution process-compatible types. CIGS, CZTS and Hybrid perovskite solar cell can also be prepared by solution process but are out of my scope in this study. My focus, organic solar cell, will be introduced in the following sessions.

1.4 Organic Solar Cells

Organic solar cell, or organic photovoltaic (OPV) devices are based on organic semiconductors like carbon-based materials which the backbones are composed of C–C single bond and C=C double bond with different chemical moieties.[6] The ability of the electron delocalization within the conjugated backbone will alter the semiconducting properties of the devices.[7] Thanks to its intrinsic weak intermolecular van de Waals interaction, organic solar cell can be conducted by low-cost, large-area deposition methods such as roll-to-roll printing or blade coating.[8] In recent five years, the research interest of organic solar cells are back to thrive due to the development of new organic materials and efficiency breakthrough.

OPVs are divided into two different categories according to whether their constituent molecules are either small or large, like oligomers and polymers. The two classes of materials are quite different in many aspects as synthesis and thin film preparation processes. Small-molecule solar cells are processed mainly using thermal evaporation deposition in a high-vacuum environment while polymer solar cells are processed from solutions. Polymer solar cells are attractive owing to a number of advantageous features, including their thin-film architecture, high absorption coefficient, their utilization of efficient solution processes and low manufacturing energy requirements.[9] In addition, their low specific weight, mechanical

flexibility, tunable material properties and high transparency also enable more possible applications in wearable devices or building integrated photovoltaics (BIPV).

A typical device structure in organic solar cell is consisted of low work function cathode, electron transport layer, photoactive layer including donor and acceptor semiconductor materials, hole transport layer and high work function anode. The device schematic and energy diagram of polymer solar cell are illustrated is shown in **Figure 1-4**.[10] Once a photon is injected to the organic sola cell, it will be absorbed by the semiconductor materials in photoactive layer and creates an electron-hole pair, or *exciton*. The exciton will diffuse in the semiconductor material until it reaches the junction between the donor and acceptor. The energy difference between the lowest unoccupied molecular orbital (LUMO) of the donor material and highest occupied molecular orbital (HOMO) of the acceptor material can provide the driving force for the dissociation of Frenkel excitons. After charge separation at the donor–acceptor interface, holes and electrons travel to the positive and negative electrodes through donor and acceptor networks, respectively. The third key factor is the organic–electrode interface, where the charges are extracted to external circuits. The charge collection efficiency $\eta_{CC}(\lambda)$ accounts for both carrier transport in the networks and the extraction steps.

The photovoltage (or open-circuit voltage, V_{OC}) of the device is directly linked to the energy difference between the LUMO level of the acceptor and the HOMO level of the donor, which are the source of primary driving force for charge separation. The short-circuit current density (J_{SC}) is equal to the integral of the product between cell responsivity and incident

solar spectral irradiance. Having a low bandgap difference to obtain broader solar spectrum and enlarging the energy level difference between the LUMO level of the donor and the HOMO level of the acceptor will result in high values of J_{SC} and V_{OC}, respectively. As a result, V_{OC} and J_{SC} are needed to be balanced to maximize the power conversion efficiency. The external quantum efficiency (EQE) as a function of wavelength (λ) is the ratio between the collected photo-generated charges and the number of incident photons, ultimately being the product of four efficiencies (η): absorption (A), exciton diffusion (ED), charge separation (CS) and charge collection (CC), giving $EQE(\lambda) = \eta_A(\lambda) \times \eta_{ED}(\lambda) \times \eta_{CS}(\lambda) \times \eta_{CC}(\lambda)$.

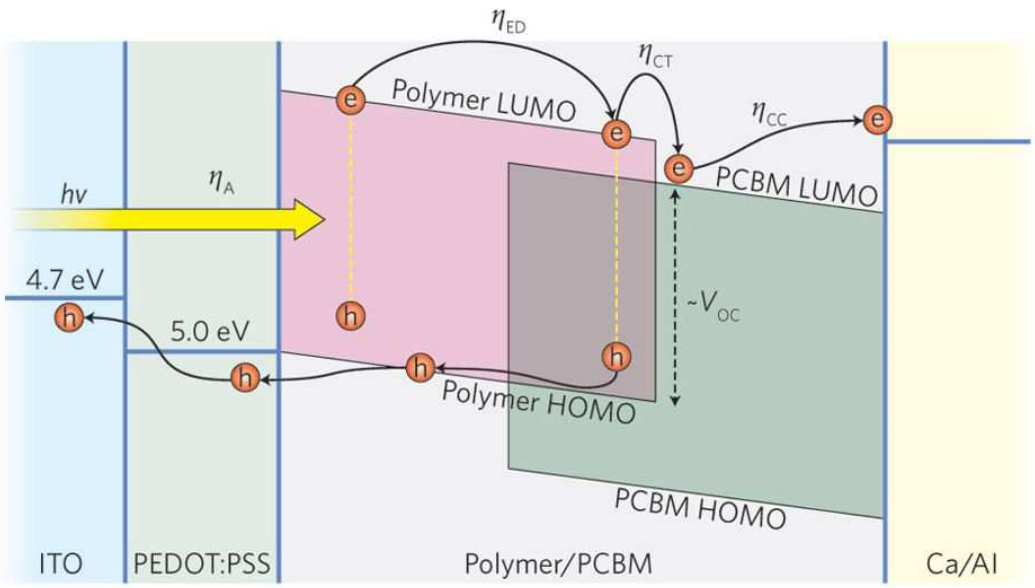

Figure 1-4 The operating mechanism of a polymer solar cell.[10]

A major achievement in OPV technology was the adoption of C_{60} fullerene and its derivatives (such as [6,6]-phenyl-C_{61}-butyric acid methyl ester, PCBM), which have strong electronegativity and high electron mobility, to replace the other n-type molecules in solar cell devices.[11] In the early 1990s, Heeger *et al*. and Yoshino *et al*. independently demonstrated

electron transfer between a conjugated polymer and fullerene derivatives. There is an extremely fast photo-induced electron transfer process of around 50–100 fs, which dominates over all other photo-physical processes present in organic solar cell device.[12, 13] These discoveries provided a solid foundation for OPV technology.

1.5 Challenges for Organic Solar Cells

1.5.1 Transport of Exciton and Charge Carriers

One of the major differences between organic semiconductors and inorganic semiconductors is the binding energy of excitons. In organic semiconductor, excitons are tightly bound resulting from the low dielectric constant ($\varepsilon r \approx 2–4$) of organic materials. The binding energy of the Frenkel exciton is in the range of 0.3–1 eV.[14, 15] A large binding energy impedes exciton dissociation by an internal electrical field, which reduces the short circuit current

In regards of efficient current harvest, there are still the other certain limitations including small surface area between the donor–acceptor interfaces and the requirement of long carrier lifetime to ensure that the electrons and holes reach their respective electrodes. This problem can be solved by introducing a bulk heterojunction as shown in **Figure 1.5**, which means mixing donor–acceptor materials in the bulk body rather than conventional bi-layered structure. By using bulk heterojunction, the physical distance from P-type to N-type can be shortened to 10 nm or even smaller scale and enable a higher change for exciton dissociation. The preferred morphology of bulk heterojunctions is a bicontinuous interpenetration network. Donor and acceptor domains should be twice the size of the exciton diffusion length and increase the $\eta_{ED}(\lambda)$ and $\eta_{CS}(\lambda)$ ratios.

This concept was firstly demonstrated by Hiramoto through the co-evaporation of donor and acceptor materials under high-vacuum conditions.[16] The first efficient bulk heterojunction organic solar cell were independently reported in 1995 by Heeger and Friend in polymer–fullerene and polymer–polymer blends.[17, 18] Polymer–fullerene systems currently dominate the field of high-efficiency organic solar cells. The efficiencies are now beyond 13% and some publications even claim higher values. Innovations in materials science have provided efficient ways of enhancing the device efficiency and morphology modification is another critical factor in bulk heterojunction solar cells.

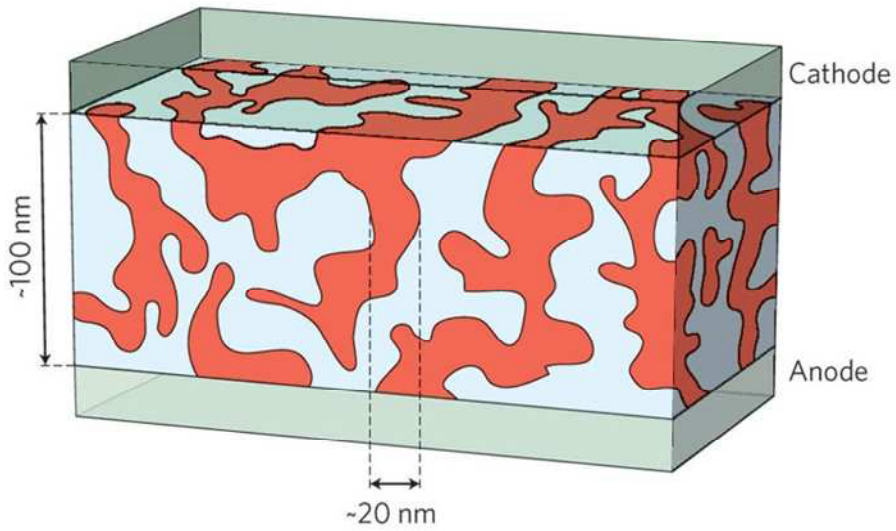

Figure 1-5 Conceptual morphology model with bicontinuous interpenetration network of the polymer and the acceptor.[10]

Although the bulk heterojunction concept is a certain solution for creating higher chance for excitons to dissociate in the active layer of the organic solar cells, the following route can still compromise the short circuit current. The other key factor is the organic–electrode interface, where the free charges are extracted to external circuits. After charge separation at the donor–acceptor interface, holes and electrons must travel to the positive and

negative electrodes through donor and acceptor networks, respectively. The charge collection efficiency $\eta_{CC}(\lambda)$ accounts for both the extraction steps and carrier transport in the networks. As a result, good transport materials are indispensable to achieve a high efficiency organic solar cell. However, there are more restrict constrains for preparing a high quality transport layer due to the processing limitation for organic materials. High temperature annealing (> 200 □) is usually forbidden for protecting the low-lying organic layers, which means the traditional good conductive crystalline materials cannot be used and high transparency as well as good Ohmic contact are still needed to be achieved. Solution processable metal oxide nano particles, like Zinc oxide, are the typical transport layer materials in organic solar cell for their low temperature process and acceptable electronic properties. Yet there are still some disadvantages like low mobility (< 1 cm^2/Vs) caused from impurities and residue solvents and lower charge carrier density which may limit the total enabled short-circuit current.

1.5.2 Shockley−Queisser limit

Back to 1960, William Shockley and Hans J. Queisser derived an upper theoretical efficiency limit of the single p−n junction solar cell by only considering the fundamental physics like detailed balance. It is called the Shockley−Queisser limit or detailed balance limit.[19] It was the first theoretical calculation based on non-empirical values of the constants of the characteristics of the solar cells and it is considered to be a mile stone contribution in solar cell development because of its prediction of solar cell efficiency development .

The Shockley-Queisser limit assumes the sun and solar cell are blackbodies with , respective temperature of 6000K and 300K. The ideal case should follow several assumptions: (1) Only the radiative recombination mechanism exists. (2) Sunlight is not concentrated. (3) If

the photons have energy greater than the bandgap, all energy is converted to heat. (4) One photon only generates one exciton. (5) Only one PN junction in one solar cell. As shown in **Figure 1-6**, the maximum power conversion efficiency was calculated to be approximately 33% based on a single p−n junction with bandgap of 1.1 eV. 67% of the total photon energy could not be utilized in this model. A major part of the loss was attributed to bandgap loss, which is because of the optical responses of semiconducting bandgap. Photons with lower energy than that of the absorber bandgap cannot be absorbed by the active layer, while photons with higher energy than bandgap ultimately produce charge carriers having the same energy as the bandgap.

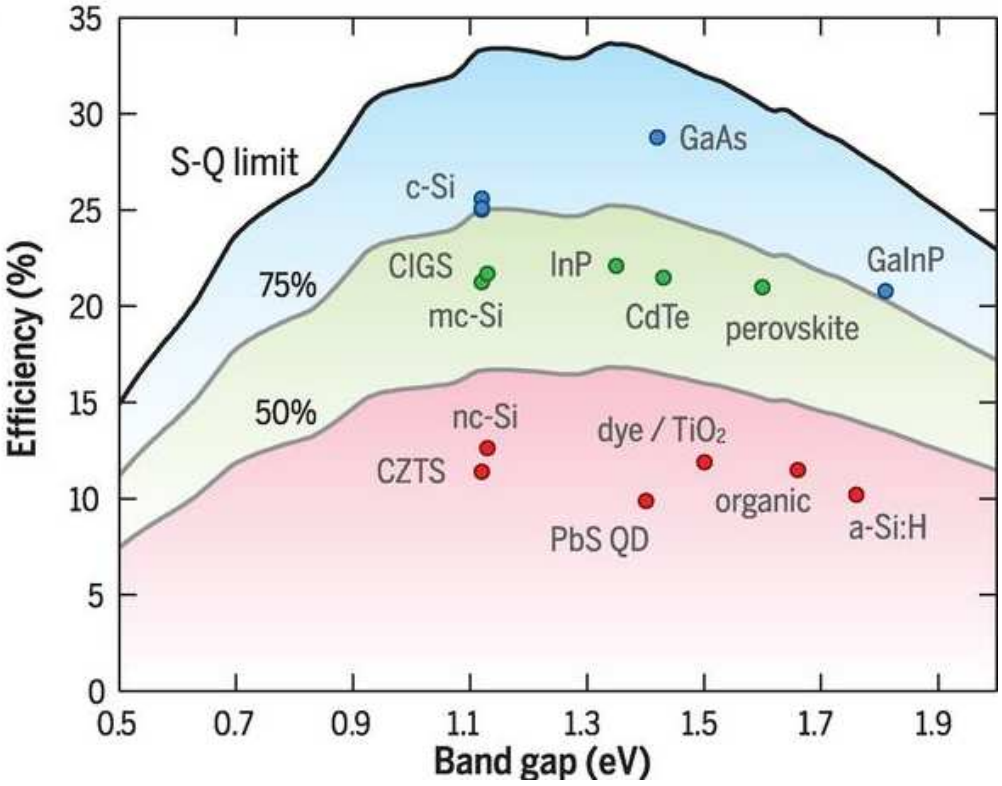

Figure 1-6 Theoretical Shockley-Queisser detailed-balance efficiency limit as a function of band gap (black line) and 75% and 50% of the limit (gray lines). The record efficiencies for different materials are plotted for the corresponding band gaps.[20]

1.5.3 Absorption Spectrum

Besides the transport properties, the major disadvantage of organic solar cell device is the absorption spectrum. Compared to inorganic materials like Si (1.1 eV) and GaAs (1.3 eV), who have continues conduction band and valance band, polymers and small molecules usually have a bandgap larger than 1.5 eV due to the disorder of molecular packing. As described in **Chapter 1.6.3**, this feature is the major cause that compromises the absorption spectrum and results in worse short circuit current. For achieving a higher J_{SC}, narrowing the bandgap for a broader coverage of the solar spectrum is essential.[21-23] Typical methods of designing small bandgap molecules include using an alternating donor–acceptor structure in the same molecular structure, replacing the aromatic structure by the quinoid structure, controlling the polymer chain planarity and tuning the effective conjugation length. Designing an alternating donor–acceptor structure is the most common way which the push–pull driving forces generated fromthe donor and acceptor units. It enhances photoinduced intramolecular charge transfer, facilitates electron delocalization and forms the quinoid mesomeric structures over the polymer backbone.[21,24,25] According to molecular orbital perturbation theory, electron delocalization leads in the hybridization of molecular orbitals which then results in electron redistribution throughout the interacting orbitals. The molecular structure coupling thus create two new hybridized orbitals: a higher HOMO level and a lower LUMO level and they form a narrower bandgap.

Although J_{SC} can be improved by using the above methods to design new material, it is still a big challenge to simultaneously improve both V_{OC} and J_{SC}. Narrowing the bandgap can

improve J_{SC}, but V_{OC} will be compromised because of the approaching HOMO and LUMO levels. The other strategies beyond the molecular level should be adopted to enable more flexibility to achieve a high efficiency organic solar cell.

References

1. US Department of Energy, "The History of Solar," Office of Energy Efficiency & Renewable Energy, https://www1.eere.energy.gov/solar/pdfs/solar_timeline.pdf, accessed on December, 2018.

2. Solar Power authority, "A History of Solar Cells: How Technology Has Evolved", https://www.solarpowerauthority.com/a-history-of-solar-cells/, accessed on December, 2018.

3. Martin A. Green. (2009) "The Path to 25% Silicon Solar Cell Efficiency: History of Silicon Cell Evolution", *Prog. Photovolt: Res. Appl*. 17:183-189.

4. National Renewable Energy Laboratory, November, 2018.

5. PVEducation.ORG, "Chapter 4: Solar Cell Structure", http://pveducation.org/pvcdrom/solar-cell-structure, accessed on April 1, 2018.

6. Li, G., Zhu, R. Yang, Y. (2012). Polymer solar cells. *Nat. Photonics 6*(3), 153-161

7. Pope, M. Swenberg, C. E. *Electronic Processes in Organic Crystals and Polymers* 2nd edn (Oxford Univ., 1999).

8. Forrest, S. R. (2004). The path to ubiquitous and low-cost organic electronic appliances on plastic. *Nature 428*(6986), 911-918.

9. Dennler, G., Scharber, M. C., Brabec, C. J. (2009). Polymer□fullerene bulk□ heterojunction solar cells. *Adv. Mates. 21*(13), 1323-1338.

10. Yang, X., Loos, J. (2007). Toward high-performance polymer solar cells: the importance of morphology control. *Macromolecules 40*(5), 1353-1362.

11. Hummelen, J. C., Knight, B. W., LePeq, F., Wudl, F., Yao, J., Wilkins, C. L. (1995). Preparation and characterization of fulleroid and methanofullerene derivatives. *J. Org. Chem. 60*(3), 532-538.

12. Sariciftci, N. S., Smilowitz, L., Heeger, A. J. Wudl, F. (1992) Photoinduced electron-transfer from a conducting polymer to Buckminsterfullerene. *Science* 258, 1474–1476.

13. Morita, S., Zakhidov, A. A. Yoshino, K. (1992) Doping effect of Buckminsterfullerene in conducting polymer — change of absorption-spectrum and quenching of luminescence. *Solid State Commun.* 82, 249–252.

14. Espinosa, N., Garcia-Valverde, R., Urbina, A., Krebs, F. C. (2011). A life cycle analysis of polymer solar cell modules prepared using roll-to-roll methods under ambient conditions. *Sol. Energy Mater Sol. Cells 95*(5), 1293-1302.

15. Tang, C. W. (1986). Two□layer organic photovoltaic cell. *Appl. Phys. Lett. 48*(2), 183-185.

16. Hiramoto, M., Fujiwara, H. Yokoyama, M. (1992) P-I-N like behavior in 3-layered organic solar-cells having a co-deposited interlayer of pigments. *J. Appl. Phys.* 72, 3781–3787.

17. Yu, G., Gao, J., Hummelen, J. C., Wudl, F. Heeger, A. J. (1995) Polymer photovoltaic cells — enhanced efficiencies via a network of internal donor–acceptor heterojunctions. *Science* 270, 1789–1791.

18. Halls, J. J. M.; Walsh, C. A.; Greenham, N. C.; Marseglia, E. A.; Friend, R. H., Moratti, S. C., & Holmes, A. B. (1995). Efficient photodiodes from interpenetrating polymer networks. *Nature 376*, 498-500.

19. Shockley, W.; Queisser, H. J. (1961) Detailed balance limit of efficiency of p-n junction solar cells. *J. Appl. Phys. 32*, 510-519.

20. Polman, A.; Knight, M.; Garnett, E. C.; Ehrler, B.; Sinke, W. C. (2016) Photovoltaic materials: Present efficiencies and future challenges. *Science 352*, aad4424.

21. Cheng, Y. J.; Yang, S. H. Hsu, C. S. Synthesis of conjugated polymers for organic solar cell applications. (2009) *Chem. Rev.* 109, 5868–5923.

22. Liang, Y. Y.; Yu, L. P. (2010) Development of semiconducting polymers for solar energy harvesting. *Polym. Rev.* 50, 454–473.

23. Liang, Y. Y.; Yu, L. P. (2010) A new class of semiconducting polymers for bulk heterojunction solar cells with exceptionally high performance. *Acc. Chem. Res.* 43, 1227–1236.

24. Havinga, E. E.; Tenhoeve, W. Wynberg, H. (1993) Alternate donor–acceptor small-band-gap semiconducting polymers — polysquaraines and polycroconaines. *Synth. Met.* 55, 299–306.

25. Zhang, Q. T. Tour, J. M. (1997) Low optical bandgap polythiophenes by an alternating donor/acceptor repeat unit strategy. *J. Am. Chem. Soc.* 119, 5065–5066.

Chapter 2 Principles for Enhancing Power Conversion Efficiency

Considering of the issues of single junction organic solar cells, several approaches have been proposed to improve the performance. One thing is to compensate the low carrier life time within the active layer. Applying a higher mobility transport layer for a better charge extraction property is a feasible way if a suitable transport material can be found, though there are many requirements to meet with. Surface work function modification is also important for a barrier-less charge transport. The other thing is to improve the fundamental physical property: the absorbance of organic solar cells. This includes two methods: Tandem and Ternary structures. Tandem structure which comprised of sub-cells with different bandgaps can capture a wider range of incident photons and minimize the thermal loss due to the difference between the absorbed hot photons and the bandgap. Ternary structure is an internal approach, which incorporates the other semiconductor material in the original binary mixture of p-type and n-type semiconductor materials. The third component should have complementary absorption spectrum with the original semiconductor materials. The aforementioned ideas have been proposed and applied in different organic solar cells. However, there are still many issues remained to be solved due to the increased complexity by adopting these methods.

2.1 Fermi Level Pinning by Interface Modification

To improve the charge transport properties between the surfaces of organic materials and transport layers for better extraction, modifications of their energy levels to achieve Fermi level pining is a useful way. In the interface of transitional-metal oxide (TMO) and organic semiconductor material, it is usually non-reactive/weak. To elaborate the relationship in the interaction of the two materials, several models have been brought out. Braun suggested that the most relevant parameters in energy level alignment at TMO/organic interfaces are the TMO's work function and the energy level of molecular orbitals.[1] An universal alignment trend that can be divided into three regimes: Fermi level pinning to the highest occupied molecular orbital (HOMO) of the molecule, Fermi level pinning to the lowest unoccupied molecular orbital (LUMO), and vacuum level alignment. Greiner have further proposed and demonstrated a universal energy level alignment (UELA) rule at oxide/organic interfaces.[2] Taking C60 as organic semiconductor material and several TMO as examples, the experimental result properly fit the theory.[5] As shown in **Figure 2.1**, the measured HOMO edge offset (ΔEH) of monolayer C60 films plotted against the work function (Φsub) of the bare TMO substrate. It is quite clear that C60 energy level alignment has three distinct features: (I) a first plateau region with $\Delta EH \sim 2.3$ eV for $\Phi sub < 4.2$ eV; (II) a linear region $\Delta EH \propto \Phi sub$ for 4.2 eV $< \Phi sub < 6.3$ eV; (III) a second plateau region with $\Delta EH \sim 0.3$ eV for $\Phi sub > 6.3$ eV. In region (II), the energy offset decreases linearly as the substrate work function increases. In this regime, the work function of the TMO is in between the molecule's ionization energy and electron affinity (IE org>Φsub> EA org). This region corresponds to a relatively weak interaction between the organic semiconductor and the underlying substrate such that the slope of the trend line is approximately 1 and the Schottky-Mott rule holds.[3,4] In region (III), the substrate work

function is larger than that of the ionization potential of C60, i.e., the Fermi level of the TMO is lower than that of the HOMO. This leads to ionization of the C60 to maintain Fermi level equilibrium. Region (III) is often referred to as Fermi level pinning to the HOMO. In region (I), the HOMO offset plateaus at 2.3 eV, which coincides with the energy gap of C60. This suggests that the substrate Fermi level is aligned with C60's LUMO, which means pinning of the substrate Fermi level to the LUMO. This also suggests that the C60 film receives charge to maintain electrochemical equilibrium with the electrode.

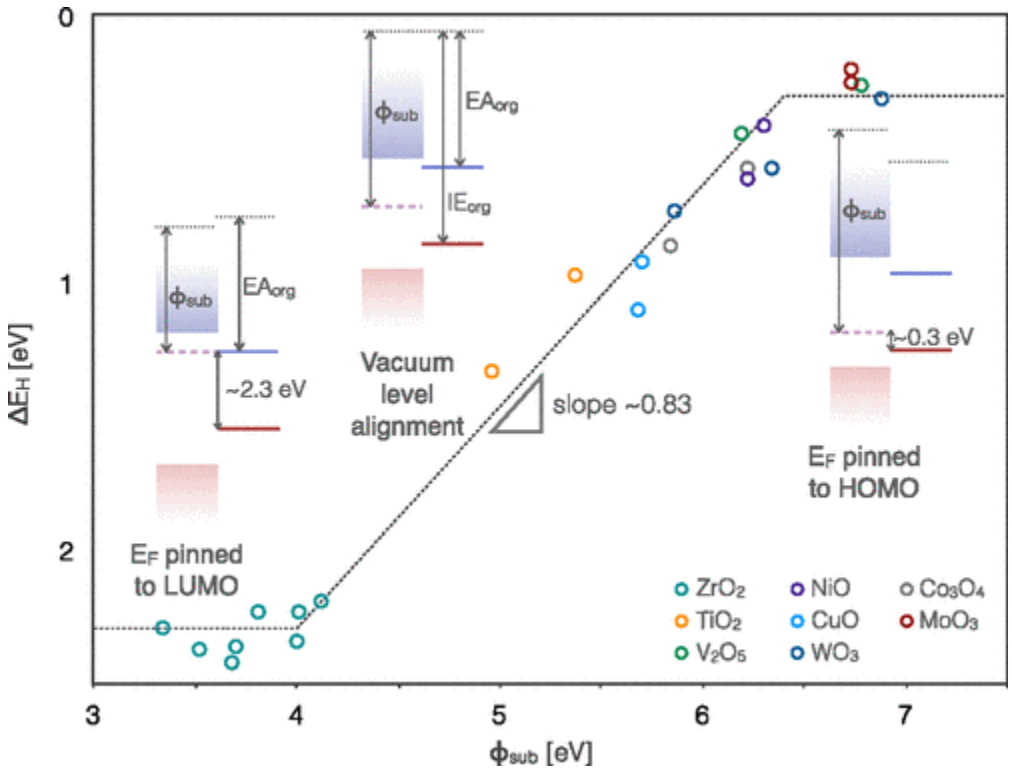

Figure 2-1 Energy level alignment at the interface of TMO and C60. HOMO edge offset (ΔEH) of C60 is plotted against the work function (Φsub) of underlying TMOs. Three regimes can be identified. The energy positions of key parameters in each scenario are shown in the schematics beside each region.[5]

This concept was also proved elsewhere. An Ohmic hole contact on organic semiconductors can be formed. The injected hole current from high-work-function metal-oxide electrodes is improved by more than an order of magnitude by using an interlayer for which the sole requirement is that it has a higher IE (> 0.3 eV from the empirical cases) than the organic semiconductor, as shown in **Figure 2.2**. Insertion of the interlayer results in electrostatic decoupling of the electrode from the semiconductor and realignment of the Fermi level with the IE of the organic semiconductor.[6]

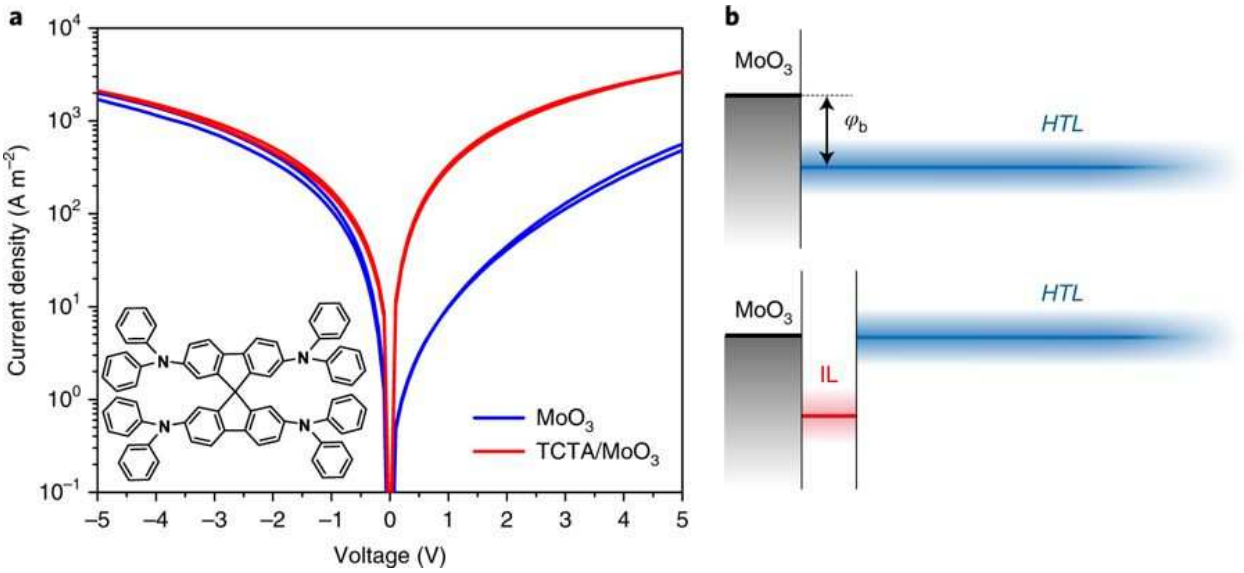

Figure 2-2 (a) Current density–voltage characteristics of a PEDOT:PSS/Spiro-TAD/MoO_3 hole-only device with and without a TCTA (5 nm) interlayer between the Spiro-TAD (163 nm) transport layer and MoO_3. Negative bias corresponds to hole injection from the PEDOT:PSS, positive bias to hole injection from MoO_3. The inset shows the molecular structure of Spiro-TAD. **(b)** Schematic energy-band diagram showing the effective injection barrier (φ_b) between $MoO_3$and the hole-transport layer (HTL). Introducing an interlayer (IL) with a higher IE realigns the Fermi level with the IE of the HTL.[6]

To summarize, it had been demonstrated that: For TMOs with work functions between the LUMO and HOMO of the organic molecules, the HOMO energy offsets follow the Schottky-Mott rule. For TMOs with work functions exceeding LUMO or HOMO limits, the LUMO or HOMO energy offsets will be pinned to the substrate Fermi levels. If the LUMO of the N-type material for electron and HOMO of the P-type material for hole can be pinned to the work function of the transport layer, a loss-less charge transfer can be achieved. This infers that an electron transport layer with much lower low work function and a hole transport layer with much higher work function are preferable.

2.2 Enhancing Absorption Spectrum by Using Tandem Solar Cells

In order to break the Shockley−Queisser limit, tandem structure has been applied to minimize the thermal loss and maximize the absorption spectrum. As shown in **Figure 2-3**, in single-junction cells, photons with energy lower than E_g cannot be absorbed by the active layer materials while photons with energy higher than E_g produce hot carriers, which will be thermalized to band edge by phonon interaction and dissipate excessive energy. As a result, more than half of the energy losses come from the spectral losses.[7] To solve this problem, the tandem devices are composed of two or more junctions having different E_g. Higher energy photons can be absorbed by the top sub-cell with large bandgap and the lower energy photons will pass through the first sub-cell and be absorbed by the next small bandgap sub-cell. This design widens the range of the solar spectrum to maximize absorption and minimize the thermal loss from the difference between incoming photon energy and bandgap. For tandem solar cells based on two junctions under 1 sun intensity, the optimized combination of bandgaps was calculated to be respectively 1.9 and 1.0 eV to achieve a maximum efficiency of 42%.[8]

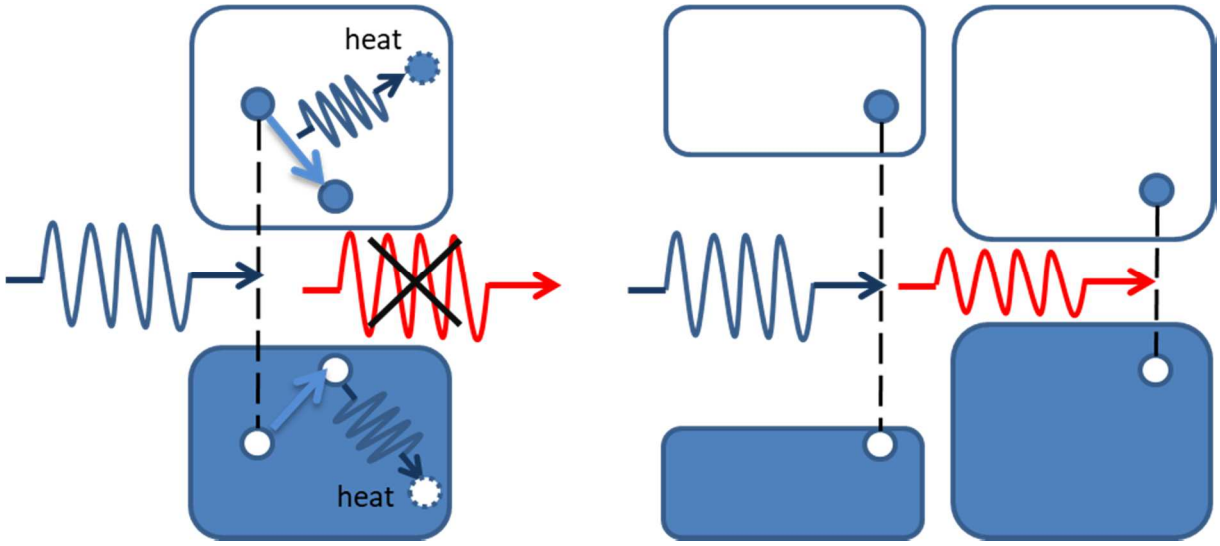

Figure 2-3 The comparison of thermal loss and spectrum loss issues in single and tandem solar cells.

Tandem solar cells can be classified by how the sub-cells are connected to guide out the electricity. Four terminal tandem solar cells are two sub-cells with each's own anode and cathode, in which the high E_g sub-cell is superimposed on the low E_g one. A spectral splitting dichromatic mirror may be used to waive the stacked structure since the mirror distributes the specific light to each sub-cell.[9] The devices can thus be fabricated separately and electrically connected through external circuit. In two-terminal type, the whole device is fabricated sequentially onto one substrate, which the sub-cells are connected through an interconnecting layer. Interconnecting layer is the exchange center where charge carriers from different sub-cells can recombine for maintaining charge neutrality by a tunneling junction or a metallic recombination layer.[10]

2.3 Enhancing Absorption Spectrum by Using Ternary Solar Cells

The other method to improve the total absorption spectrum is using ternary blend in the bulk heterojunction active layer. If the original P-type and N-type material cannot capture

enough photons, adding third light-sensitive component is a simple solution when considering the morphological feature of bulk heterojunction layer.[11] In a ternary organic solar cell, an IR sensitizer is typically chosen as third material to the original binary system. The ternary structure, unlike tandem structure, does not tackle the detailed balance limit, but rather improve the photon harvesting in thickness limited photoactive layers instead. To further realize the physics in the ternary solar cell, we should know that the charge transfer and transport in the ternary blend is more than a simple superposition of the charge transfer and transport properties of the individual phases. **Figure 2-4** illustrates different energy level combination in ternary solar cell.[12] The first transport model is called cascade charge transfer. The relative energetic position of the sensitizer's electronic levels with respect to the ones of host donor and acceptor determines the feasibility of a cascade exciton dissociation and charge transfer among donor/sensitizer/acceptor interfaces. There are several possible pathways which are energetically relevant for the relaxation of photoexcited states in ternary system. The photoexcited donor may transfer an electron to either acceptor or the sensitizer phase. In the latter case, the sensitizer subsequently has to transfer an electron to acceptor for charge collection, and vice versa.

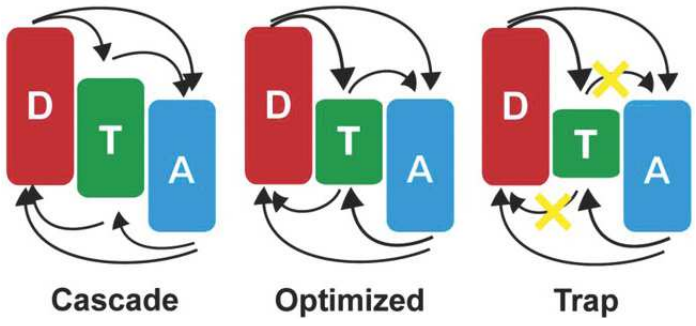

Figure 2-4 Schematic diagrams of different models for charge transfer.[12]

However, there are two challenging issues for ternary solar cell: potential charge recombination in the narrow gap material, miscompatibility between each component.[11,13,14] As seen from **Figure 2-3**, if the bandgap of the third component is too narrow, the charge recombination traps will be formed. The miscompatibility will take place if the chemical structures of donor/acceptor and the third component are different, which may worsen the phase separation in the active layer and impede the charge transport route of the donor/acceptor binary blend active layer.[15] A better microstructure must insert the sensitizer directly at the interface between the host donor and acceptor. If the chemical structure of the third component can be designed to be similar to the original binary system and its LUMO energy level similar to the acceptor and HOMO energy level similar to the donor, an optimized ternary can be achieved, which free charge carriers can be transferred through sensitizer to donor or acceptor materials without encountering energy barrier.

2.4 Organic Tandem Solar Cells

In serial-connected organic tandem solar cell, the energetic diagram of the device can be represented as in **Figure 2-5**.[16] The front sub-cell comprises a donor and an acceptor that are either stacked on each other or mixed. The intermediate layer/interconnecting layer must align of the quasi-Fermi level of the acceptor of the front cell with the quasi-Fermi level of the donor of the rear cell in a normal type solar cell (Anode in the lower position and cathode in the upper position). In inverted device, the alignment should be assured in the corresponding way. The alignment allows the interconnecting layer to recombine electrons from one sub-cell and holes from the other side. To determine the performance of an organic tandem solar cell, the voltage across the whole serial-connected tandem solar cell is equal to the sum of the voltage across each sub-device according to the Kirchhoff's law. We can write: $V_{OC1}+V_{OC2}+V_{OC3}=\ldots V_{Tandem}$. The total current should be determined by the sub-cell with smallest short circuit current.

Over the last 2 decades, there has been an increasing trend of the publications of organic tandem solar cells. Different strategies have been employed based on different photoactive materials and the interconnecting layer. The first application of tandem structure in organic solar cell was published in 1990.[17] It was comprised of two stacked, serial-connected sub-cells based on evaporated small molecules. In the scope of this thesis, all solution-processed active layer type was firstly demonstrated in 2006.[18-20] After one year, the breakthrough in solution-processed tandem cells was achieved demonstrating a high efficiency tandem device showing a 38% performance improvement *versus* the best single device by the use of inverted structure, new solution-processed interconnecting layer, better absorption spectrum coverage.[21] To make a better double-junction organic tandem solar cell, new design of low bandgap polymer has been deemed as

an important way since the scarcity of good low bandgap polymer in the previous development era of organic solar cell. A New low bandgap polymer PBDTT-DPP with improved quantum efficiency (50%) at long wavelength, and successfully achieved an inverted tandem PSC with PCE of certified 8.6%.[22-24] In the following work, the technical milestone to break 10% barrier was firstly done by employing a low bandgap polymer PDTP-DFBT in the rear cell.[25] In general, the progress of organic tandem solar cell follows the new synthesis of highly efficient polymers and small molecules with complementary absorption spectra.

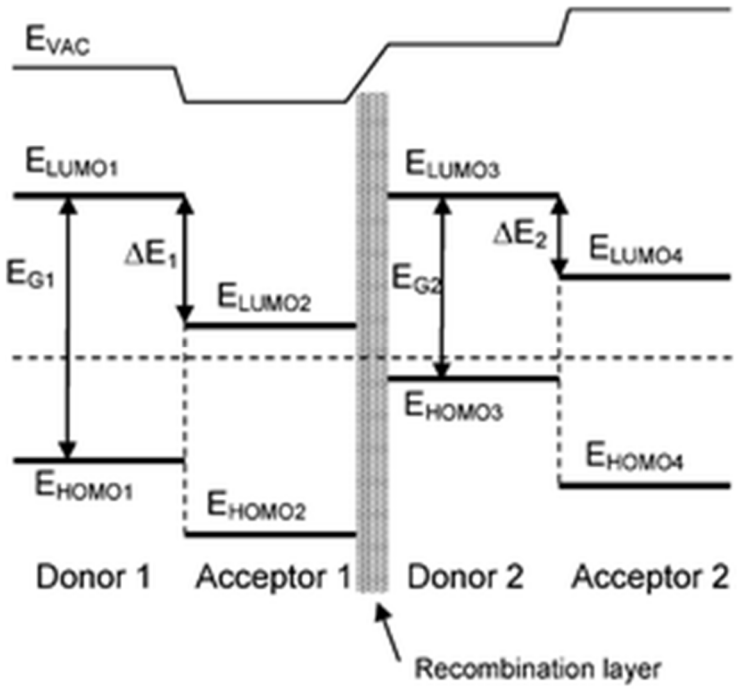

Figure 2-5 Simplified band diagram of a tandem cell made of two sub-cells connected in series via a recombination layer.[16]

2.5 Challenges

The development of organic solar cell is thriving thanks to the discovery of new photoactive materials and advanced device structure as introduced in previous chapters. However, several critical issues still exist which hamper the further improvement.

For the charge transport layer of single junction devices and interconnecting layer of tandem devices, the solution-processable materials with good charge mobility and interface morphology are needed.[26] The preparation of appropriate transport layer is definitely tricky since the film formation process is involving interactions between processing solvent, donor/acceptor materials and base layer. The most common used transport materials in organic solar cell are sol-gel and nanocrystal metal oxides because of the easiness of layer preparation in relatively low temperature annealing process. Nonetheless, low charge carrier density, low mobility, work function tenability and surface modification remain major challenges.

Second, although the theoretical efficiency of organic tandem solar cell is higher than single junction type, the latter still have a higher certified efficiency. There are some causes for this embarrassing situation. In general, fabrication of two-terminal organic tandem solar cells is challenging because of the current matching of each sub-cell and the limitation in the fabrication process. Because the equivalent circuit of tandem solar cell can be illustrated as diodes linked together, the total device current will be confined to the sub-cell with the smallest short circuit current. It can be imagined as: when external voltage is applied, the sub-cell with higher current is relatively forward biased while the sub-cell with smaller current is reversed biased. As a result, the excessive short circuit current is flow in forward bias condition, which cannot provide power to the all tandem solar cell. Speaking of the process limitation, the bottom devices should have strong enough chemical and mechanical durability to survive the processes of the following

functional layers. The thing that casting a further layer from solution dissolves the underneath layer has to be avoided. Besides, the energy levels of each sub-cells should be suitable with the interconnecting layer as informed in last paragraph.

References

1. Braun, S., Salaneck, W. R., & Fahlman, M. (2009) Energy□level alignment at organic/metal and organic/organic interfaces. *Adv. Mater*. *21*, 1450-1472.

2. Greiner, M. T., Helander, M. G., Tang, W. M., Wang, Z. B., Qiu, J., & Lu, Z. H. (2012) Universal energy-level alignment of molecules on metal oxides. *Nat. Mater*. *11*, 76-81.

3. Greiner, M. T., Chai, L., Helander, M. G., Tang, W. M., & Lu, Z. H. (2012) Transition metal oxide work functions: the influence of cation oxidation state and oxygen vacancies. *Adv. Funct. Mater*. *22*, 4557-4568.

4. Ley, L., Smets, Y., Pakes, C. I., & Ristein, J. (2013). Calculating the Universal Energy□ Level Alignment of Organic Molecules on Metal Oxides. *Adv. Funct. Mater*. *23*, 794-805.

5. Chai, L., White, R. T., Greiner, M. T., Lu, Z. H. (2014). Experimental demonstration of the universal energy level alignment rule at oxide/organic semiconductor interfaces. *Phys. Rev. B. 89*, 035202.

6. Kotadiya, N. B., Lu, H., Mondal, A., Ie, Y., Andrienko, D., Blom, P. W., Wetzelaer, G. J. A. (2018). Universal strategy for Ohmic hole injection into organic semiconductors with high ionization energies. *Nat. Mater. 17*, 329-334.

7. Shockley, W.; Queisser, H. J. (1961) Detailed balance limit of efficiency of p-n junction solar cells. *J. Appl. Phys. 32*, 510-519

8. De Vos, A. (1980) Detailed balance limit of the efficiency of tandem solar cells. *J. Phys. D: Appl. Phys. 13*, 839.

9. Yum, J.-H.; Lee, J.-W.; Kim, Y.; Humphry-Baker, R.; Park, N.-G.; Grätzel, M. (2014) Panchromatic light harvesting by dye-and quantum dot-sensitized solar cells. *Solar Energy 109*, 183-188.

10. Bailie, C. D.; McGehee, M. D. (2015) High-efficiency tandem perovskite solar cells. *MRS Bull. 40*, 681-686.

11. Ameri, T., Khoram, P., Min, J., & Brabec, C. J. (2013). Organic ternary solar cells: a review. *Adv. Mater*. *25*, 4245-4266.

12. Cheng, Pei, et al. (2018). Unique energy alignments of a ternary material system toward high□performance organic photovoltaics. *Adv. Mater*. 1801501.

13. Savoie, B. M., Dunaisky, S., Marks, T. J., Ratner, M. A. (2015). The scope and limitations of ternary blend organic photovoltaics. *Adv. Energy Mater, 5*, 1400891.

14. Huang, W., Cheng, P., Yang, Y., Li, G., Yang, Y. (2018). High□performance organic bulk□heterojunction solar cells based on multiple□donor or multiple□acceptor components. *Adv. Mater*. *30*, 1705706.

15. Machui, F., Rathgeber, S., Li, N., Ameri, T., Brabec, C. J. (2012). Influence of a ternary donor material on the morphology of a P3HT: PCBM blend for organic photovoltaic devices. *J. Mater. Chem. 22*, 15570-15577.

16. Ameri, T., Dennler, G., Lungenschmied, C., Brabec, C. J. (2009). Organic tandem solar cells: A review. *Energy Environ., Sci. 2*, 347-363.

17. Hiramoto, M., Suezaki, M., & Yokoyama, M. (1990). Effect of thin gold interstitial-layer on the photovoltaic properties of tandem organic solar cell. *Chem. Lett. 19(3)*, 327-330.

18. Kawano, K., Ito, N., Nishimori, T., & Sakai, J. (2006). Open circuit voltage of stacked bulk heterojunction organic solar cells. *Appl. Phys. Lett. 88*, 073514.

19. Dennler, G., Prall, H. J., Koeppe, R., Egginger, M., Autengruber, R., & Sariciftci, N. S. (2006). Enhanced spectral coverage in tandem organic solar cells. *Appl. Phys. Lett. 89*, 073502.

20. Hadipour, A, et al. (2006). Solution□processed organic tandem solar cells. *Adv. Funct. Mater. 16*, 1897–1903

21. Kim, J. Y., Lee, K., Coates, N. E., Moses, D., Nguyen, T. Q., Dante, M., & Heeger, A. J. (2007). Efficient tandem polymer solar cells fabricated by all-solution processing. *Science 317*, 222-225.

22. Chou, C. H., Kwan, W. L., Hong, Z., Chen, L. M., & Yang, Y. (2011). A metal□oxide interconnection layer for polymer tandem solar cells with an inverted architecture. *Adv. Mater. 23*, 1282-1286.

23. Dou, L, et al. (2012). Tandem polymer solar cells featuring a spectrally matched low-bandgap polymer. *Nat. Photonics 6*, 180–185

24. Dou, L, et al. (2012). Systematic investigation of benzodithiophene-and diketopyrrolopyrrole-based low-bandgap polymers designed for single junction and tandem polymer solar cells. *J. Am. Chem. Soc. 134*, 10071-10079.

25. You, J. et al. (2013). A polymer tandem solar cell with 10.6% power conversion efficiency. *Nat. Commun*. *4*, 1446.

26. Yip, H. L., Jen, A. K. Y. (2012). Recent advances in solution-processed interfacial materials for efficient and stable polymer solar cells. *Energy Environ. Sci*. *5*, 5994-6011.

Chapter 3 High Mobility Indium Oxide Electron Transport Layer in Organic Photovoltaics

(This chapter is based on the publication, *Nano Lett. 2018, 18, 5805-5811*)

The electron transport layer (ETL) plays an important role in determining the device efficiency of organic solar cells. A rational design of an ETL for organic solar cell aims high charge extraction and induction of optimized active layer morphology. In this chapter, a high mobility In_2O_3 synthesized via a solution-processed combustion reaction was successfully used as a universal ETL in an organic solar cell. After modifying the surface by a thin polyethylenimine ethoxylated (PEIE) layer, a device based on crystalline In_2O_3 outperforms its counterpart, Zinc Oxide (ZnO), in both polymer PBDTTT-EFT-based fullerene and non-fullerene systems. As In_2O_3 was applied to ETL, the average efficiency increased from 9.5% to 10.5% for PBDTTT-EFT− $PC_{71}BM$ fullerene-based organic solar cells and also increased from 10.8% to 11.5% for PBDTTT-EFT−IEICO-4F non-fullerene-based organic solar cells, respectively. In the morphological studies of the transport layer materials, it has been discovered the fact that the crystalline In_2O_3 thin film has highly aligned nano-scale morphology. This morphological feature induced the crystallization of polymer into a preferential molecular packing enhancing the charge transport from active layer to ETL. From the photophysical study, it has also found that charge extraction in the crystalline In_2O_3 device is significantly faster than

in the ZnO device due to the higher mobility of In_2O_3 and optimized nanomorphology of the active layer.

3.1 Motivation

As described in the previous chapters, the ETL plays an important role in determination of organic solar cell device performance. The ETL can not only enhance electron extraction and reduce charge recombination but also influence the morphology of active layer. The metal oxide-based ETLs specifically have attracted immense attention due to their highly transparent nature and tunable energy levels and electrical properties achieved through doping or chemical modification.[18] A number of metal oxides such as pristine and doped ZnO [19-22] and TiO_2 [21,23] have been already synthesized and employed in the inverted OPV. However, both ZnO- and TiO_2-based ETLs suffer from their relative low mobility. Hence, it is necessary to develop a high mobility alternative metal oxide such as SnO_2 and In_2O_3 for facilitating charge extraction and achieving better device efficiency.[24,25]

In this Chapter, we report a solution-processed high mobility In_2O_3 ETL. The In_2O_3 ETL was achieved by using indium nitrate hydrate as a precursor mixed with a small amount of additives to lower its annealing temperature below 300 °C via a combustion reaction.[26,27] By rational selection of metal oxide precursors and additives, a strong exothermic combustion reaction can be stimulated to form high quality In_2O_3 films at low temperatures, facilitating the subsequent fabrication processes of OPV.[28] The two design rules for an excellent ETL are able to collect the electron charge carrier in an efficient way and to induce a favorable active layer morphology. The solution-processed In_2O_3 incorporates both of these two aspects. The mobility of In_2O_3 increases up to 15 $cm^2/(V \cdot s)$, which is 1 order of magnitude higher than the one of solution-processed ZnO, which can significantly improve the charge extraction. In addition, by combining the microscopy and scattering results, it becomes clear that the crystalline In_2O_3 layer exhibits a preferential orientation with the (222) plane either parallel or perpendicular to the glass

substrate, which consequently induces crystallization of the polymer into a highly ordered crystallite orientation.

A model system, the blend of poly[[2,60–4,8-di(5-ethylhexylthienyl)benzo[1,2-*b*;3,3-*b*]dithiophene]3-fluoro-2[(2-ethylhexyl)carbonyl]thieno[3,4-*b*]thiophenediyl] (PTB7-Th, also called PBDTTT-EFT) with $PC_{71}BM$ (shown in **Figure 3-1(a)**), was used to compare the device performance based on three different ETLs: crystalline In_2O_3 (c-In_2O_3, annealed at 300 °C), amorphous In_2O_3(a-In_2O_3, annealed at 200 °C), and ZnO (annealed at 200 °C).[29−32] As shown in **Figure 3-1(b)**, devices were fabricated with a structure of ITO/ETL/PEIE/ PTB7-Th–$PC_{71}BM$/MoO_3/Ag. A thin layer of PEIE was used to tune the work function of metal oxide for a better charge extraction and minimize the pinhole density in the In_2O_3 ETL.[33] Device based on the PEIE-modified c-In_2O_3exhibit an average power conversion efficiency (PCE) of 10.5%, showing an enhancement by over 10% compared with its PEIE-modified ZnO counterpart. The photocurrent decay measurement reveals an improved charge extraction in the c-In_2O_3 device. In addition to PTB7-Th–$PC_{71}BM$ fullerene-based solar cells, devices based on c-In_2O_3 also show the superior photovoltaic performance compared to the devices based on ZnO in PBDTTT-EFT–IEICO-4F non-fullerene solar cells. An average efficiency of 11.5% is achieved by using the c-In_2O_3 ETL in PBDTTT-EFT–IEICO-4F solar cells.

3.2 Result and discussion

3.2.1 Optical Property and Crystallographic Analysis of In_2O_3 Thin Film

ETLs need to be highly transparent for sufficient light transmittance. Therefore, In_2O_3 is a suitable candidate because its energy gap is greater than 3 eV.[34] The transmission spectrum (**Figure 3-2(a)**) shows that c-In_2O_3 film has a very low absorption in the visible region. The transmittance in the region between 400 and 800 nm is above 95%. The c-In_2O_3 crystals are

homogeneous and compactly packed on the surface of ITO (**Figure 3-2(b)**). From the X-ray diffraction results (**Figure 3-2(c)**), the occurrence of crystallization is observed in In_2O_3 film annealed at 300 °C. The peak located at $2\theta = 30.6°$ corresponds to the scattering from the (222) peak. However, due to thin c-In_2O_3 film and low X-ray flux, a low scattering intensity was observed in the lab-based X-ray scattering measurement. A synchrotron-based grazing incidence wide-angle X-ray scattering (GIWAXS) was also employed to further probe the crystallization behavior of the c-In_2O_3 film with a significantly higher X-ray flux. The crystallite information, such as the crystallite orientation, could also be monitored using a 2D detector. From the 2D scattering pattern of c-In_2O_3 film (**Figure 3-2(d)**), a strong intense peak at $q = 2.1$ $Å^{-1}$ corresponds to the (222) plane. This (222) scattering peak was observed only along the out-of-plane (OOP) or in-plane (IP) direction, suggesting that the (222) plane of In_2O_3 crystallites was either parallel or perpendicular to the substrate. As the annealing temperature decreases to 200 °C, the In_2O_3 film showed a totally amorphous microstructure. There was no scattering peak from the a-In_2O_3 film annealed at 200 °C in both lab-based and synchrotron-based scattering measurements.

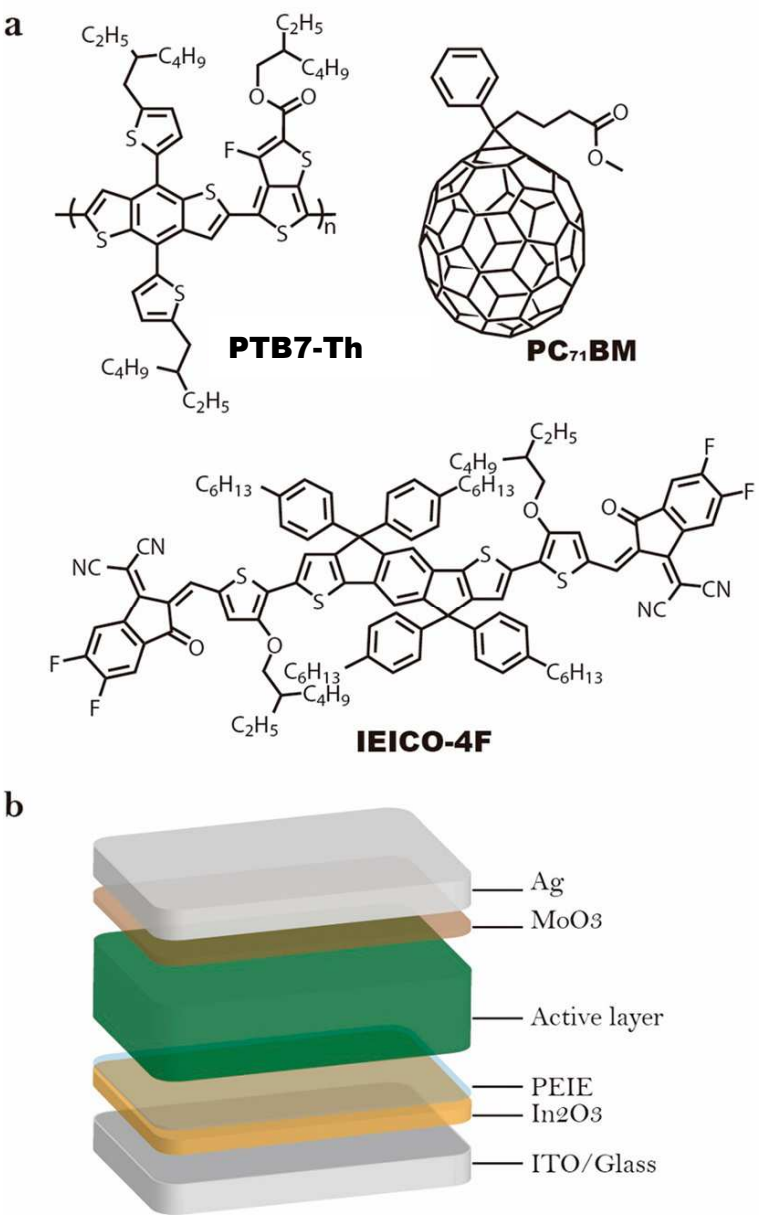

Figure 3-1 Molecular structure of PTB7-Th, $PC_{71}BM$, and IEICO-4F. (b) Schematic of the inverted organic solar cell based on a structure of ITO/In_2O_3/PEIE/active layer/MoO_3/Ag.

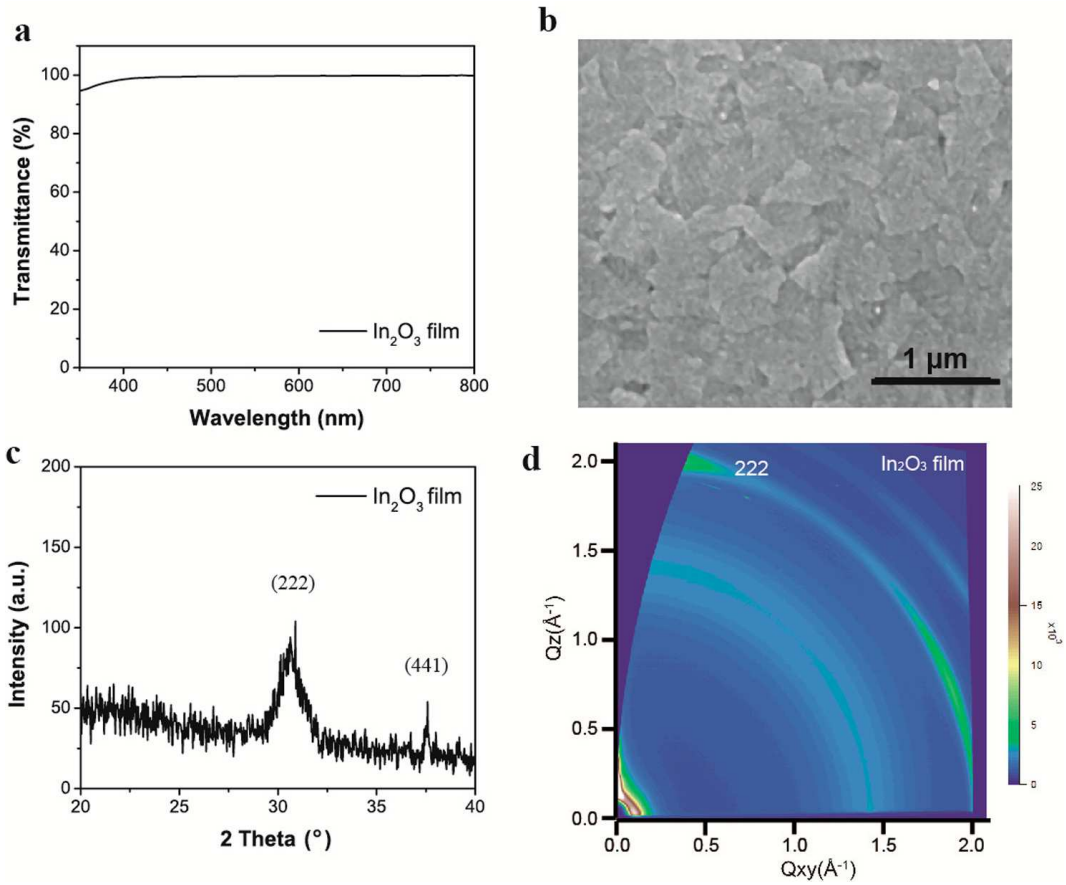

Figure 3-2 Optical properties and morphology of In_2O_3 thin film. **(a)** Transmittance spectra of c-In_2O_3 film on the glass substrate. **(b)** Scanning electron microscope (SEM) image of c-In_2O_3 film on the ITO coated glass. **(c)** Lab-based X-ray diffraction (XRD) spectra of the c-In_2O_3 film. **(d)** Grazing incidence wide-angle X-ray scattering (GIWAXS) pattern of the c-In_2O_3 film.

3.2.2 Electrical Properties of Indium Oxide Thin Films

In order to characterize the electrical performance of In_2O_3 films, In_2O_3-based thin-film transistors (TFTs) were fabricated with a bottom-gate and top-contact (BGTC) structure. A typical transfer curve of c-In_2O_3 TFT is illustrated in **Figure 3-3(a)**, with an annealing temperature at 300 °C. Extracted from this transfer curve, the mobility of In_2O_3 film annealed at 300 °C was measured to be 15.1 $cm^2/(V \cdot s)$. The device shows a turn-on voltage at around 0 V and a high on/off ratio of 10^7. The mobility increases to 25.5 $cm^2/(V \cdot s)$ as the annealing temperature is increased to 350 °C, as illustrated in **Figure 3-3(b)**. The amorphous In_2O_3 TFTs annealed at 200 °C also show a high saturation mobility of about 1.0 $cm^2/(V \cdot s)$.

The oxygen binding state plays an important role in determining the mobility of the In_2O_3 films.[34] **Figure 3-3(c)** compares the X-ray photoelectron spectroscopy (XPS) O 1s spectrum of c-In_2O_3 and a-In_2O_3 films. There are two peaks located at 532.1 and 530.4 eV, representing the hydroxide bonding and oxide lattice, respectively.[28] Compared with the a-In_2O_3 film, the peak area related to the oxide lattice shows a dramatic increase in the c-In_2O_3 film, confirming a better crystalline microstructure. Meanwhile, the peak area corresponding to the hydroxide bonding slightly decreases in the c-In_2O_3 film. In this study, in order to further improve the charge extraction at the interface between the ETL and active layer, all ETLs were modified by using a dipole layer PEIE, which allows for tuning of their work functions and reducing pinhole defects.[33,35] The work functions of c-In_2O_3 film modified with and without PEIE were measured by ultraviolet photoemission spectroscopy (UPS), as shown in **Figure 3-3(d)**. The UPS spectra reveal that the work function of c-In_2O_3 film decreases 0.4 V after modification of the thin layer of PEIE, improving the charge injection at the interface between the ETL and active layer.

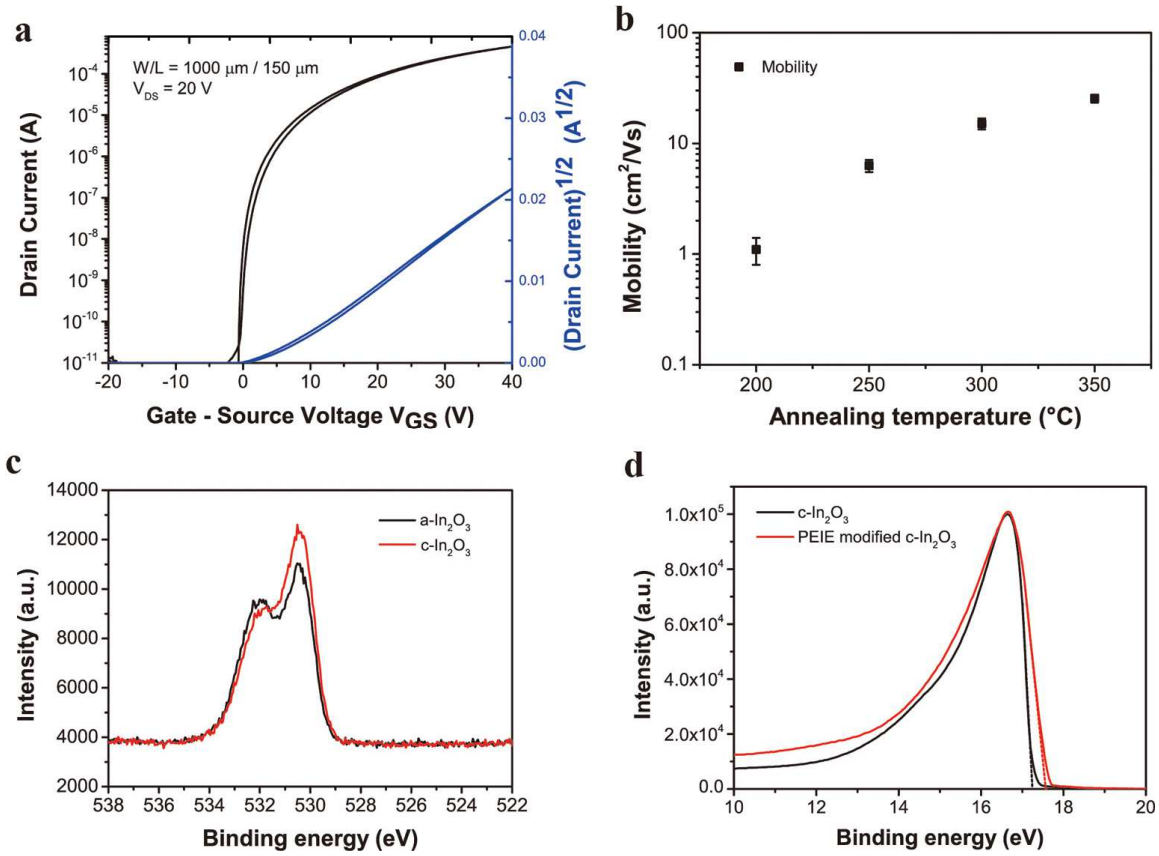

Figure 3-3 Electrical properties of In_2O_3 thin film. **(a)** Electrical performance of c-In_2O_3 thin-film transistors (TFT). The device structure is bottom-gate and top-contact, and the c-In_2O_3 thin film is annealed at 300 °C, **(b)** The saturation mobility of In_2O_3 TFT as a function of annealing temperature. **(c)** X-ray photoelectron spectroscopy (XPS) O 1s spectra of c-In_2O_3 and a-In_2O_3. **(d)** Ultraviolet photoelectron spectroscopy (UPS) spectra of c-In_2O_3 modified with and without PEIE.

3.2.3 Device Performances

All devices were fabricated with an inverted structure of ETL/PEIE/active layer/MoO_3/Ag. The active layers were prepared by using the same solution with a donor/acceptor weight ratio of 1:1.5. **Figure 3-4** presents the average photovoltaic performance of organic solar cells based on different ETLs: ZnO, c-In_2O_3, and a-In_2O_3. (All of the photovoltaic parameters are summarized in **Table 3-1**.) **Figure 3-4(a)** demonstrates the current–voltage (*J-V*) characteristics under a light intensity of 100 mW/cm^2. The device based on ZnO exhibits an average PCE of 9.5% with a short circuit current (J_{sc}) of 16.9 mA/cm^2, an open-circuit voltage (V_{oc}) of 0.82 V and a fill factor (FF) of 0.69. When ZnO is replaced by c-In_2O_3 (annealed at 300 °C), the device PCE shows an enhancement by over 10%, significantly increasing from 9.5% to 10.5%. The main reason for the improved device performance is attributed to the increased J_{sc} from 16.9 to 18.9 mA/cm^2. From the EQE measurement (**Figure 3-4(b)**), it is noted that the EQE spectra of the device based on c-In_2O_3 show higher values over the whole visible region between 400 and 800 nm. The maximum EQE value in the c-In_2O_3 device reaches over 80% at the wavelength of 725 nm. The integrated J_{sc} values from EQE spectra are 16.4 mA/cm^2 for ZnO and 18.4 mA/cm^2 for c-In_2O_3, respectively. (The difference between J_{sc} values measured from *J-V* curves and integrated from EQE spectra is less than 5%.) The enhancement in the integrated EQE value showed a good agreement with the enhancement in J_{sc}.

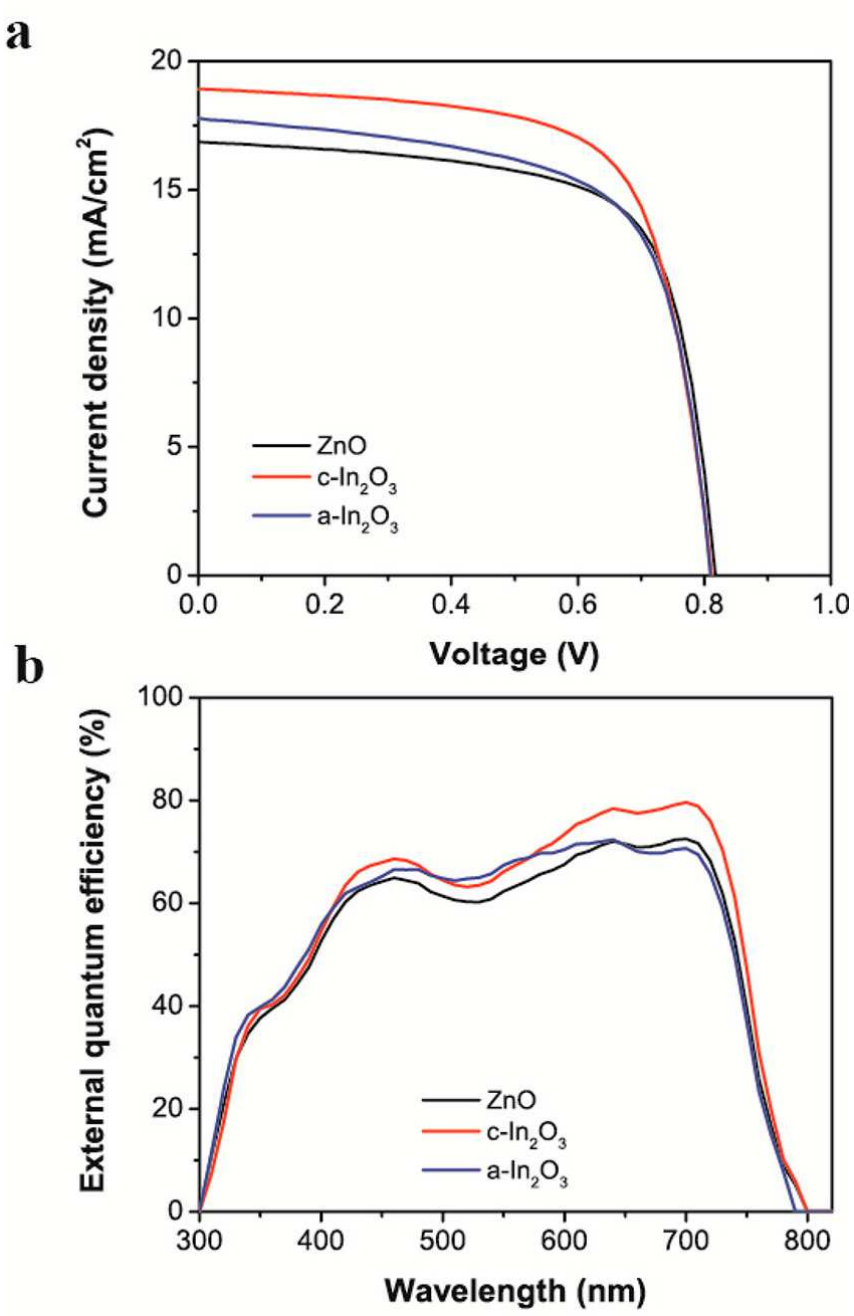

Figure 3-4 Device performance of PTB7-Th–$PC_{71}BM$ organic solar cells based on various ETLs: ZnO, c-In_2O_3, and a-In_2O_3. (a) Current density–voltage (*J-V*) curve and (b) external quantum efficiency (EQE) spectra.

Active layer	ETL	Efficiency (%)	V_{OC} (V)	J_{sc} (mA/cm^2)	Fill factor	Rs (Ωcm^2)	Rsh (Ωcm^2)
PTB7-Th–$PC_{71}BM$	ZnO	9.5 (±0.2)	0.82 (±0.1)	16.9 (±0.2)	0.69 (±0.2)	5.0	803
PTB7-Th–$PC_{71}BM$	c-In_2O_3	10.5 (±0.3)	0.81(±0.2)	18.9 (±0.5)	0.69 (±0.3)	4.7	821
PTB7-Th–$PC_{71}BM$	a-In_2O_3	9.5 (±0.4)	0.81 (±0.1)	17.7 (±0.4)	0.66 (±0.3)	4.6	624
PTB7-Th–IEICO-4F	ZnO	10.8 (±0.3)	0.71 (±0.1)	22.1 (±0.3)	0.69 (±0.2)	3.2	456
PTB7-Th–IEICO-4F	c-In_2O_3	11.5 (±0.3)	0.71 (±0.2)	23.7 (±0.4)	0.68 (±0.3)	2.8	414
PTB7-Th–IEICO-4F	a-In_2O_3	10.8 (±0.4)	0.71 (±0.1)	22.3 (±0.4)	0.68 (±0.2)	2.9	402

Table 3-1 Average Device Performance of Organic Solar Cells Based on Various ETLs

The PCEs of devices based on the In_2O_3 ETL are sensitive to the annealing temperature. As the annealing temperature is decreased to 200 °C, the efficiency slightly decreased to 9.5%, which is similar to the one in devices based on the ZnO ETL. The device yields a J_{sc} of 17.7 mA/cm^2 (17.1 mA/cm^2 calculated from EQE), a V_{oc} of 0.81 V, and a fill factor of 0.66. As shown in **Figure 3-5**, device PCEs show a monotonical increase with the annealing temperature in the region between 200 and 300 °C. The change in device performance is mainly attributed to the mobility of the In_2O_3 ETL. As the annealing temperature continues to increase to 350 °C, the mobility of In_2O_3 further increases to 25 cm^2/(V·s), while the PCE slightly decreases to 10.2%.

The possible explanations to this phenomenon are the formation of plenty of pinholes in In_2O_3 films and the increase of ITO resistance under such high temperature annealing.

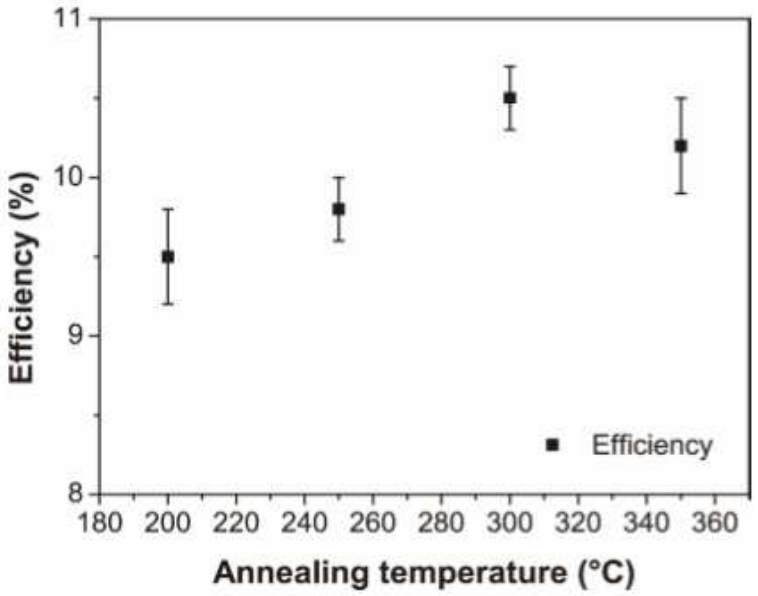

Figure 3-5 Power conversion efficiency of organic solar cells based on the In_2O_3 ETL with different annealing temperatures.

In addition to the PTB7-Th–$PC_{71}BM$ fullerene-based system, we also compared device performance of a non-fullerene system based on different ETLs (**Figure 3-6**). The device fabricated by ZnO shows an average efficiency of 10.8% with a J_{sc} of 22.1 mA/cm^2, a V_{oc} of 0.71 V, and a fill factor of 0.69 and the device based on a-In_2O_3 shows a similar average efficiency compared to the one based on ZnO. Among three different ETLs, the highest average efficiency (11.5%) was achieved in a device based on c-In_2O_3. Similar to the PTB7-Th–$PC_{71}BM$ blend, the c-In_2O_3 device also exhibits the highest J_{sc} among PTB7-Th–IEICO-4F solar cells. Compared with the ZnO device, the J_{sc} of the c-In_2O_3 device increases to 23.7 mA/cm^2. The increased short

circuit current is also the main reason for the efficiency improvement in this non-fullerene solar cell.

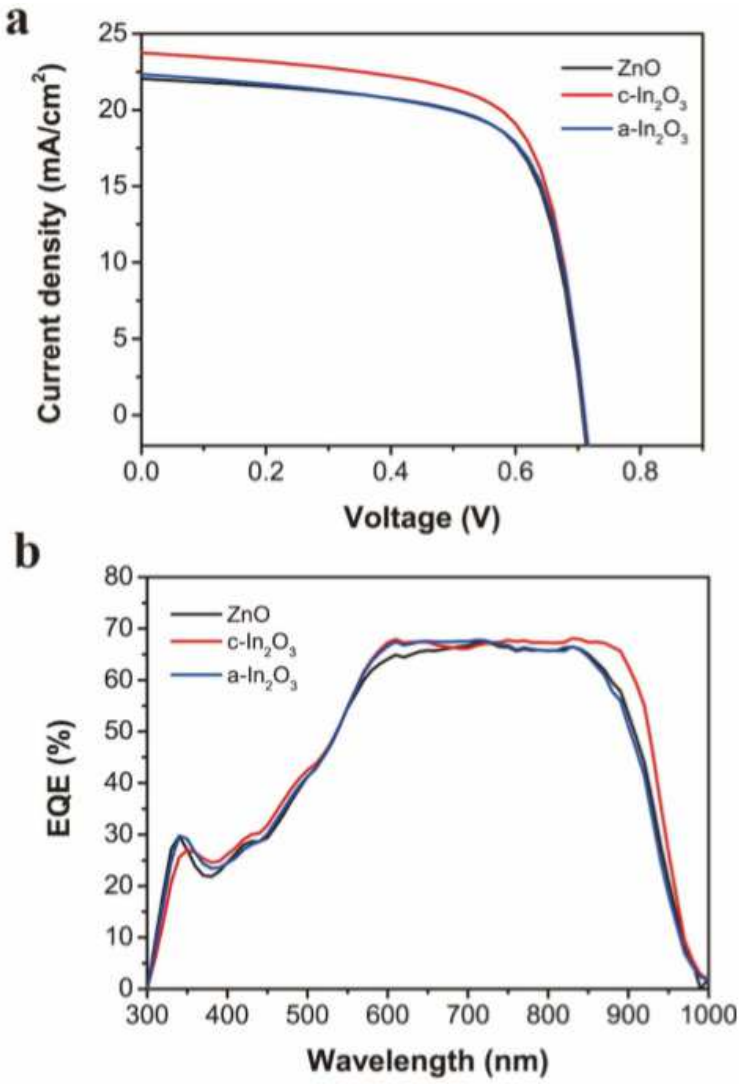

Figure 3-6 Device performance of PTB7-Th:IEICO-4F organic solar cells based on various ETLs: ZnO, c-In_2O_3 and a-In_2O_3. (a) Current density-voltage (J-V) curve and (b) external quantum efficiency (EQE) spectra.

3.2.4 Device Transport Properties Analysis by Crystallographic Data

In order to probe the effect of the underlying layer on the active layer nanomorphology and device physics, the PTB7-Th–$PC_{71}BM$ blend was taken as a model system to investigate the crystallization behavior of the polymer (i.e., crystalline orientation) and charge extraction at the interface between the ETL and active layer.[36,37] The two-dimensional GIWAXS scattering patterns of PTB7-Th–$PC_{71}BM$ blends based on three different ETLs (ZnO, c-In_2O_3, and a-In_2O_3) are presented in **Figure 3-7(a)–(c).** A prominent (100) reflection was found at $q = 0.31$ $Å^{-1}$, which corresponds to alkyl stacking.[32,35] From the peak position, the alkyl stacking distance was calculated to be 2.03 Å, which was similar to our previous measurement.[35,38] The (100) reflection in both In_2O_3 samples shows the significantly higher intensity than the ZnO sample. The coherence length of polymer crystallite was calculated from full width at half maximum (FWHM) of scattering peak by using the Scherrer equation. The fitted parameter of polymer (100) peak is summarized in **Table 3-2**. Polymer deposited on both In_2O_3 ETLs showed a large coherence length (8.2 nm for c-In_2O_3 and 8.1 nm for a-In_2O_3) than that on ZnO (7.6 nm). This suggests that the In_2O_3-based ETLs can facilitate the crystallization of polymer PTB7-Th.

In addition to crystallinity, the orientation of polymer crystallites is also important for the charge transport. The pole figure of polymer (100) peak was extracted from 2D scattering patterns, as shown in **Figure 3-7(d)**. The polymer films on ZnO and a-In_2O_3 show a similar crystallite orientation that polymer crystallites were almost randomly oriented with a slightly higher intensity along the in-plane direction. However, from the scattering pattern of the c-In_2O_3 sample, it is worth noting that the significantly higher intensities were found along either the out-of-plane or in-plane direction, indicating that the polymer PTB7-Th on the c-In_2O_3 substrate exhibited more aligned crystallites. Such observation could be explained by the

substrate-induced polymer crystallization. The scattering peak located at $q = 2.1$ Å^{-1} was identified as the (222) peak from the c-In_2O_3 film. The (222) c-In_2O_3 peak was largely located along either out-of-plane or in-plane axis, indicating that the oriented crystallites were observed in the c-In_2O_3 film. The highly aligned c-In_2O_3 crystallites have led to the crystallization of polymer PTB7-Th with more ordered orientations. ZnO and In_2O_3 ETLs were modified with a layer of PEIE to tune their work function and minimize pinhole density. The existence of this ultrathin layer could partially compensate the benefit of the underlying In_2O_3 layer on the polymer morphology. However, the thickness of this PEIE layer is less than 10 nm. The crystallization behavior of polymer PTB7-Th is still strongly dependent on the microstructure of the underlying metal oxide.

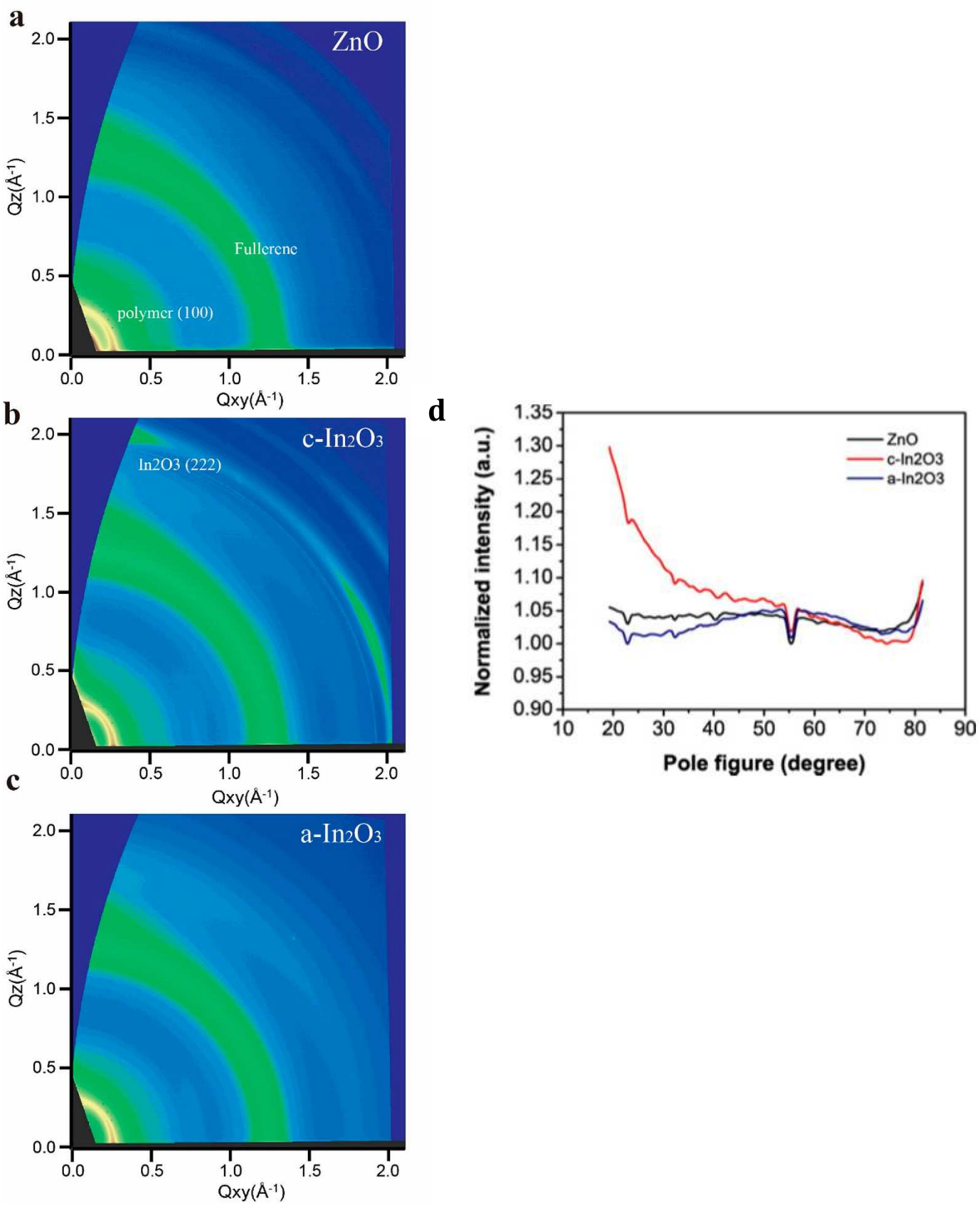

Figure 3-7 2D GIWAXS scattering patterns of PBDTTT-EFT–$PC_{71}BM$ blend on different ETLs: (a) ZnO, (b) c-In_2O_3, and (c) a-In_2O_3. (d) Pole figures of the polymer (100) peak

	FWHM (Å)	Calculated coherence length (nm)
ZnO	0.082	7.6
c-In_2O_3	0.077	8.2
a-In_2O_3	0.078	8.1

Table 3-2 The fitted full width at half maximum (FWHM) of in-plane polymer (100) peak

A broad out-of-plane peak located at q = 1.5 $Å^{-1}$ corresponding to the polymer π–π stacking can be also observed from 2D scattering patterns, but the peak position of the scattering pattern from polymer π–π stacking is close to that from fullerene molecules. In order to distinguish these two peaks, line profiles (out-of-plane and in-plane) were extracted from the 2D scattering patterns by integrating the scattering intensity along the out-of-plane and in-plane directions. As shown in the 1D out-of-plane scattering profiles (**Figure 3-8**), the peak intensity of polymer π–π stacking located at q = 1.5 $Å^{-1}$ in the c-In_2O_3 sample is stronger than that in the a-In_2O_3 and ZnO samples. It indicates that the highly oriented c-In_2O_3 underlying layer leads to the polymer crystallization into a more "face-on" configuration with the π–π stacking direction perpendicular to the substrate. As the charge transport through the π–π stacking direction is faster than that through the side-chain direction, the face-on configuration is considered as a favorable morphology for the efficient charge transport. Combination of the highly ordered crystallite orientation and increased face-on configuration facilitates the charge transport and minimizes the charge recombination possibility in the c-In_2O_3 device.

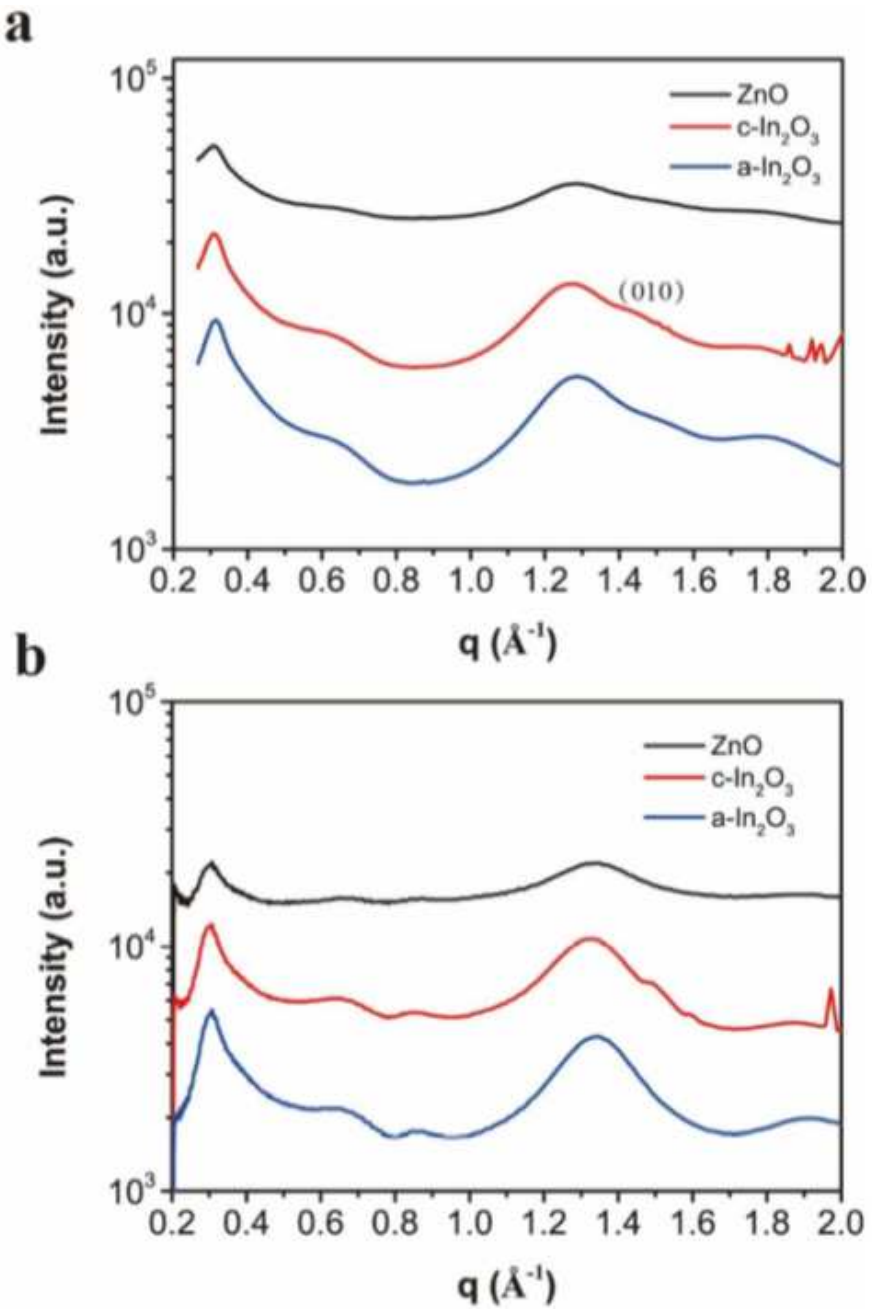

Figure 3-8 Line scattering profiles of blend based on different ELTs cut from 2D GIWAXS patterns: (a) out-of-plane (OOP) direction and (b) in-plane (IP) direction.

3.2.5 Mobility Analysis of Electron Transport Layers

The charge extraction with different ETLs is investigated with a transient photocurrent measurement (TPC), shown in **Figure 3-9**. In this measurement, a constant background illumination is provided by using a white LED with the light intensity of 1 sun equivalent. The RC time constants of the devices are measured to have an order $\leqq$ 0.1μs, which implies the decay mechanism here is not RC time-limited. Among three devices, the c-In_2O_3 device exhibits the fastest photocurrent decay. The photocurrent decay time was derived by using an exponential decrease function. The photocurrent decay time in the c-In_2O_3 device is only 0.46 μs lower than the ones observed in the other two counterparts, ZnO and a-In_2O_3, with the decay times of 0.61 and 0.88 μs, respectively. The transient photocurrent was also measured without the background light illumination and showed a similar trend, where the decay time for the c-In_2O_3 device was the lowest. From the transient photocurrent measurement, it can be concluded that the ETL with the higher mobility is better for charge extraction. The charge extraction in the c-In_2O_3 sample is more efficient than the one in the ZnO sample, which could be the main reason for the enhanced short circuit current.

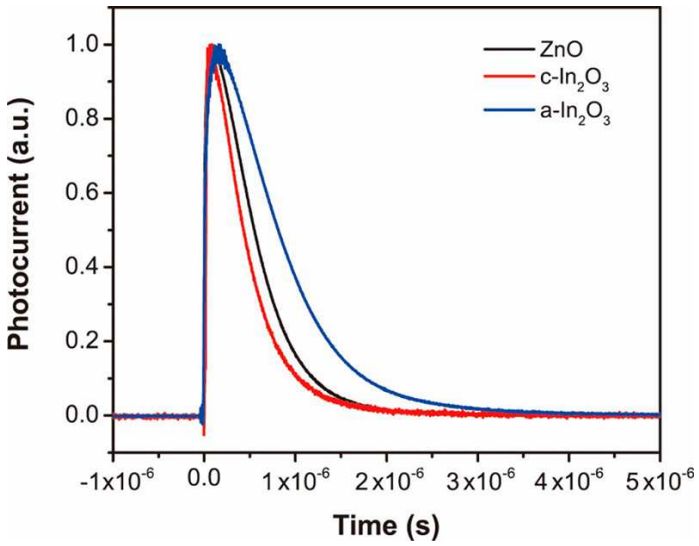

Figure 3-9 Photocurrent decay of organic solar cells based on three different ETLs: ZnO, c-In_2O_3, and a-In_2O_3 undrr light illumination.

Due to its high mobility and wide band gap, the sol–gel-processed In_2O_3 ETL is considered as a promising ETL candidate for solution-processed photovoltaic technologies.[24,39] However, the occurrence of pinholes in the In_2O_3 layer during the annealing process is a critical issue in limiting the device performance.[24] Here, we successfully synthesized a high quality solution-processed In_2O_3 ETL for organic photovoltaic via the incorporation of a small amount of additive, which significantly lowers the processing temperature. The solution-processed In_2O_3 ETLs were modified with a thin layer of PEIE, which effectively minimizes the pinholes and defects in the In_2O_3 layer and tunes the work function of In_2O_3 for a more efficient charge injection. Both fullerene-based and non-fullerene-based organic solar cells with the In_2O_3 ETL appear as a superior device compared to its counterpart, ZnO. The better device efficiency can be explained by the more efficient charge extraction and the more favorable blend morphology. Compared with ZnO film, c-In_2O_3 film shows the significantly

higher mobility. Therefore, the faster charge collection was achieved in c-In_2O_3, resulting in the enhanced short circuit current. In order to fully understand the effects of mobility of ETLs on device performance, a series of In_2O_3 with different annealing temperatures have been systematically studied. It was found that charge extraction shows a strong relationship with the mobility of the underlying ETL. As the annealing temperature decreases from 300 to 200 °C, In_2O_3 exhibits an amorphous microstructure. Although indium oxide shows relatively excellent carrier mobility in the amorphous state compared with other semiconductors, such as silicon due to the different transport mechanisms, a lower processing temperature still leads to the increased trap states, which are confirmed by the XPS measurement.[34,40,41] Compared with the crystalline indium oxide, significantly poorer charge extraction and higher recombination have been observed in the device with the amorphous indium oxide. Moreover, it is interesting to note that the morphology of the active layer is sensitive to the microstructure of the underlying ETL. If the underlying layer exhibits some preferential orientations, it could act as a template to induce polymer crystallization into a certain orientation. Compared with ZnO and a-In_2O_3, the more highly aligned crystallites have been observed in the c-In_2O_3 layer. Therefore, the polymer deposited on the top of the c-In_2O_3 layer exhibits the more "face-on" configuration and better crystallite orientation ordering, leading to the faster charge transport.

3.3 Summary

A solution-processed high mobility indium oxide ETL was synthesized for organic solar cells. After modification with a monolayer of PEIE, the average PCE of device based on this crystallized indium oxide shows a significant enhancement from 9.5% to 10.5% in PTB7-Th–$PC_{71}BM$ solar cells and from 10.8% to 11.5% in PTB7-Th–IEICO-4F solar cells, compared with their counterparts based on zinc oxide. The high mobility of c-In_2O_3 enables a more efficient charge extraction at the interface between the active layer and ETL. Moreover, the aligned crystallite orientation of underlying In_2O_3 also induces the polymer crystallization into a favorable nanomorphology facilitating the charge transport through the active layer. The emergence of the In_2O_3 ETL provides a new material platform for exploring the boundary of high performance OPV. These results not only introduce a new ETL for organic photovoltaic with an excellent device performance but also provide general rules on how to design a highly efficient ETL.

3.4 Experimental method

3.4.1 Chemicals

PTB7-Th (also called PBDTTT-EFT and PCE10) was purchased from 1-Materials. PC71BM and IEICO-4F were purchased from Solarmer. Polyethylenimine ethoxylated (PEIE), 1,8-diiodooctane (DIO) and 1-chloronaphthalene (CN) were supplied by Sigma Aldrich.

3.4.2 Device Preparation

Devices were fabricated with an inverted structure of ITO/ETL/PEIE/active layer/MoO3/Ag. Indium oxide films were prepared from 0.1 M indium oxide precursor by dissolving 300 mg of indium nitrate hydrate (In(NO3)3·xH2O, Sigma, 99.999%) in 10 mL of 2-methoxyethanol (2-ME, Sigma, 99%). Then 200 μL of acetylacetone (Acac, Sigma, 99%) and 70 μL of ammonium hydroxide solution ($NH3 \cdot H_2O$, 28% NH_3 in H_2O) were added as additives, and the solution was stirred overnight. For TFTs, devices were fabricated with a bottom-gate and top-contact (BGTC) structure on highly doped silicon wafers (P++) with 100 nm SiO2. The source/drain Al electrodes (100 nm) were deposited by thermal evaporation via a shadow mask defining a channel region of 1000 μm/150 μm (W/L). For solar cells, the indium oxide film was fabricated by spin-coating the indium oxide precursor solution on ITO glass at 3000 rpm for 30s, followed by pre-baking at 100 °C for 1 min and then baking at desired temperatures for 3 hours. In order to avoid parasitic current during device measurement, the indium oxide layer from each pixel was completely isolated. Zinc oxide films were prepared from 0.1 M zinc oxide precursor. The PEIE interfacial layer was spin-coated on In_2O_3 and ZnO at 5000 RPM from the solution of 2-ME (0.2 wt.%) and then thermally annealed at 100°C for 5 min. The active layer was spin-coated at 1500 RPM for 1min. PTB7-Th and $PC_{71}BM$ were dissolved in a co-solvent (chlorobenzene: 97 vol.% and DIO: 3 vol.%) at a concentration of 8 mg/ml for polymer

PBDTTT-EFT and 12 mg/ml for $PC_{71}BM$. For PTB7-Th:IEICO-4F device, PBDTTT-EFT and IEICO-4F were dissolved in the co-solvent (chlorobenzene: 97 vol.% and CN: 3 vol.%) at a concentration of 10 mg/ml for polymer PBDTTT-EFT and 15 mg/ml for IEICO-4F. After the deposition of active layer, molybdenum oxide and silver were consecutively thermally evaporated with thicknesses of 12 and 100 nm respectively.

3.4.3 Device Characterization

Saturation Mobilities: The saturation mobilities of In_2O_3-based TFTs were evaluated from IDS-VDS curves in the saturation region, based on the followed equation:

$I_{DS,sat} = (C_i \cdot \mu_{sat} \cdot W/2L)(V_{GS}-V_T)^2$ where Ci, W and L, VGS stand for the gate capacitance, channel width and length, and threshold gate voltage, respectively.

Current–Voltage (*I–V*) Measurement: The power conversion efficiency of organic solar cells was measured under 1 sun AM 1.5G using an Oriel 9600 solar simulator by using a Keithley 2400 source meter. The light intensity was calibrated by using KG-5 filter diodes as a reference cell. The device was measured with a 0.1 cm^2 mask.

External Quantum Efficiency (EQE) Measurement: EQE measurements were carried out using an integrated system (Enlitech, Taiwan) with a lock-in amplifier under short-circuit conditions.

Transient Photocurrent Measurements: Transient photocurrent measurements were performed by illuminating the device with or without a white LED. The device was connected to a digital oscilloscope with a 50 Ω termination to achieve a short-circuit condition. A small light perturbation was performed with a laser with 3 ns pulse and the transient response of device was recorded by the oscilloscope.

Ultraviolet-Visible Light Spectroscopy (UV-vis): The ultraviolet-visible light spectroscopy (UV-vis) was performed by using a Hitachi U-4100 spectrophotometer

Scanning Electron Microscope (SEM) Spectroscopy: SEM images were acquired using FEI Nova NanoSEM 230.

X-ray/ Ultraviolet Photoelectron Spectroscopy (XPS/UPS): The electrical properties of In2O3 films were examined by using an X-ray photoelectron spectroscopy (XPS, Omicron) and an ultraviolet photoelectron spectroscopy (UPS, Omicron)

Grazing-Incidence Wide-Angle X-ray Scattering (GIWAXS): GIWAXS experiments were conducted at the Australian Synchrotron on the SAXS/WAXS beamline. All samples were irradiated by 11 KeV X-ray at a fixed angle of 0.16°. 2D scattering signals were probed by using a Dectris Pilatus 1M detector. The X-ray exposure time was 1 s such that no film damage was identified. The results were analyzed by an altered version of the NIKA 2D based in IgorPro

References

1. Li, G.; Zhu, R.; Yang, Y. (2012).Polymer solar cells. *Nat. Photonics 6*, 153– 161
2. Xiao, S.; Zhang, Q.; You, W. (2017). Molecular engineering of conjugated polymers for solar cells: an updated report *Adv. Mater. 29*, 1601391.
3. Huang, W.; Cheng, P.; Yang, Y.; Li, G.; Yang, Y. (2018). High performance organic bulk heterojunction solar cells based on multiple donor or multiple acceptor components *Adv. Mater. 30*, 1705706.
4. An, Q.; Zhang, F.; Zhang, J.; Tang, W.; Deng, Z.; Hu, B. (2016). Versatile ternary organic solar cells: a critical review. *Energy Environ. Sci. 9*, 281– 322.
5. Lu, L.; Zheng, T.; Wu, Q.; Schneider, A. M.; Zhao, D.; Yu, L. (2015). Recent advances in bulk heterojunction polymer solar cells. *Chem. Rev. 115*, 12666– 12731.
6. Yan, C.; Barlow, S.; Wang, Z.; Yan, H.; Jen, A. K. Y.; Marder, S. R.; Zhan, X. (2018). Non-fullerene acceptors for organic solar cells. *Nat. Rev. Mater. 3*,18003.
7. Cheng, P.; Li, G.; Zhan, X.; Yang, Y. (2018). Next-generation organic photovoltaics based on non-fullerene acceptors. *Nat. Photonics 12*, 131– 142.
8. Che, X.; Li, Y.; Qu, Y.; Forrest, S. R. (2018). High fabrication yield organic tandem photovoltaics combining vacuum-and solution-processed subcells with 15% efficiency. *Nat. Energy 3*, 422– 427.
9. Zhang, S.; Qin, Y.; Zhu, J.; Hou, J. (2018). Over 14% Efficiency in Polymer Solar Cells Enabled by a Chlorinated Polymer Donor. *Adv. Mater. 30*, 1800868.
10. Li, S.; Ye, L.; Zhao, W.; Yan, H.; Yang, B.; Liu, D.; Li, W.; Ade, H.; Hou, J. (2018). A wide band gap polymer with a deep highest occupied molecular orbital level enables 14.2% efficiency in polymer solar cells. *J. Am. Chem. Soc. 140*, 7159.
11. Fei, Z.; Eisner, F. D.; Jiao, X.; Azzouzi, M.; Röhr, J. A.; Han, Y.; Shahid, M.; Chesman, A. S. R.;Easton, C. D.; McNeill, C. R.; Anthopoulos, T. D.; Nelson, J.; Heeney, M. (2018). An alkylated indacenodithieno[3,2□b]thiophene□based nonfullerene acceptor with high crystallinity exhibiting single junction solar cell efficiencies greater than 13% with low voltage losses. *Adv. Mater. 30*, 1705209.
12. Sun, C.; Pan, F.; Bin, H.; Zhang, J.; Xue, L.; Qiu, B.; Wei, Z.; Zhang, Z.-G.; Li, Y. (2018). A low cost and high performance polymer donor material for polymer solar cells. *Nat. Commun. 9*,743.
13. Lin, Y.; Zhao, F.; Prasad, S. K. K.; Chen, J. D.; Cai, W.; Zhang, Q.; Chen, K.; Wu, Y.; Ma, W.; Gao, F.;Tang, J. X.; Wang, C.; You, W.; Hodgkiss, J. M.; Zhan, X. (2018). Balanced partnership between donor and acceptor components in nonfullerene organic solar cells with >12% efficiency. *Adv. Mater. 30*, 1706363.

14. Yu, G.; Gao, J.; Hummelen, J. C.; Heeger, A. J. (1995). Polymer photovoltaic cells: enhanced efficiencies via a network of internal donor-acceptor heterojunctions. *Science 270*, 1789– 1791.

15. Li, G.; Chu, C. W.; Shrotriya, V.; Huang, J.; Yang, Y. (2006). Efficient inverted polymer solar cells. *Appl. Phys. Lett. 88*, 253503.

16. Chen, L.-M.; Hong, Z.; Li, G.; Yang, Y. (2009). Recent progress in polymer solar cells: manipulation of polymer:fullerene morphology and the formation of efficient inverted polymer solar cells. *Adv. Mater. 21*, 1434– 1449.

17. Huang, W.; Gann, E.; Cheng, Y.-B.; McNeill, C. R. (2015). In-depth understanding of the morphology–performance relationship in polymer solar cells. *ACS Appl. Mater. Interfaces 7*, 14026– 14034.

18. Yang, G.; Tao, H.; Qin, P.; Ke, W.; Fang, G. (2016). Recent progress in electron transport layers for efficient perovskite solar cells. *J. Mater. Chem. A 4*, 3970– 3990.

19. Sun, Y.; Seo, J. H.; Takacs, C. J.; Seifter, J.; Heeger, A. J. (2011). Inverted polymer solar cells integrated with a low□temperature□annealed sol□gel□derived ZnO film as an electron transport layer. *Adv. Mater. 23*, 1679– 1683.

20. Liang, Z.; Zhang, Q.; Jiang, L.; Cao, G. (2015). ZnO cathode buffer layers for inverted polymer solar cells. *Energy Environ. Sci. 8*, 3442– 3476.

21. Liu, X.; Li, X.; Li, Y.; Song, C.; Zhu, L.; Zhang, W.; Wang, H.-Q.; Fang, J. (2016). High□performance polymer solar cells with PCE of 10.42% via Al□doped ZnO cathode interlayer. *Adv. Mater. 28*, 7405– 7412.

22. Chen, H. -D.; Li, Y. -Q.; Zhu, J.; Zhange, Q.; Zhang, Q.; Xu, R. -P.; Li, C.; Zhang, Y. -X.; Huang, J. -S.;Zhan, X.; You, W.; Tang, J. -X. (2018). Polymer solar cells with 90% external quantum efficiency featuring an ideal light□ and charge□manipulation layer. *Adv. Mater. 30*, 1706083.

23. Park, S. H.; Roy, A.; Beaupré, S.; Cho, S.; Coates, N.; Moon, J. S.; Moses, D.; Leclerc, M.; Lee, K.;Heeger, A. J. (2009). Bulk heterojunction solar cells with internal quantum efficiency approaching 100%. *Nat. Photonics 3*, 297– 303.

24. Qin, M.; Ma, J.; Ke, W.; Qin, P.; Lei, H.; Tao, H.; Zheng, X.; Xiong, L.; Liu, Q.; Chen, Z.; Lu, J.; Yang, G.;Fang, G. (2016). Perovskite solar cells based on low-temperature processed indium oxide electron selective layers. *ACS Appl. Mater. Interfaces 8*, 8460– 8466.

25. Ke, W.; Fang, G.; Liu, Q.; Xiong, L.; Qin, P.; Tao, H.; Wang, J.; Lei, H.; Li, B.; Wan, J.; Yang, G.; Yan, Y. (2015). Low-temperature solution-processed tin oxide as an alternative electron transporting layer for efficient perovskite solar cells. *J. Am. Chem. Soc. 137*, 6730– 6733.

26. Rim, Y. S.; Chen, H.; Liu, Y.; Bae, S.-H.; Kim, H. J.; Yang, Y. (2014). Direct light pattern integration of low-temperature solution-processed all-oxide flexible electronics. *ACS Nano 8*, 9680– 9686.

27. Kim, M.-G.; Kanatzidis, M. G.; Facchetti, A.; Marks, T. J. (2011). Low-temperature fabrication of high-performance metal oxide thin-film electronics via combustion processing. *Nat. Mater. 10*, 382.

28. Rim, Y. S.; Chen, H.; Song, T.-B.; Bae, S.-H.; Yang, Y. (2015). Hexaaqua metal complexes for low-temperature formation of fully metal oxide thin-film transistors. *Chem. Mater. 27*, 5808– 5812.

29. Liao, S.-H.; Jhuo, H.-J.; Cheng, Y.-S.; Chen, S.-A. (2013). Fullerene derivative-doped zinc oxide nanofilm as the cathode of inverted polymer solar cells with low-bandgap polymer (PTB7-Th) for high performance. *Adv. Mater. 25*, 4766– 4771.

30. Chen, J.-D.; Cui, C.; Li, Y.-Q.; Zhou, L.; Ou, Q.-D.; Li, C.; Li, Y.; Tang, J.-X. (2015). Single-junction polymer solar cells exceeding 10% power conversion efficiency. *.Adv. Mater. 27*, 1035–1041.

31. Huang, W.; Gann, E.; Chandrasekaran, N.; Thomsen, L.; Prasad, S. K. K.; Hodgkiss, J. M.; Kabra, D.;Cheng, Y.-B.; McNeill, C. R. (2017). Isolating and quantifying the impact of domain purity on the performance of bulk heterojunction solar cells. *Energy Environ. Sci. 10*, 1843– 1853.

32. Huang, W.; Gann, E.; Xu, Z.-Q.; Thomsen, L.; Cheng, Y.-B.; McNeill, C. R. (2015). A facile approach to alleviate photochemical degradation in high efficiency polymer solar cells. *J. Mater. Chem. A 3*, 16313– 16319.

33. Zhou, Y.; Fuentes-Hernandez, C.; Shim, J.; Meyer, J.; Giordano, A. J.; Li, H.; Winget, P.; Papadopoulos, T.;Cheun, H.; Kim, J.; Fenoll, M.; Dindar, A.; Haske, W.; Najafabadi, E.; Khan, T. M.; Sojoudi, H.; Barlow, S.;Graham, S.; Brédas, J.-L.; Marder, S. R.; Kahn, A.; Kippelen, B. (2012). A Universal method to produce low–work function electrodes for organic electronics. *Science 336*, 327– 332.

34. Yu, X.; Marks, T. J.; Facchetti, A. (2016). Metal oxides for optoelectronic applications. *Nat. Mater. 15*, 383–396

35. Huang, W.; Gann, E.; Thomsen, L.; Dong, C.; Cheng, Y.-B.; McNeill, C. R. (2015). Unraveling the morphology of high efficiency polymer solar cells based on the donor polymer PBDTTT□EFT. *Adv. Energy Mater. 5*,1401259.

36. Verploegen, E.; Mondal, R.; Bettinger, C. J.; Sok, S.; Toney, M. F.; Bao, Z. (2010). Effects of thermal annealing upon the morphology of polymer-fullerene blends. *Adv. Funct. Mater. 20*,3519– 3529, DOI: 10.1002/adfm.201000975

37. Rivnay, J.; Mannsfeld, S. C. B.; Miller, C. E.; Salleo, A.; Toney, M. F. (2012). Quantitative determination of organic semiconductor microstructure from the molecular to device scale. *Chem. Rev. 112*, 5488– 5519.

38. Huang, W.; Gann, E.; Chandrasekaran, N.; Prasad, S. K. K.; Chang, S.-Y.; Thomsen, L.; Kabra, D.;Hodgkiss, J. M.; Cheng, Y.-B.; Yang, Y.; McNeill, C. R. (2017). Influence of fullerene acceptor on the performance, microstructure, and photophysics of low bandgap polymer solar cells. *Adv. Energy Mater. 7*, 1602197.

39. Yoon, S.; Ha, T.-J.; Kang, D.-W. (2017). Improving the performance and reliability of inverted planar perovskite solar cells with a carbon nanotubes/PEDOT:PSS hybrid hole collector. *Nanoscale 9*, 9754, DOI: 10.1039/C7NR02404E

40. Rim, Y. S.; Chen, H.; Kou, X.; Duan, H.-S.; Zhou, H.; Cai, M.; Kim, H. J.; Yang, Y. (2014). Boost up mobility of solution□processed metal oxide thin□film transistors via confining structure on electron pathways. *Adv. Mater. 26*, 4273– 4278.

41. Nomura, K.; Ohta, H.; Takagi, A.; Kamiya, T.; Hirano, M.; Hosono, H. (2004). Room-temperature fabrication of transparent flexible thin-film transistors using amorphous oxide semiconductors. *Nature 432*, 488.

Chapter 4 High-Efficiency Organic Tandem Solar Cells with Effective Transition Metal Chelates Interconnecting Layer

(This chapter is based on the publication, *Solar RRL 2017, 1(10): 1700139*)

Organic tandem solar cells have two sub□cells vertically connected via an interconnecting layer (ICL), which the ICL plays a critical role of determining the performance of the tandem cell. In this manuscript, we report a new design of the ICL consisting of zirconium (IV) acetylacetonate (Zr□Acac) as the electron transport layer. The Zr□Acac has a suitable work function to pin the Fermi□level of the ICL and hence, can effectively behave as the charge recombination function for the tandem device. Comparing to the reference device consisting of ZnO ETL layer, the Zr□Acac ICL can effectively enhance the efficiency by 20%, from 8.4 to 10.1% power conversion efficiencies. More importantly, the Zr□Acac ETL layer functions effectively without thermal annealing, which not only simplifies the tandem solar cell processing, but also widens the front sub□cell material selection.

4.1 Motivation

Learning from the success of inorganic solar cells, multiple junction OPV designs that integrate the contributions from a few sub-cells that have active layers with different light absorption spectral ranges have been adopted. Multiple-junction structure can lead to a substantial reduction of energy losses by incorporating PV units with complementary bandgaps (E_g) in the serial connected tandem structure.

For developing a stable high-efficiency organic tandem solar cells, besides active materials for sub-cells, one of the most important factors is the interconnecting layer (ICL), which is indispensable to separate and transport charge carriers from each sub-cell. High quality ICLs are required to have an intact V_{oc}; a tandem PV without a proper ICL will have diminished V_{oc} value because of the opposite PN direction for the carriers in the two directly connected sub-cells that have the same anode and cathode on the overall structure. The first criterion for an adequate ICL, therefore, is that the active layer/ICL interface must be an Ohmic contact for minimizing the loss of the total V_{oc} of two sub-cells that have misaligned energy levels. Second, in order to minimize optical losses, ICL has to be highly transparent. Kim et al. developed all solution-processed metal oxide (TiOx)/poly(3,4-ethylenedioxylenethiophene)-polystylene sulfonic acid (PEDOT:PSS) composites as interconnecting layer for two sub-cells in series in tandem OPV.[1] Metal/metal oxide composite has also been adopted to have both good stability and transparency in ICL design.[2-4] Traditional metal oxide transport layers, however, require high temperature treatment to increase the number of metal-oxygen bonds in the film so as to obtain good charge carrier mobility.[5] Yet most of the organic photoactive layers experiencing high temperature thermal treatment exhibit severe donor-acceptor phase separation or acceptor recrystallization that lead to stronger charge recombination and smaller

photo current. [6-7] As a result, additional requirements for the preparation of a proper ICL of tandem OPV should be that (i) the ICL is compatible with low temperature treatment or thermal treatment□free processes for maintaining stable active layers and (ii) processing the ICL with orthogonal solvent to the neighbor solution□processed layer is required to prevent the penetration into underlying layer. Because of these multifarious requirements, developing an effective ICL design for tandem OPV is quite challenging. Here, we present an organic□inorganic hybrid material—Zirconium acetylacetonate (Zr□Acac) which can function well as an effective ETL unit in ICL for tandem OPV without undergoing thermal treatment. The resulting ICL can be used for wider selection of sub□cells with different active materials in tandem OPV devices.

In this work, we report a high performance tandem organic solar cell using a wide bandgap polymer poly[benzo[1,2□b:4,5□b́]dithiophene□thiophene□2,1,3□benzooxadiazole] (PBDTTBO) with 1.8 eV optical bandgap, and an effective low bandgap polymer poly[2,7□(5,5□bis□(3,7□dimethyloctyl)□5H□dithieno[3,2□b:2′,3′□d]pyran)□alt□4,7□(5,6□difluoro□2,1,3□benzothia diazole)] (PDTP□DFBT) with 1.3 eV optical bandgap, to build front, and rear sub□cell, respectively. For developing more viable tandem design, we used an effective transition metal chelate Zr□Acac as an n□type interconnecting layer material in our organic tandem PV design. The Zr□Acac layer gives superior electrical and optical properties without any thermal treatment in the single junction OPV.[8] By incorporating Zr□Acac within the tandem solar cell, we enhance the PCE of the tandem solar cell by nearly 20%, as compared to that of the reference tandem device that adopted ZnO electron transport layer. We achieved over 10% power conversion efficiency with better V_{oc} and J_{sc} values.

4.2 Result and discussion

4.2.1 Wide and Low Bandgap Photoactive Materials

Wide bandgap polymer PBDTTBO has good optical absorbance in UV□Visible region and decent short□circuit current when mixed with $PC_{71}BM$. Low bandgap PDTP□DFBT has an optical absorption cutoff in NIR region while still possesses a good open□circuit voltage. PBDTTBO and PDTP□DFBT were synthesized following the steps from the references.[9, 10] Their optical and electronical properties make the two polymers good candidates for achieving high efficiency organic tandem solar cells. To examine them, absorption spectra of polymer films have been shown in **Figure 4-1(a)**. The absorption cutoff of PBDTTBO is around 700 nm while PDTP□DFBT polymer exceeds 900 nm. From the absorption spectra, it can be found that the low bandgap PDTP□DFBT displays a strong absorption in infrared region while the wide bandgap PBDTTBO mainly catch photons before 650 nm. The absorptions for PBDTTBO and PDTP□DFBT are complementary to each other, and thus are promising to make good current matching of two sub□cells.

We then obtained photovoltaic performances of two single junction devices based on polymer PBDTTBO and PDTP□DFBT, respectively. The single junction devices architecture is shown in **Figure 4-2(a)**. Inverted structure was used here to obtain highly stable and better vertical phase distribution of the photoactive layer.[11,12] In this inverted structure, ZnO and MoO_3 served as electron and hole transport layers, respectively.[13-19] **Figure 4-2(b)** and **c** show current density—voltage (*J–V*) curves of the PBDTTBO and PDTP□DFBT single junction solar cell with varying active layer thicknesses from 80 to 130 nm under 1000 W/m^2 AM1.5G illumination. V_{oc}, J_{sc}, FF, and and their PCE are listed in **Table 4-1**. The best performance of

PBDTTBO device has been obtained at active layer thickness of 100 nm with a PCE of 7.0% along with V_{oc} of 0.86 V, J_{sc} of 13.2 mA cm^{-2} and FF of 61.7 %.

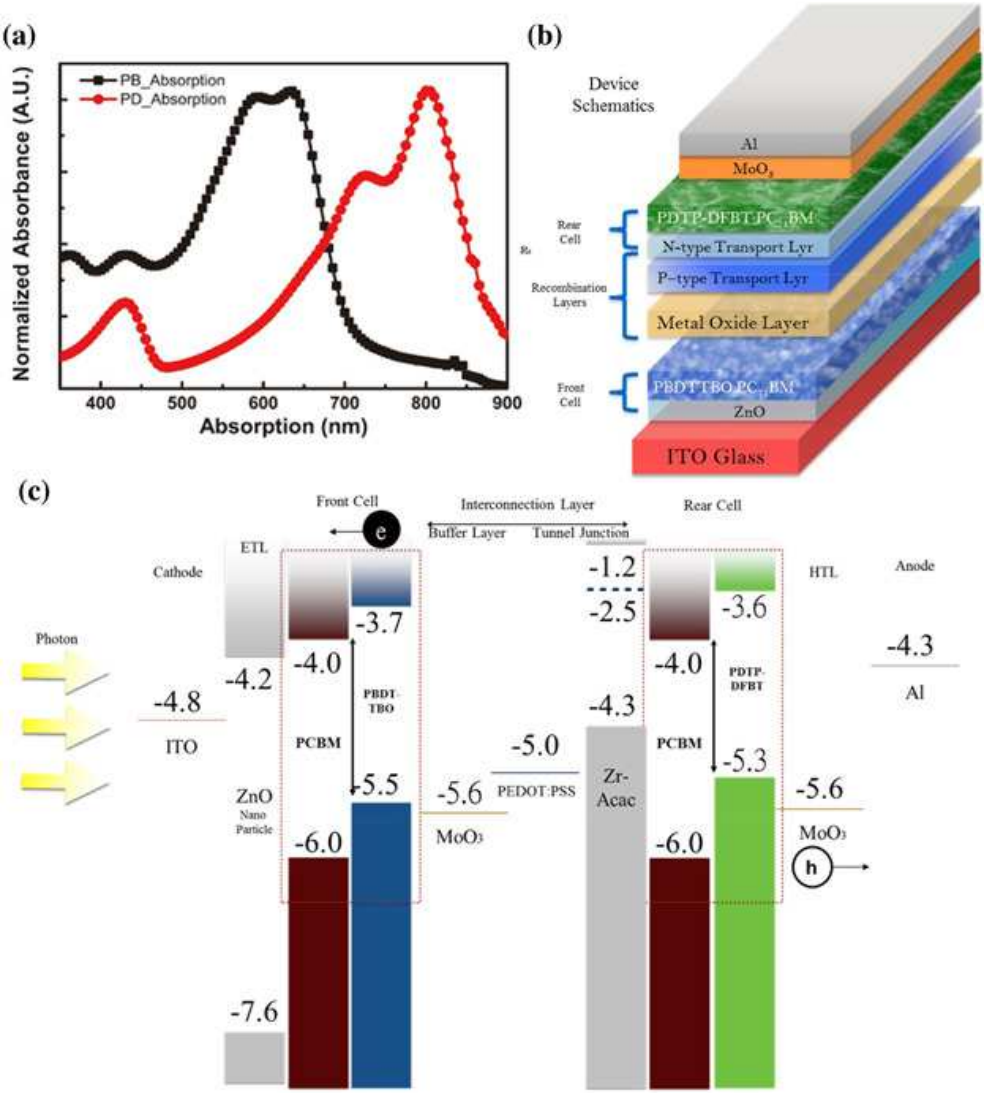

Figure 4-1 (a) Normalized UV□vis absorption spectra of PBDTTBO and PDTP□DFBT thin films. **(b)** Schematic of device structure. **(c)** Band diagram of PBDTTBO and PDTP□DFBT tandem solar cells.

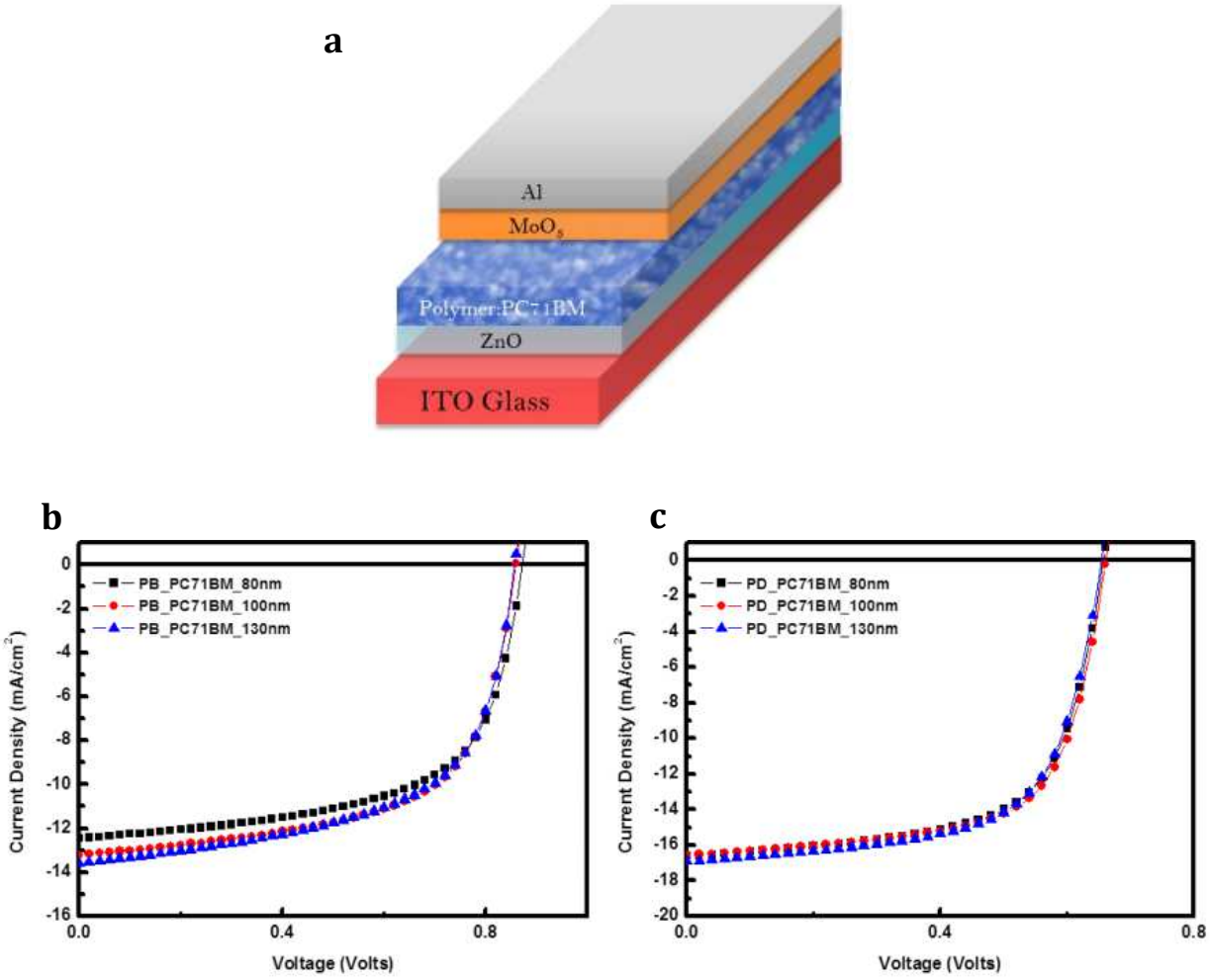

Figure 4-2 (a) The structure of inverted single junction device. **(b) (c)** The J-V curves of PBDTTBO:$PC_{71}BM$ and PDTP-DFBT:$PC_{71}BM$ devices with different active layer thickness

The tandem device architecture and energy diagram are shown in **Figure 4-1(b)** and (**c**). The structure comprises ITO/ZnO/PBDTTBO:$PC_{71}BM$/ICL/PDTP□DFBT:$PC_{71}BM$/MoO_3/Al. The broader ICL has three layers that include MoO_3 buffer layer, hole, and electron transport layer. For hole transporting in tandem structure, MoO_3 and modified PEDOT:PSS (M□PEDOT) were utilized and confirmed as an useful interconnecting layer for inverted tandem solar cells.[14, 18] We measured that the work function of MoO_3 and M□PEDOT are −5.6 and −5.0 eV, respectively.[20-21] The work function of MoO_3 is comparable to that of the HOMO (highest

occupied molecular orbital) level for PBDTTBO polymer (−5.3 eV), indicating a possible Ohmic contact at the polymer/MoO_3 interface, being beneficial for charge collection. MoO_3 also provides a better physical contact and robust protection between the WBG layer and followed M□PEDOT layer. High free charge concentration M□PEDOT can serve as a recombination center between MoO_3 and electron transport layer. Although ZnO has been used as a common electron transport layer for inverted single junction polymer solar cells,[17,18] the free charge concentration, however, is not high enough, resulting in a non□ideal contact resistance.[21] In addition, ZnO needs relatively high temperature (120 °C) thermal treatment to obtain fair electron mobility. When it serves as an ICL in tandem solar cell, such a high temperature treatment resulted in the post□crystallization of fullerene in the front cell and degrades the front cell performances.

Device Process	*V*oc (volts)	*J*sc (mA/ cm^2)	FF	PCE (Max)
PBDTTBO:$PC_{71}BM$ 80nm	0.87±0.02	13.1±0.2	61.7±0.5	6.6 (6.7)
PBDTTBO:$PC_{71}BM$ 100 nm	0.86±0.01	13.2±0.1	61.7±0.2	7.0 (7.2)
PBDTTBO:$PC_{71}BM$ 130 nm	0.86±0.01	13.4±0.3	59.7±0.4	6.9 (7.0)
PDTP-DFBT:$PC_{71}BM$ 80nm	0.66±0.01	16.0±0.3	66.0±0.8	7.0 (7.1)
PDTP-DFBT:$PC_{71}BM$ 100 nm	0.66±0.01	16.1±0.4	65.8±0.5	7.0 (7.2)
PDTP-DFBT:$PC_{71}BM$ 130 nm	0.66±0.02	16.7±0.4	63.6±0.6	7.0 (7.1)

Table 4-3 The average device data of PBDTTBO:$PC_{71}BM$ and PDTP-DFBT:$PC_{71}BM$ devices with different active layer thickness.

4.2.2 Physical Properties of Transport Materials

To improve the electron transporting through ICL, we developed a more versatile N□ type material, zirconium(IV) acetylacetonate (Zr□Acac) combined in ICL. Its chemical structure is shown in **Figure 4-3(a)**. When incorporating the Zr□Acac with superior optical, topological, and electronic properties into the interfacial layers between sub□cells, the enhanced performance of the tandem cells is expected, because the work function of Zr□Acac is very low (2.5 eV, as shown in **Figure 4-3(c)**) and lies above the LUMO levels of the commonly used acceptors. The LUMO level of the organic□semiconductors will thus be pinned to the Fermi level of the buffer layer, inducing a "barrier free" electron extraction from the LUMOs of the acceptors, which is beneficial for ICL.[22-24] Moreover, the annealing□free process of Zr□Acac prevents the possible damage to the underlying layers during fabrication.

Transmission spectra of ZnO and Zr-Acac thin films were measured and demonstrated that the transmittance of Zr-Acac layer is better than that of ZnO layer at functional thickness as shown in **Figure 4-3(b)**. The surface feature of ZnO layer under 120 °C temperature treatment for 3 min and as-cast Zr-Acac layer were inspected via using atomic force microscope (AFM) and scanning electron microscope (SEM) as shown in **Figure 4-4**. From AFM data, the roughness value R_{ms} of Zr-Acac thin film is 2.6 nm, which is smaller than 3.2 nm of ZnO thin film. In both AFM and SEM images, it is clear that Zr-Acac thin film has more continuous flake shape features with preferential orientation parallel to the substrate surface. Compared to the sufficiently annealed ZnO layer, there are smaller aggregations of ZnO nano particle under low temperature treatment.[5] In order to examine the morphology of PDTP-DFBT/$PC_{71}BM$ on the

different transport layer, grazing incident wide angle X-ray scattering (GIWAXS) was also performed (**Figure 4-5)**. The scattering peak located at q = 0.33 Å along the out-of-plane direction (OOP) is corresponding to the alkyl stacking. From 1D scattering line profile (**Figure 4-5(c))**, it is clear that polymer PDTP-DFBT on different transport layers shows same scattering peak position and a similar peak width, indicating that there is no significant difference in crystallization behavior of polymer PDTP-DFBT between transport layer ZnO and Zr-Acac.

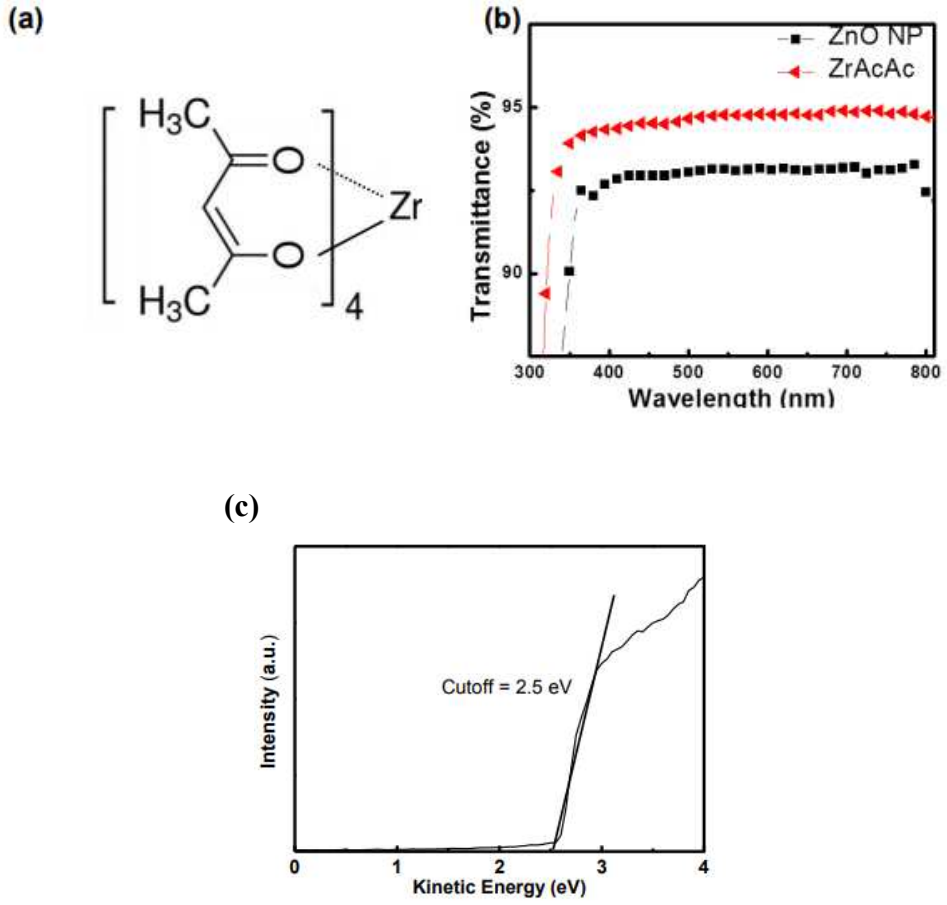

Figure 4-3 (a) The chemical structure of Zr-Acac and **(b)** transmittance comparison of Zr-Acac and ZnO thin film. **(c)** Ultraviolet photoelectron spectroscopy (UPS) of Zr-Acac thin film on ITO glass substrate.

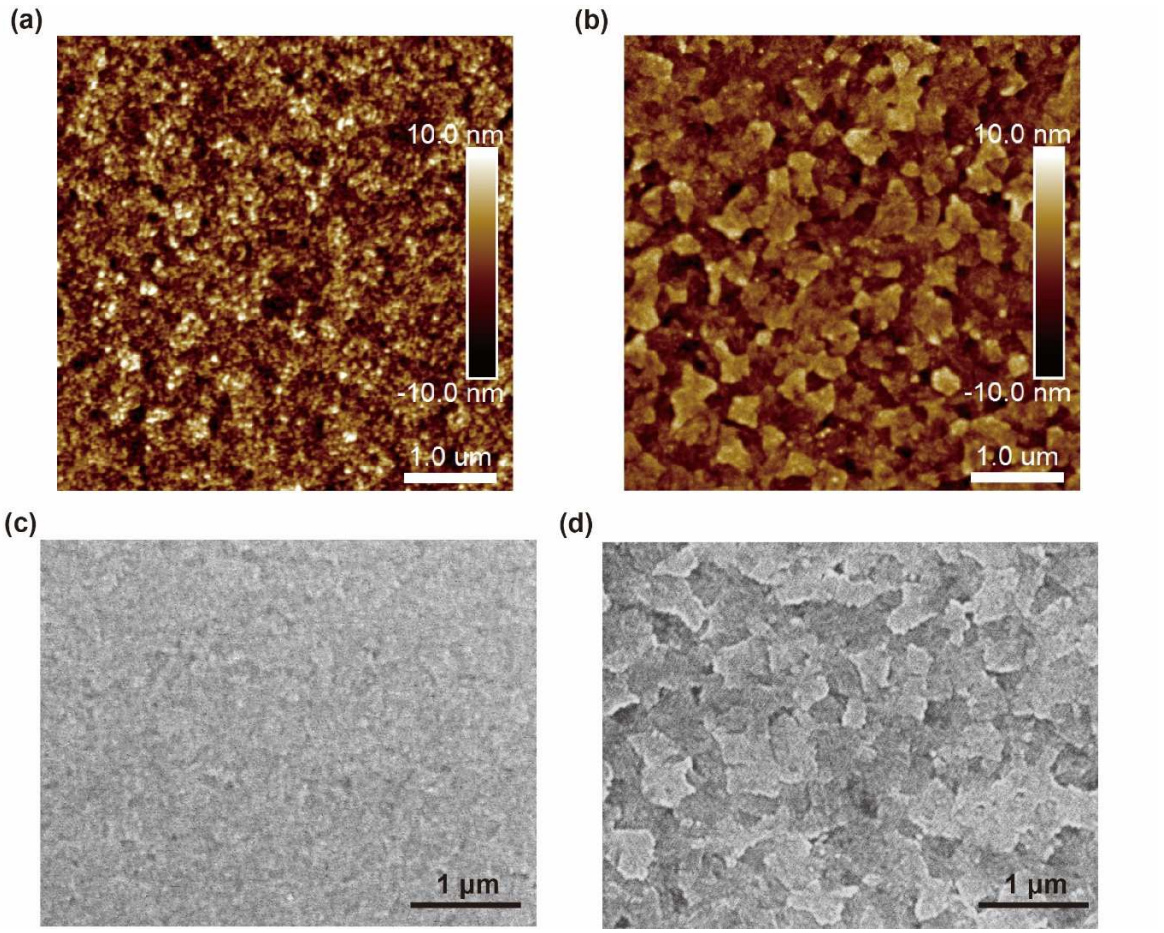

Figure 4-4 AFM and SEM images of thin films of (**a** and **c**) ZnO nano particle and (**b** and **d**) Zr□Acac.

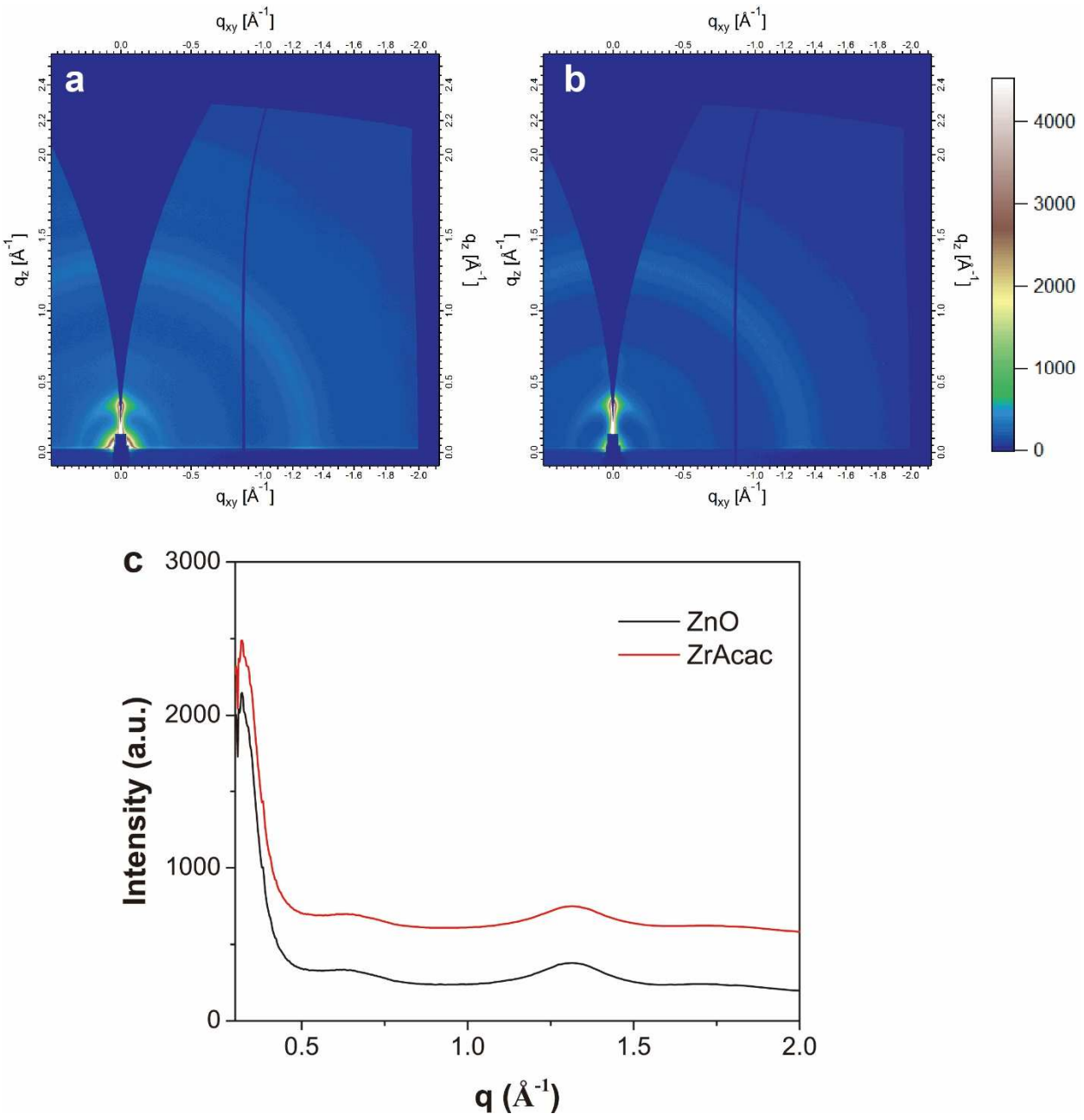

Figure 4-5 Grazing incident wide angle X-ray scattering patterns of PDTP-DFBT/$PC_{71}BM$ on substrate of **(a)** ZnO and **(b)** Zr-Acac. **(c)** 1D profile cut from 2D scattering pattern along the out-of-plane (OOP) direction.

4.2.3 Light Field Simulation for Optimized Tandem Devices

In order to harvest more photons and balance the photocurrent, a key factor for achieving high efficiency organic tandem solar cell is that the front and real sub□cells should have comparable short circuit current dictating the most suitable structure.[25] To optimize the thickness in both front and real cell, the light field simulation was carried out for predicting the proper combination of our tandem design and shown in **Figure 4-6**. In the simulation, the front and real cells were set at a range that varies from 80 to 130 nm. Typically, the overall photocurrent through the tandem cells is limited by the front PBDTTBO cell; the front cell is, thus, prepared with a thicker active layer for matching the current of the rear cell. As a result, the optimized thickness of each cell will be different, as compared to that of the single junction cells. When prepared the front and rear cell in thickness of 80 and 130 nm, the integrated current of front cell is around 8 mA/cm^2 while the rear one is 17 mA/cm^2. If using 100 nm as front and rear cell thickness the values are 9 and 15 mA/cm^2 for each sub□cell. In comparison, the result of simulated light intensity showed that the incident light of the 130:80 nm ratio is more utilized before 600 nm region despite the decreased utilization of NIR region photons. The integrated currents of tandem device with 130:80 nm of rear cell are 11 and 12 mA/cm^2, respectively. This thickness distribution leads in a better current matching to prevent electrical loss.

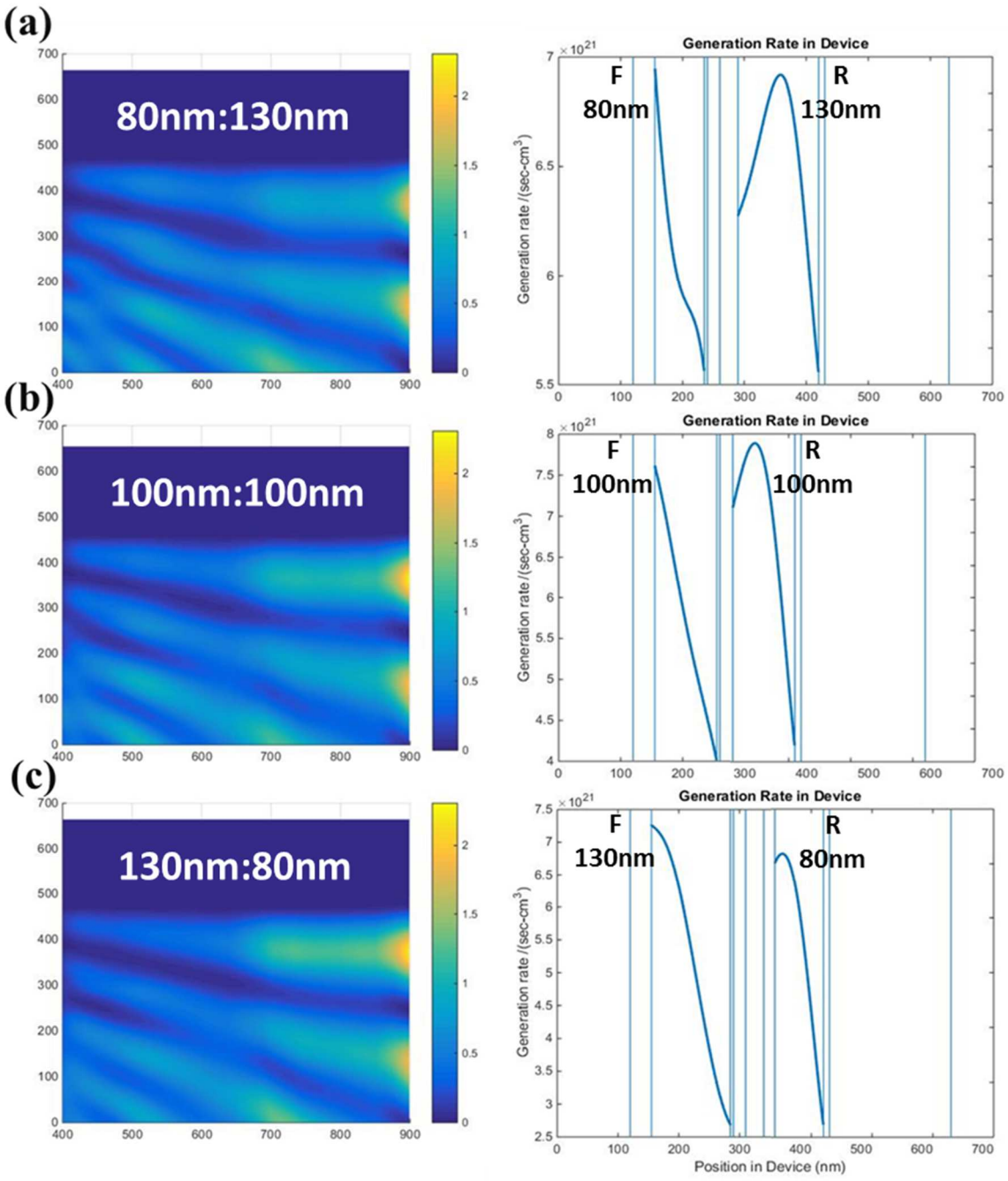

Figure 4-6 The light field simulation (Left) Light field distribution and (Right) generation current of active layer for **(a)** 80 and 130 nm **(b)** 100 and 100 nm **(c)** 130 and 80 nm

4.2.4 Solar Cells Performance

The experimental results of tandem devices of different thickness distribution are shown in **Figure 4-7(a)** and **Table 2**. It is apparent that the short circuit value of the tandem devices increases with the increased front: rear sub□cell thickness ratio, which is agreed with the simulation results. 130:80 nm ratio tandem devices with Zr□Acac transport layer showed V_{oc} of 1.49 V, J_{sc} of 11.6 mA cm^{-2}, FF of 58.7, and PCE of 10.1%.

Based on the optimized thickness of simulation results, tandem devices with Zr□Acac and ZnO transport layer have been done and the *J–V* curves and EQE of the tandem cells for comparison are shown in **Figure 4-8(a)** and **(b)**. The details of devices performance of the tandem devices with different electron transport layers are summarized in **Table 3**. The tandem cell with Zr□Acac shows V_{oc} of 1.49 V, which is only 0.04 V less than the sum of the two single junctions. The small difference might be attributed to the resistance of ICL and the V_{oc} drop from the rear cell due to weaker light intensity compared to 1 sun intensity. In the case of ZnO one, V_{oc}, and J_{sc} of tandem cells is smaller − 1.46 and 10.4 mA/cm^2. It might be caused from higher energy barrier for electron transporting to recombination site. FF is 55.1, which was also lower than the Zr□Acac case because of stronger surface recombination from worse surface contact in the organic/metal oxide junction. Combining all of these, the 10.1% PCE of the tandem with Zr□Acac ETL is 20% better than the 8.4% of ZnO one.

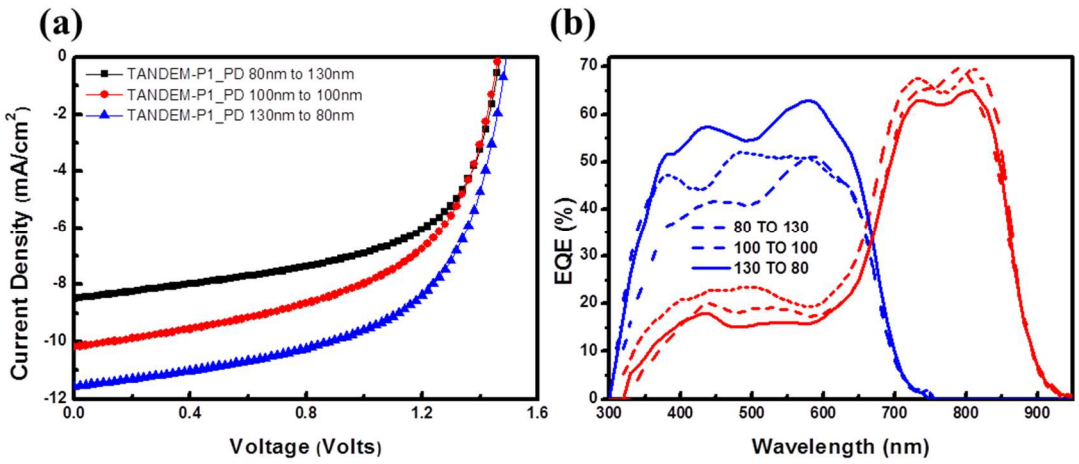

Figure 4-7 (a) *J–V* curves and **(b)** EQEs of PBDTTBO and PDTP□DFBT tandem solar cells with different front and rear sub□cell thickness.

Device Data	*V*oc (volts)	*J*sc (mA/cm^2)	FF	PCE (Max)
Tandem-Zr-Acac 80 nm/130 nm	1.46±0.02	8.2±0.3	58.1±0.5	7.0 (7.3)
Tandem-Zr-Acac 100 nm/100 nm	1.47±0.01	9.6±0.6	56.3±1.3	7.9 (8.2)
Tandem-Zr-Acac 130 nm/80 nm	1.48±0.01	11.5±0.1	57.6±1.1	9.8 (10.1)

Table 4-2 The average device performance parameters of tandem solar cells based on Zr-Acac interconnecting layer with different front and rear sub-cell thickness.

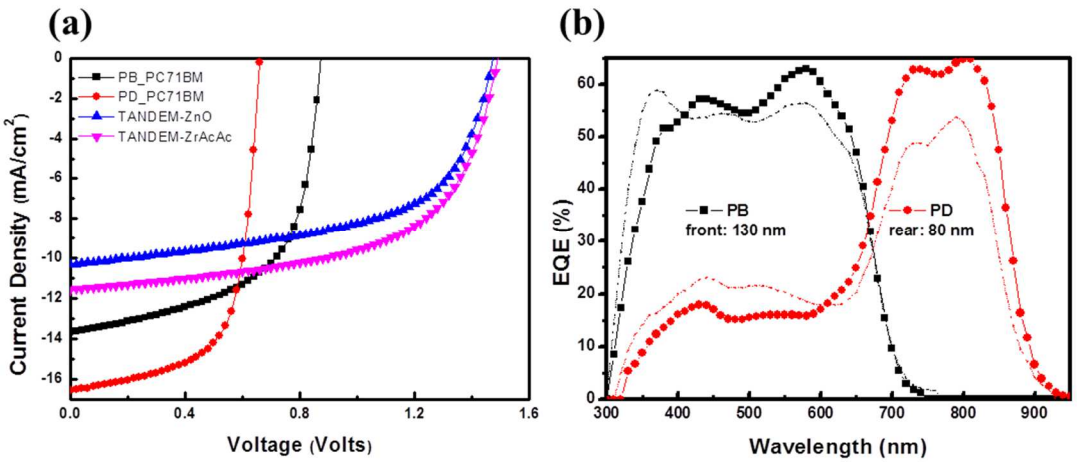

Figure 4-8 (a) *J-V* curves and **(b)** EQEs of PBDTTBO and PDTP-DFBT single junction and tandem solar cells with ZnO (dashed line) and Zr-Acac (solid line) as interconnecting layer.

Device Data	*V*oc (volts)	*J*sc (mA/ cm^2)	FF	PCE (Max)
PBDTTBO:PC$_{71}$BM	0.86±0.01	13.2±0.1	61.7±0.2	7.0 (7.2)
PDTP-DFBT:PC$_{71}$BM	0.66±0.01	16.1±0.4	65.8±0.5	7.0 (7.2)
Tandem-ZnO 130 nm/80 nm	1.47±0.02	10.4±0.2	55.3±0.7	8.4 (8.4)
Tandem-Zr-Acac 130 nm/80 nm	1.48±0.01	11.5±0.1	57.6±1.1	9.8 (10.1)

Table 4-3 The average device performance parameters of single junction OPV based on ZnO and tandem solar cells.

4.3 Summary

We have presented double-junction tandem solar cells with an effective wide bandgap polymer PBDTTBO and low bandgap PDTP-DFBT that complement one another in their absorption spectra and EQE for beneficial to achieve good current matching. By using an effective Zr-Acac electron transport layer in the interconnecting layer, better electron transport property has been achieved over that of the commonly used ZnO layer. The power conversion efficiency of the tandem cell incorporating a Zr-Acac layer has been greatly increased to 10.1%, compared to 8.4% for those ZnO-based, exhibiting a nearly 20% efficiency enhancement. These results indicate that tandem solar cells utilizing Zr-Acac as ETL in interconnecting layer can effectively increase the device efficiency. Furthermore, the annealing-free property of the Zn-Acac ETL is expected to largely broaden the active materials selection in solution-processed tandem polymer solar cells, and eventually, will leads to higher efficiencies when new materials are available.

4.4 Experimental method

4.4.1 Chemicals

The photoactive materials PBDTTBO and PDTP-DFBT were synthesized following the steps from the references.[9,10] $PC_{71}BM$ (CAS: 609771-63-3) was purchased from Solarmer Energy Inc. ZnO nanoparticle solution was synthesized in our lab following the steps from the reference.[17] Zirconium(IV) acetylacetonate powder (97%) was purchased from Sigmal Adrich. The details of modified PEDOT:PSS can be found in the other reference.[26] Molybdenum(VI) oxide (99.5%) and Aluminum shots (99.99%) were purchased from Alfa Aesar.

4.4.2 Device Preparation

The pre-cleaned patterned ITO substrates were first treated with UV-ozone for 15 min. ZnO nanoparticles were spin-coated on the ITO substrates at a spin rate of 2500 RPM 30 sec and the substrate was annealed at 150 ° C for 15 min. The typical thickness of ZnO layer is about 40 nm. The concentration of ZnO nano particle solution is about 10 mg/ml for our experiments. Then, the active layer was spin coated on the ZnO surface. The photoactive materials PBDTTBO:$PC_{71}BM$ (1:2) solutions were dissolved in dichlorobenzene with or without 3% 1-chloronaphthalene at a concentration from 8.0 mg/mL. PDTP-DFBT:$PC_{71}BM$ (1:2) solutions were dissolved in dichlorobenzene at a concentration of 7.5 mg/mL. Before spin-coating the active layer, PBDTTBO:$PC_{71}BM$ and PDTP-DFBT:$PC_{71}BM$ solutions were respectively heated at 80 and 60 °C for more than 2 hours to improve the qualities of the blend solutions. For preparing the PBDTTBO:$PC_{71}BM$ front cell, the spin rate is from 1200 RPM 60 sec to 2000 PRM 60sec to achieve 80 nm to 130 nm film thickness. For preparing the PDTP-DFBT:$PC_{71}BM$ rear cell, the spin rate is from 1800 RPM 60 sec to 2500 RPM

60sec to achieve 80 nm to 130 nm film thickness. After spin-coating the active layer, the samples were transferred into the evaporation chamber for fabricating the MoO_3 /Al electrode at a base pressure below $5 * 10^{-6}$ Torr. The device area is 0.1 cm^2.

For tandem devices, the front cells were made according to the single junction procedure, and then the samples were transferred into the evaporation chamber for MoO_3 buffer layer deposition, the thickness of MoO_3 are 10 to 15 nm. Then M-PEDOT:PSS were spin-casted onto MoO_3 surface and annealed at 120 °C for 30sec to 5min. For electron tunnel junction, a thin layer of ZnO film or Zr-Acac film was spin-casted. ZnO film was thermal annealed at 120 °C for 30 sec after spin-coating. ZnO nanoparticles were prepared by the same way described in single junction device fabrication. Zr-Acac was dissolved in anhydrous alcohol solution in a weight ratio of 0.2 to 0.5 %. The Zr-Acac solution was spin-coated at the speed varying from 3000 RPM to 5000 RPM for 40 sec. The typical thickness of the Zr-Acac layers prepared in our tandem solar cells is about 30 – 40 nm. Then the rear cell was fabricated as the front cells; the thicknesses of the active layer were controlled by the spin coating speed. Finally, the samples were transferred into the evaporation chamber for MoO_3 /Al electrode at a base pressure below $5 * 10^{-6}$ Torr. The device area is 0.1 cm^2.

4.4.3 Device Characterization

Thickness: The film thickness was measured by using Veeco Dektak 150.

Atomic Force Microscope (AFM) Spectroscopy: AFM images were taken by using Bruker Dimension FastScan Scanning Probe Microscope (SPM).

Current–Voltage (*I–V*) Measurement: The power conversion efficiency of organic solar cells was measured under 1 sun AM 1.5G using an Oriel 9600 solar simulator by using a Keithley 2400 source meter. The light intensity was calibrated by using KG-5 filter diodes as a reference cell. The device was measured with a 0.1 cm^2 mask. Light biases of 550 and 800 nm were selected to excite the front, rear sub-cells in the tandem devices. The unexcited sub-cell was then measured using a Xe lamp passing through a monochromator with a typical intensity of 10 μW. The optical parameters n and k of each layer in the device were obtained through spectroscopic ellipsometry.

External Quantum Efficiency (EQE) Measurement: EQE measurements were carried out using an integrated system (Enlitech, Taiwan) with a lock-in amplifier under short-circuit conditions.

Ultraviolet-Visible Light Spectroscopy (UV-vis): The ultraviolet-visible light spectroscopy (UV-vis) was performed by using a Hitachi U-4100 spectrophotometer

Scanning Electron Microscope (SEM) Spectroscopy: SEM images were acquired using FEI Nova NanoSEM 230.

Ultraviolet Photoelectron Spectroscopy (UPS): UPS spectra were obtained by using Kratos X-ray photoelectron spectroscopy.

Grazing-Incidence Wide-Angle X-ray Scattering (GIWAXS): GIWAXS measurement was performed at Advanced Light Source on the 7.3.3. beamline.[55] The results were analyzed by an altered version of the NIKA 2D based in IgorPro

References

1. Kim, J. Y.; Lee, K., Coates. N. E., Moses, D.; Nguyen, T. Q.; Dante, M.; Heeger, A. J. (2007). Efficient tandem polymer solar cells fabricated by all-solution processing. *Science 317*, 222-225.

2. Chou, C. H.; Kwan, W. L.; Hong, Z.; Chen, L. M..; Yang, Y. (2011). A metal□oxide interconnection layer for polymer tandem solar cells with an inverted architecture. *Adv. Mater*. *23*(10), 1282-1286.

3. Bag, S.;Patel, R.J.;Bunha, A.;Grand, C.;Berrigan, J.D.;Dalton, M.J.;Leever, B.J.;Reynolds, J.R.;Durstock, M.F. (2015). Tandem solar cells from accessible low band-gap polymers using an efficient interconnecting layer. *ACS Appl. Mater. Interfaces*. *8*, 16-19.

4. Wang, F.;Tan, Z.a.;Li, Y. (2015). Solution-processable metal oxides/chelates as electrode buffer layers for efficient and stable polymer solar cells. *Energy Environ. Sci*. *8*, 1059-1091..

5. Sun, Y.;Seo, J.H.;Takacs, C.J.;Seifter, J.;Heeger, A.J. (2011). Inverted polymer solar cells integrated with a low□temperature□annealed sol□gel□derived ZnO film as an electron transport layer. *Adv Mater*. *23*, 1679-1683.

6. Cheng, P.;Zhan, X. (2016). Stability of organic solar cells: challenges and strategies. *Chem Soc Rev*, *45*, 2544-2582.

7. Huang, W.;Gann, E.;Cheng, Y.-B.;McNeill, C.R. (2015). In-depth understanding of the morphology–performance relationship in polymer solar cells. *ACS Appl Mater Interfaces 7*, 14026-14034.

8. Tan, Z.a.;Li, S.;Wang, F.;Qian, D.;Lin, J.;Hou, J.;Li, Y. (2014). High performance polymer solar cells with as-prepared zirconium acetylacetonate film as cathode buffer layer. *Sci Rep 4*, 4691.

9. Jiang, J.-M.;Lin, H.-K.;Lin, Y.-C.;Chen, H.-C.;Lan, S.-C.;Chang, C.-K.;Wei, K.-H. (2013). Side chain structure affects the photovoltaic performance of two-dimensional conjugated polymers. *Macromolecules 47*, 70-78.

10. Dou, L.;Chen, C.-C.;Yoshimura, K.;Ohya, K.;Chang, W.-H.;Gao, J.;Liu, Y.;Richard, E.;Yang, Y. (2013). Synthesis of 5 H-dithieno [3, 2-b: 2′, 3′-d] pyran as an electron-rich building block for donor–acceptor type low-bandgap polymers. *Macromolecules 46*, 3384-3390.

11. He, Z.;Zhong, C.;Su, S.;Xu, M.;Wu, H.;Cao, Y. (2012). Enhanced power-conversion efficiency in polymer solar cells using an inverted device structure. *Nat Photon*ics *6*, 591-595.

12. Li, G.;Chu, C.-W.;Shrotriya, V.;Huang, J.;Yang, Y. (2006). Efficient inverted polymer solar cells. *Appl Phys Lett 88*, 253503.

13. Yip, H.-L.;Jen, A.K.Y. (2012). Recent advances in solution-processed interfacial materials for efficient and stable polymer solar cells. *Energy Environ Sci 5*, 5994-6011.

14. White, M.S.;Olson, D.C.;Shaheen, S.E.;Kopidakis, N.;Ginley, D.S. (2006). Inverted bulk-heterojunction organic photovoltaic device using a solution-derived ZnO underlayer. *Appl Phys Lett 89*, 143517.

15. Waldauf, C.;Morana, M.;Denk, P.;Schilinsky, P.;Coakley, K.;Choulis, S.A.;Brabec, C.J. (2006). Highly efficient inverted organic photovoltaics using solution based titanium oxide as electron selective contact. *Appl Phys Lett 89*, 233517.

16. Hau, S.K.;Yip, H.-L.;Baek, N.S.;Zou, J.;O'Malley, K.;Jen, A.K.-Y. (2008). Air-stable inverted flexible polymer solar cells using zinc oxide nanoparticles as an electron selective layer. *Appl Phys Lett 92*, 253301.

17. You, J.;Chen, C.-C.;Dou, L.;Murase, S.;Duan, H.-S.;Hawks, S.A.;Xu, T.;Son, H.J.;Yu, L.;Li, G. Y, Yang. (2012). Metal oxide nanoparticles as an electron□transport layer in high□performance and stable inverted polymer solar cells. *Adv Mater 24*, 5267-5272.

18. Small, C.E.;Chen, S.;Subbiah, J.;Amb, C.M.;Tsang, S.-W.;Lai, T.-H.;Reynolds, J.R.;So, F. (2012). High-efficiency inverted dithienogermole–thienopyrrolodione-based polymer solar cells. *Nat Photon. 6*, 115-120.

19. Yang, T.;Cai, W.;Qin, D.;Wang, E.;Lan, L.;Gong, X.;Peng, J.;Cao, Y. (2010). Solution-processed zinc oxide thin film as a buffer layer for polymer solar cells with an inverted device structure. *J. Phys. Chem. C 114*, 6849.

20. Yang, J.;Zhu, R.;Hong, Z.;He, Y.;Kumar, A.;Li, Y.;Yang, Y. (2011). A robust inter□connecting layer for achieving high performance tandem polymer solar cells. *Adv. Mater 23*, 3465-3470.

21. Dou, L.;You, J.;Yang, J.;Chen, C.-C.;He, Y.;Murase, S.;Moriarty, T.;Emery, K.;Li, G.;Yang, Y. (2012). Tandem polymer solar cells featuring a spectrally matched low-bandgap polymer.*Nat Photon*. *6*, 180-185.

22. Braun, S.;Salaneck, W.R.;Fahlman, M. (2009). Energy□level alignment at organic/metal and organic/organic interfaces. *Adv Mater*. *21*, 1450-1472.

23. Chai, L.;White, R.T.;Greiner, M.T.;Lu, Z.H. (2014). Experimental demonstration of the universal energy level alignment rule at oxide/organic semiconductor interfaces. *Phys Rev B 89*, 035202,

24. Li, Y.;Li, P.;Lu, Z.-H. (2017). Mapping Energy Levels for Organic Heterojunctions. *Adv. Mater. 29*, 1700414-n/a,10.1002/adma.201700414.

25. Gilot, J.;Wienk, M.M.;Janssen, R.A.J. (2010). Optimizing polymer tandem solar cells. *Adv. Mater*. *22*, E67-E71.

26. Cheng, P.;Yan, C.;Wu, Y.;Wang, J.;Qin, M.;An, Q.;Cao, J.;Huo, L.;Zhang, F.;Ding, L. Sun, Y. (2016). Alloy acceptor: superior alternative to PCBM toward efficient and stable organic solar cells. *Adv. Mater*. *28*, 8021-8028.

Chapter 5 High Performance Organic Tandem Solar Cells Based on Ternary Sub-Cells

(This chapter is based on the manuscript submitted to *Nano Lett.*)

Current-matching among different sub-cells of tandem solar cells remains as the main challenge for organic tandem photovoltaics. In this section, we provide a facile approach to achieve a good current matching via engineering the chemical composition of non-fullerene ternary blend sub-cells. For the front sub-cell, a ternary blend of PDBT-T1:TPH-Se:ITIC was selected due to its good thermal stability. The amorphous nature of TPH-Se can sufficiently suppress the unfavorable phase separation of blends during the heat treatment, enabling the long-term sintering in the fabrication of high quality interconnecting layer. A double-junction tandem device was fabricated with a rear sub-cell consisting of PBDBT: ITIC. After the design of the chemical composition of the front sub-cell, power conversion efficiency (PCE) of double-junction tandem device increased from 10.6% using PDBT-T1:TPHSe binary front sub-cell to 11.5% using PDBT-T1:TPH-Se:ITIC ternary front sub-cell due to better current matching. In order to further enhance the light absorption in the near-infrared region, a third junction PBDTTT-EFT:IEICO-4F was introduced. The champion cell of triple-junction non-fullerene tandem solar cell achieves a PCE of 13.0% with a high open circuit voltage of 2.52 V.

5.1 Motivation

To overcome the deficiency of absorption spectrum in organic solar cells, two approaches are widely used: ternary solar cells and tandem solar cells. In ternary solar cells, the use of multi-donor materials or multi-acceptor materials with complementary absorption spectra can enhance light absorption of the active layer.[1-6] However, the efficiency of organic ternary solar cells is still limited by Shockley-Queisser theory. Organic tandem photovoltaics, on the other hand, can break the S-Q efficiency limit for a single-junction solar cell by reducing thermalization losses from hot carriers, which have higher photon energy than the bandgap (Eg).[7-8] Tandem solar cells realize the superstition of open circuit voltage of sub-cells while preserving the high short circuit current by utilizing the photoactive materials with compensatory absorption achieving a more complete coverage of the solar spectrum.[9-16]

Two major bottlenecks for increasing the efficiency of organic tandem solar cells even further are fabrication of high quality ICL and optimization of unbalanced short circuit current between each sub-cell. As described in Chap.4, organic tandem solar cells consist of two or more sub-cells connected in series through a thin ICL. The ICL should form an Ohmic contact between two sub-cells for the efficient charge recombination and should also be robust enough to protect the underlying films from solvents during the deposition of upper layers.[17] In order to fabricate a high quality ICL, heat-treatment is typically required. However, most of high efficiency fullerene-based solar cells show rapid degradation under heat treatment due to coarsening of fullerene aggregates.[18] For solving these problems, one approach is to use thermal treatment-free materials like transition metal chelates as ICL, which are addressed in the last chapter. The other approach is to use non-fullerene material in the active layer for a better thermal durability of phase transition. Based on this idea, PDBT-T1:TPH-Se blend (molecular

structures shown in **Figure 5-1(a)**) with excellent thermal stability was selected in the front sub-cell. The acceptor TPH-Se exhibits an extremely twisted three-bladed propeller configuration, which significantly suppresses the phase separation in PDBT-T1:TPH-Se blends upon heating.[19] Therefore, the use of this blend is able to maintain device performance of front sub-cell when a long-term sintering is applied during the fabrication of ICLs. A high efficiency non-fullerene organic tandem solar cell was thus achieved with good current matching property as absorption spectra of ternary blend can be easily tuned by varying its chemical composition.

5.2 Result and discussion

5.2.1 Active Layer Materials for Tandem Solar Cell

As shown in **Figure 5-1(b)**, both PDBT-T1 and TPH-Se exhibit absorption spectra below 680 nm. In the rear sub-cell, the active layer consists of PBDB-T:ITIC, whose absorption spectrum extends to 800 nm. Tandem devices were fabricated with an architecture of ITO/ZnO/active layer 1/MoO3/m-PEDOT:PSS/np-ZnO/active layer 2/MoO3/Ag, as seen in **Figure 5-1(c)**. As a result, an efficiency of 10.6% was achieved for tandem solar cells using a binary front sub-cell PDBT-T1:TPH-Se. After the absorption spectra of front sub-cell was optimized by introducing an additional non-fullerene acceptor ITIC, the best efficiency of tandem device increases to 11.5%. The substitution of 10 wt.% TPH-Se by ITIC does not change front sub-cells' original morphology but enhances its light absorption and facilitates charge separation via cascade energy level, leading to a more balanced current between front and rear sub-cells. A wide bandgap polymer is usually used as the front sub-cell in a tandem device, which allows for the longer wavelength light to pass through. Among the various wide bandgap polymers, PDBT-T1 is a promising candidate with proper absorption coverage and high efficiency.[20] **Figure 5-2(a)** compares photovoltaic performance of OPV based on polymer

PDBT-T1 blended with two different acceptors $PC_{71}BM$ and TPH-Se. All devices are fabricated with the same architecture of ITO/ZnO/active layer/MoO3/Ag. Device photovoltaic parameters are summarized in **Table 5-1**. Devices based on the PDBT-T1:$PC_{71}BM$ blend exhibit an average PCE of 7.2%, J_{sc} of 12.4 mA/cm^2, V_{oc} of 0.85 V and FF of 0.68. As the fullerene acceptor PCBM is replaced by a non-fullerene acceptor TPH-Se with a better energy level alignment with PDBT-T1 polymer, the V_{oc} increases from 0.85 V in PDBT-T1:$PC_{71}BM$ to 1.00 V in PDBT-T1:TPH-Se. An average PCE of 8.0% is achieved in PDBT-T1:TPH-Se non-fullerene solar cells. Device based on non-fullerene acceptor TPH-Se shows the increased efficiency mainly due to the enhanced V_{oc}.

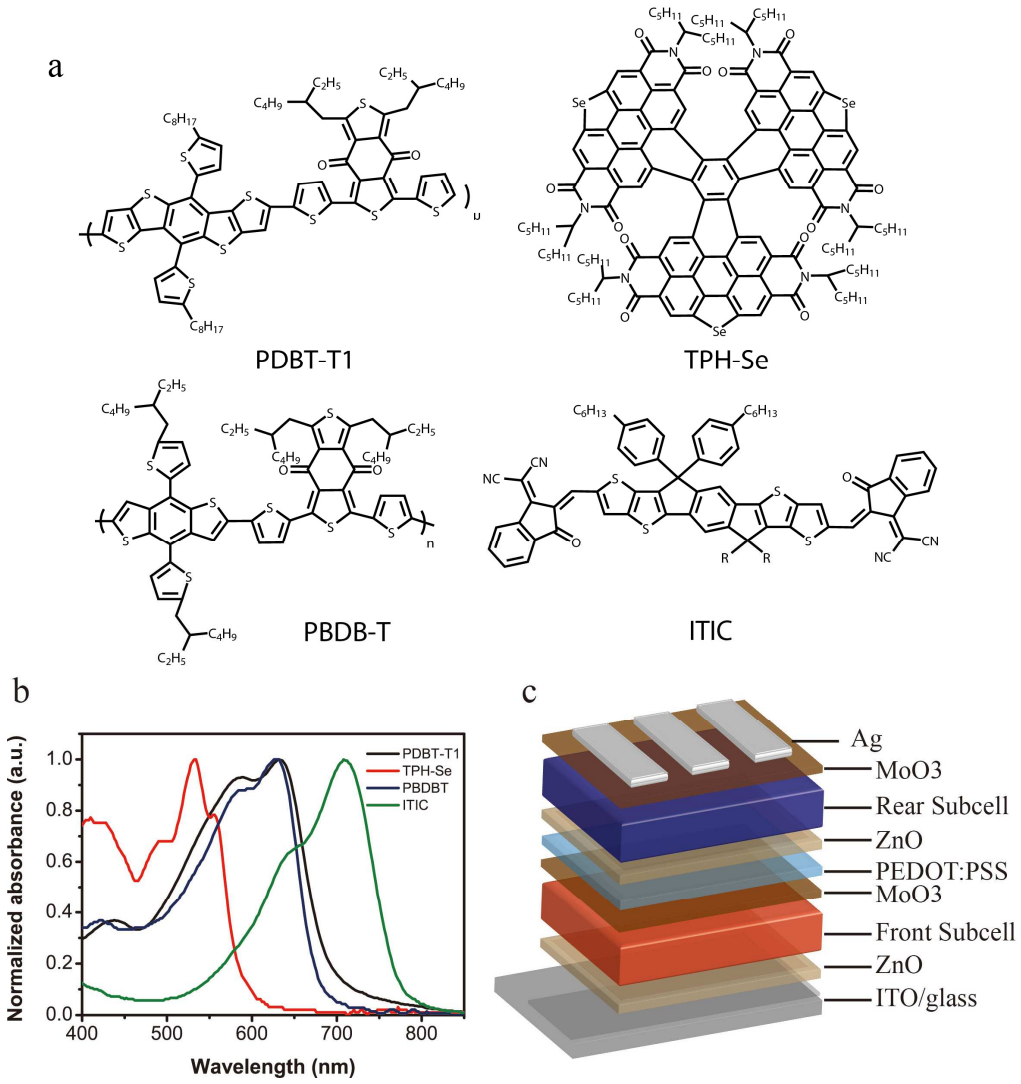

Figure 5-1 (a) Chemical structures of PDBT-T1, TPH-Se, PBDBT and ITIC. **(b)** UV-vis spectra of PDBT-T1, TPH-Se, PBDBT and ITIC films. **(c)** Schematic of the organic tandem solar cells.

Since heat treatment is usually employed during fabrication of high quality ICLs, a good thermal stability is required for the front sub-cell.[18] **Figure 5-2(b)** compares the evolution of device performance based on two different acceptors upon annealing at 120 °C. (This temperature is used for sintering ICLs.) Fullerene-based devices show a poor stability. They exhibit a rapid decrease in PCE, dropping to 75% of its initial PCE after only 5 min heat treatment. After heating at 120 °C for 60 mins, the PCE continuously decays to 58% of its initial

PCE. By contrast, there is no significant change in PCE of the non-fullerene device after 5 min heat treatment. Furthermore, PCE of non-fullerene-based device after heating at 120°C for 60 min still preserves 88% of its initial value.

Active layer	Efficiency (%)	V_{OC} (V)	J_{SC} (mA/cm^2)	Fill factor
PDBT-T1: $PC_{71}BM$	7.2	0.85	12.4	0.68
PDBT-T1:TPH-Se	8.0	1.00	11.9	0.67

Table 5-1 Photovoltaic parameters of organic solar cells based on the PDBT-T1 wide bandgap polymer.

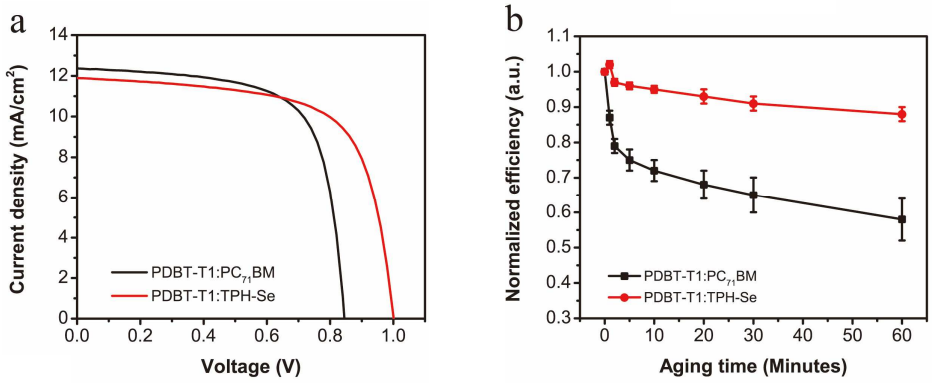

Figure 5-2 (a) Device performance of PDBT-T1 based fullerene and non-fullerene organic solar cells. **(b)** Evolution of normalized efficiency of PDBT-T1 based fullerene and non-fullerene organic solar cells. The devices were thermally aged at 120 °C.

5.2.2 Morphological Analysis of Fullerene and Non-Fullerene Acceptors

The morphological evolution of both fullerene and non-fullerene blend under heat treatment is investigated by using GIWAXS, as shown in **Figure 5-3(a-d)**. In scattering patterns of PDBT-T1:$PC_{71}BM$ blend before and after heat treatment (**Figure 5-3(a)** and **(b)**), a broad peak located along the out-of-plane direction at q= 1.7 Å^{-1} corresponds to polymer π-π stacking and an intensive peak at q= 0.3 Å^{-1} corresponds to polymer alkyl stacking. The isotropic rings at

q= 1.4 $Å^{-1}$ are related to the fullerene aggregation. It is noted that scattering intensities from both, polymer and fullerene, significantly increase after heat treatment, suggesting the rapid growth of both polymer and fullerene crystallites. An unfavorable phase separation occurs, leading to a rapid degradation of the device performance. In PDBT-T1:TPH-Se blend, due to the amorphous nature of non-fullerene acceptor TPH-Se, the crystallization of polymer PDBT-T1 is remarkably disrupted, with a relative lower polymer crystallinity. Non-fullerene acceptor TPH-Se does not exhibit any scattering patterns, indicating that most of the non-fullerene acceptor molecules dispersed in the mixed phase. Non-fullerene blends exhibit a similar microstructure before and after heat treatment with a slight increase in their scattering intensities, shown in **Figure 5-3(c)** and **(d)**. This highly mixed phase in PDBT-T1:TPH-Se blend is able to effectively suppress phase separation and maintain its initial morphology during heat treatment.[18] Therefore, the TPH-Se based non-fullerene blend presents better thermal stability than its fullerene-based counterpart. Considering the absolute efficiency and thermal stability, PDBT-T1:TPH-Se device is the better candidate for the front sub-cell.

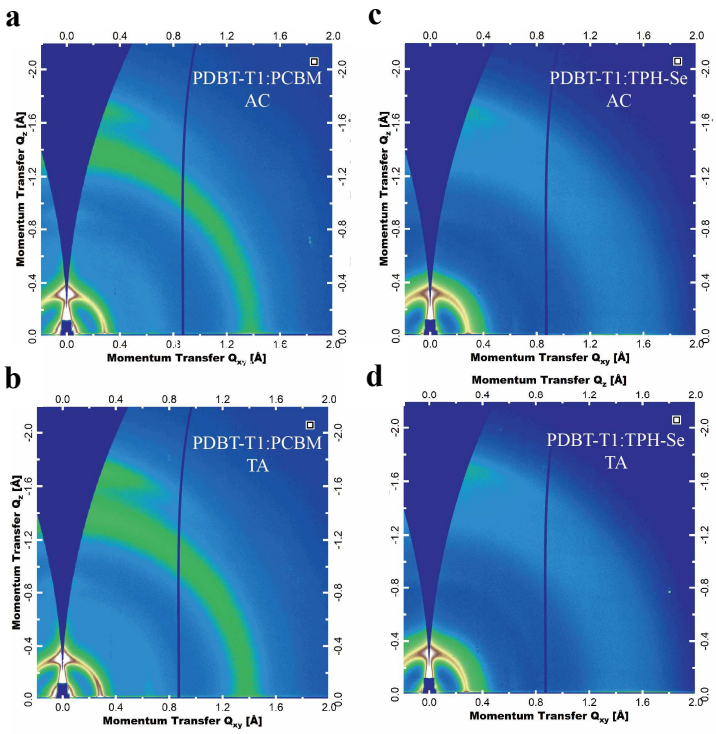

Figure 5-3 2D GIWAXS patterns of **(a)** as-cast PDBT-T1:$PC_{71}BM$, **(b)** thermal-annealed PDBT-T1:$PC_{71}BM$, **(c)** as-cast PDBT-T1:TPH-Se and **(d)** thermal-annealed PDBT-T1:TPH-Se. The blends are thermally annealed at 120 °C for 3 mins.

5.2.3 Current Matching Design of The Front Cell

The engineering of the active layer thickness is a widely used method for optimizing the current matching between different sub-cells. However, in some solar cells such as PDBT-T1:TPH-Se-based device, PCE is very sensitive to the thickness of the active layer. The slight increase in the thickness of the active layer may lead to a rapid degradation of the device performance, especially in FF. Herein, a non-fullerene component ITIC, which is the third component in the active layer blend, was introduced into the PDBT-T1:TPH-Se blend to tune the optical field distribution in a tandem device. **Figure 5-4** presents device performance of double junction organic tandem solar cells, using non-fullerene PDBT-T1:TPH-Se:ITIC ternary front sub-cell and PBDB-T:ITIC rear sub-cell. In the front sub-cell, PDBT-T1:TPH-Se:ITIC blends

were deposited with a fixed PDBT-T1 concentration and varied ratios of ITIC. Active layers with different ITIC contents were deposited with a thickness of around 80 nm to achieve their optimized device performance. **Figure 5-4(a)** and (**b)** demonstrate the trend of average PCEs and J_{sc} values in double-junction tandem solar cells as a function of ITIC content in the front sub-cell. An average PCE of 10.3% is achieved in the tandem device using PDBT-T1:TPH-Se binary front sub-cell, with an average J_{sc} of 8.8 mA/cm^2. As 10 wt.% additional component ITIC is introduced into the front sub-cell to replace TPH-Se, the average PCE and photocurrent density of tandem device monotonically increases from 10.3 to 11% and 8.8 to 9.3 mA/cm^2 respectively. **Figure 5-4(c)** and **(d)** compare J-V harvesting characteristics and EQE spectra of the champion tandem device with 0 wt. % and 10 wt. % ITIC in the front sub-cell. The details of photovoltaic parameters are summarized in **Table 5-2**. The tandem device based on the PDBT-T1:TPH-Se binary sub-cell shows the best efficiency of 10.6%, with J_{sc} of 9.2 mA/cm^2, V_{oc} of 1.84 V and FF of 0.63. Substitution of 10 wt.% TPH-Se by ITIC in the front sub-cell leads to an improvement in its efficiency, yielding the best value of 11.5% with an increased J_{sc} of 9.6 mA/cm^2 and improved FF of 0.65. As shown in EQE spectra, the increased J_{sc} of tandem device is attributed to the more balanced short circuit current between the front and rear sub-cells. In the tandem device based on the binary front sub-cell, the J_{sc} integrated from the front sub-cell is slightly lower than that from the rear sub-cell. The substitution of 10 wt.% TPH-Se by ITIC is able to enhance the light absorption of the front sub-cell in the region between 700 and 750 nm, resulting in a perfect current matching. As the ITIC content continues to increase from 10 wt.% to 50 wt.%, decreases in average PCE (from 11 to 8.6%) and J_{sc} (from 9.3 to 7.8 mA/cm^2) are observed. As more ITIC molecules are introduced, the absorption overlap between the front sub-cell and rear sub-cell becomes large, hindering the sufficient light absorption from the rear sub-

cell. The photocurrent generated from the front sub-cell is significantly higher than the one from the rear sub-cell, resulting in an unbalanced current matching again. As a result, both, PCE and short circuit current of tandem device, experience a rapid decrease upon using a ternary front sub-cell with high fraction of ITIC.

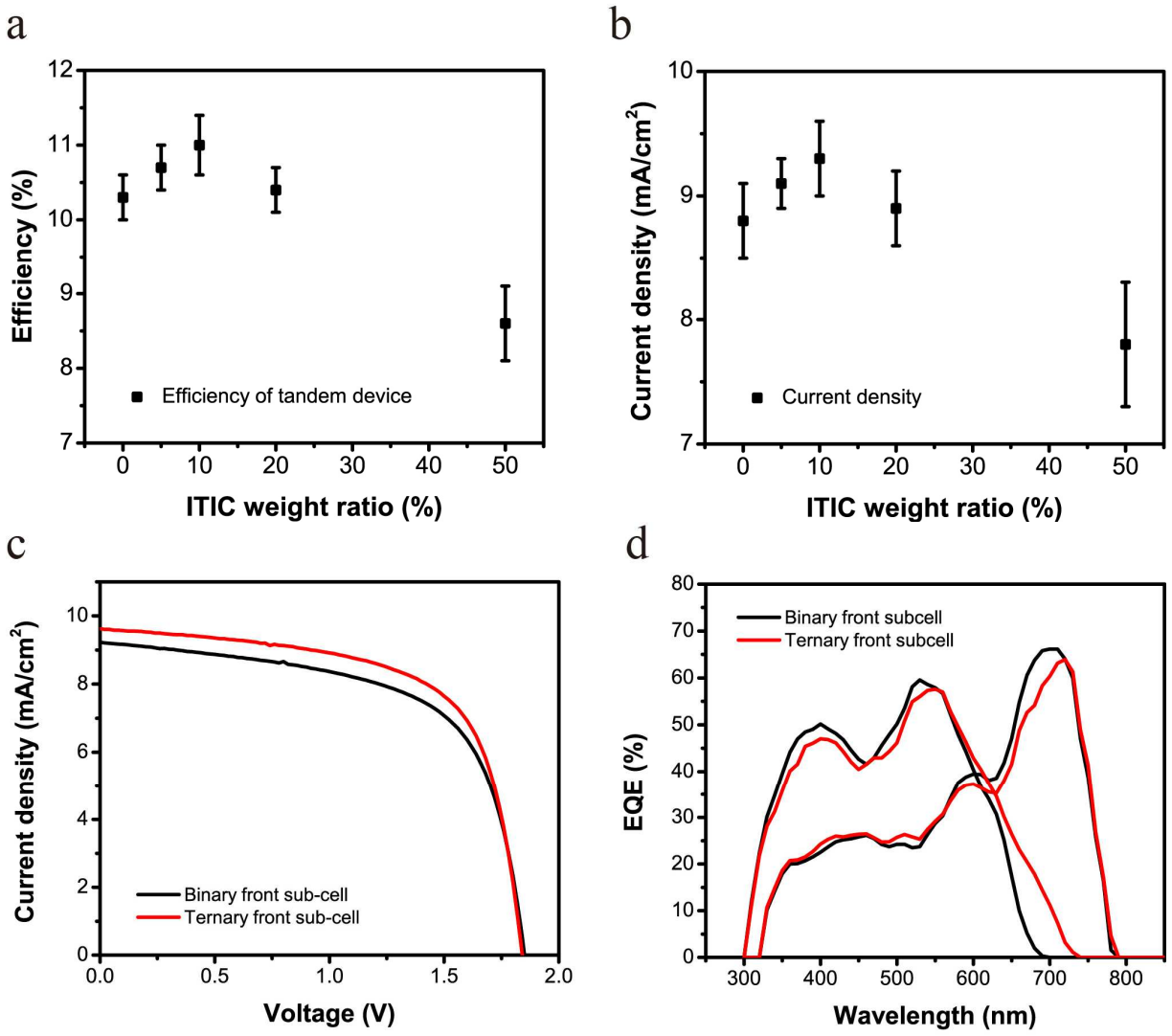

Figure 5-4 Device performance of tandem solar cells based on PDBT-T1/TPH-Se/ITIC ternary front sub-cells. **(a)** Average device efficiency of tandem solar cells as a function of ITIC ratio (in total acceptor) in the front sub-cell. **(b)** Short circuit current of tandem solar cells as a function of ITIC ratio in the front sub-cell. **(c)** Current density-Voltage (J-V) curve in the best tandem devices. **(d)** External quantum efficiency of the best tandem devices.

Front sub-cell	Efficiency (%)	V_{OC} (V)	J_{SC} (mA/cm^2)	Fill factor
Binary	10.6	1.84	9.2	0.63
Ternary	11.5	1.84	9.6	0.65

Table 5-2 Device performance of the champion double junction organic tandem solar cells based on different front sub-cells.

5.2.4 Morphological Analysis of Third Component in Active Layer

In order to better understand the roles of the third component ITIC on fabrication of the high performance non-fullerene tandem devices, device performance and ternary blend morphology in single-junction devices are also systematically investigated, as shown in **Figure 5-5**. **Figure 5-5(a)** shows the average PCE and J_{sc} as a function of ITIC content in acceptor. When a small amount of ITIC (< 20wt.%) is introduced into PDBT-T1:TPH-Se blend, both PCE and J_{sc} of ternary blend shows a rapid improvement. As shown in EQE spectra (**Figure 5-5(b)**), the reason for the increased short circuit current is due to the increased light absorption. The non-fullerene acceptor ITIC exhibits a high absorption in the region between 600 and 750 nm. The light response of PDBT-T1:TPH-Se:ITIC ternary solar cell in the region between 680 and 750 nm shows a linear increase with the increase of ITIC content.

As the best tandem device is achieved by using a ternary PDBT-T1:TPH-Se:ITIC (1:0.9:0.1) non-fullerene sub-cell, **Figure 5-6(a)** compares the J-V curves of PDBT-T1:TPH-Se binary solar cells and PDBT-T1:TPH-Se:ITIC (1:0.9:0.1) ternary solar cells. The device based on PDBT-T1:TPH-Se binary blend shows an average efficiency of 8.0% with J_{sc} of 11.9 mA/cm^2, V_{oc} of 1.0 V and FF of 0.67, while the device fabricated based on PDBT-T1:TPH-Se:ITIC (1:0.9:0.1) exhibits better performance, yielding an average PCE of 8.4% with an enhanced J_{sc} of 12.4 mA/cm^2 and an enhanced FF of 0.68. In addition to increased J_{sc}, the incorporation of a

third component ITIC forming a cascade structure in the ternary blend which facilitates efficient charge transfer leads to an enhanced FF.[21-22] It is also worth noting that the ternary blend device shows a much better thermal stability than the binary blend device (see **Figure 5-6(b)**). Compared with the binary sub-cell, the ternary sub-cell takes advantage of the increased light absorption, improved charge separation and enhanced thermal stability.

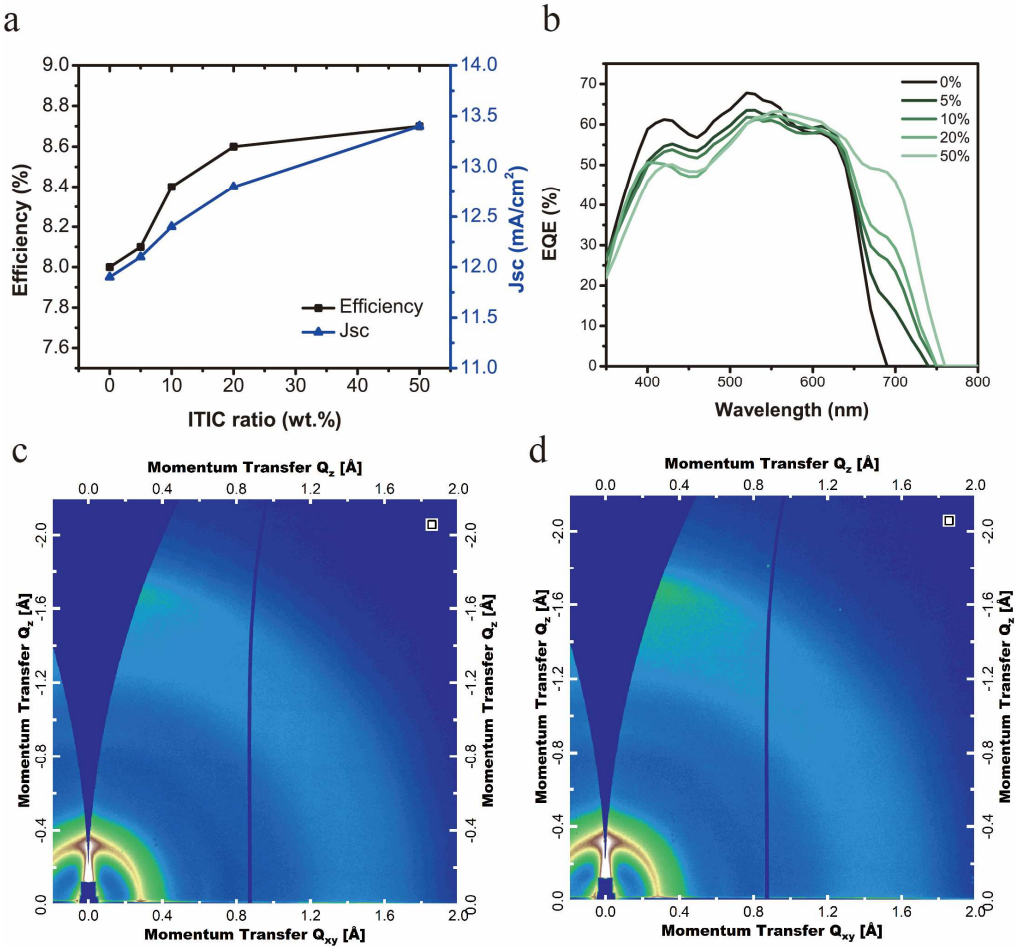

Figure 5-5 (a) Average device efficiency of single junction PDBT-T1/TPH-Se/ITIC ternary solar cells as a function of ITIC ratio. **(b)** External quantum efficiency spectra single junction PDBT-T1/TPH-Se/ITIC ternary solar cells as a function of ITIC ratio. 2D GIWAXS patterns of PDBT-T1/TPH-Se binary blend and PDBT-T1/TPH-Se/ITIC (1:0.9:0.1) ternary blend.

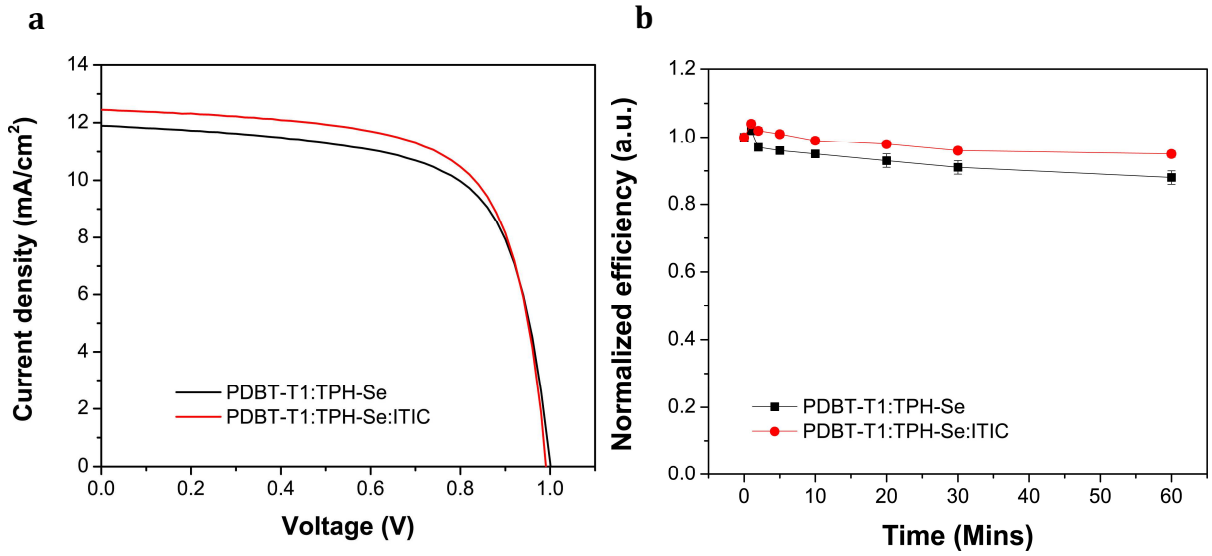

Figure 5-6 (a) Photovoltaic characteristics of PDBT-T1:TPH-Se binary solar cells and PDBT-T1:TPH-Se:ITIC (1:0.9:0.1) ternary solar cells. **(b)** Thermal stability of PDBT-T1:TPH-Se binary solar cells and PDBT-T1:TPH-Se:ITIC (1:0.9:0.1) ternary solar cells. The devices are thermally aged at 120°C.

The morphology of PDBT-T1:TPH-Se:ITIC ternary blend with different ITIC contents is investigated using GIWAXS. **Figure 5-7(a)** and **(b)** show scattering patterns of PDBT-T1:TPH-Se binary blend and PDBT-T1:TPH-Se:ITIC (1:0.9:0.1) ternary blend, respectively. After adding a small amount of a third component ITIC, the polymer PDBT-T1 still maintains its original morphology with similar crystallite orientation and crystallinity. At such low ITIC fraction (10 wt.%), no new scattering peak is obvious, suggesting that there is no separated ITIC crystalline phase. Most of the ITIC molecules are dispersed into the mixed phase. However, as the fraction of ITIC increases to 50 wt.%, several obvious scattering peaks from ITIC are observed and the crystallinity of the PDBT-T1 polymer decreases. Although the J_{sc} of the ternary device still linearly increases with increasing ITIC content from 10 wt.% to 50 wt.%, the PCE approaches a saturated value. In the ternary blend with a large fraction of ITIC (50 wt.%), the originally

optimized morphology becomes disrupted, leading to a rapid decrease in the FF. In order to achieve a better performance of the front sub-cells and an optimized current matching in the tandem device simultaneously, the replacement of the binary blend PDBT-T1:TPH-Se with the ternary blend PDBT-T1:TPH-Se:ITIC (1:0.9:0.1) is an ideal approach for the high performance organic tandem solar cells.

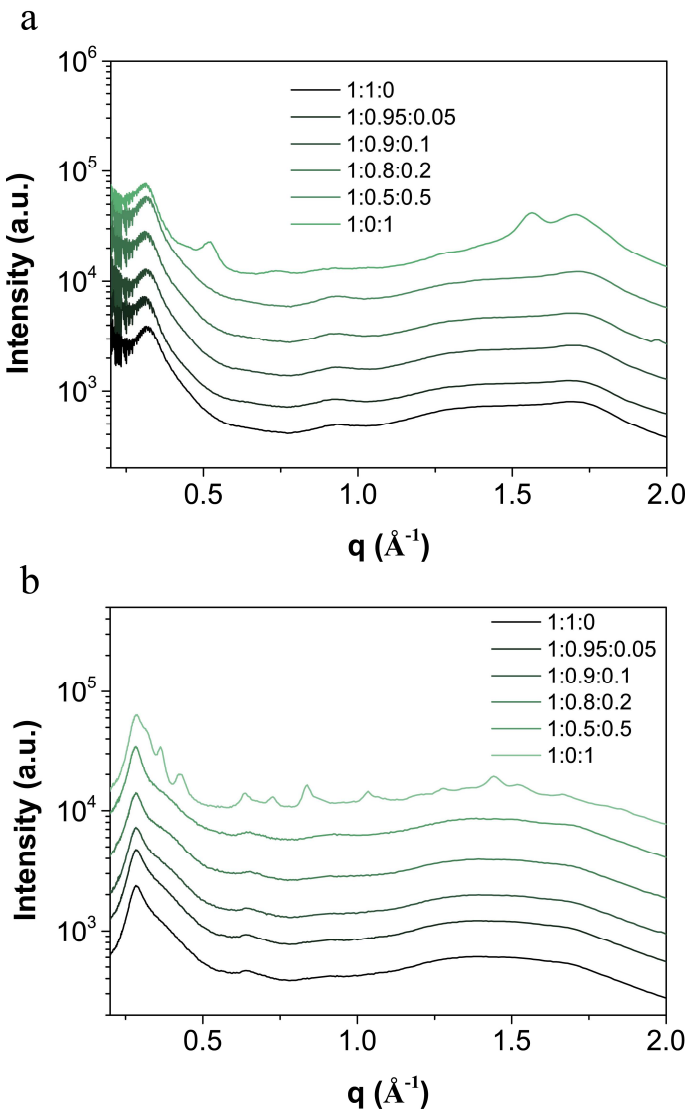

Figure 5-7 1D GIWAXS line profile of PDBT-T1:TPH-Se:ITIC with different ratios: **(a)** out-of-plane and **(b)** in-plane.

The tandem device that uses PDBT-T1:TPH-Se:ITIC as the front sub-cell and PBDB-T:ITIC as the rear sub-cell still suffers from sub-cells' limited optical absorption in the near-infrared (NIR) region. In order to enhance device's light absorption in the NIR region, a triple-junction solar cell is fabricated with a third junction of PBDTTT-EFT:IEICO-4F (molecular structure shown in **Figure 5-8(a)** and UV-vis absorption spectrum shown in **Figure 5-8(b)**). The PBDTTT-EFT:IEICO-4F blend shows a complementary absorption spectrum, starting at 1000 nm with two main absorption peaks located at 900 and 710 nm. After slight increase of the active layer thickness (~100 nm) in the middle sub-cell and fabrication of a 70 nm PBDTTT-EFT:IEICO-4F film as the third junction, a PCE of 13% is achieved in the champion cell, with J_{sc} of 8.0 mA/cm^2, V_{oc} of 2.52 V and FF of 0.63, as shown in **Figure 5-8(c)**.

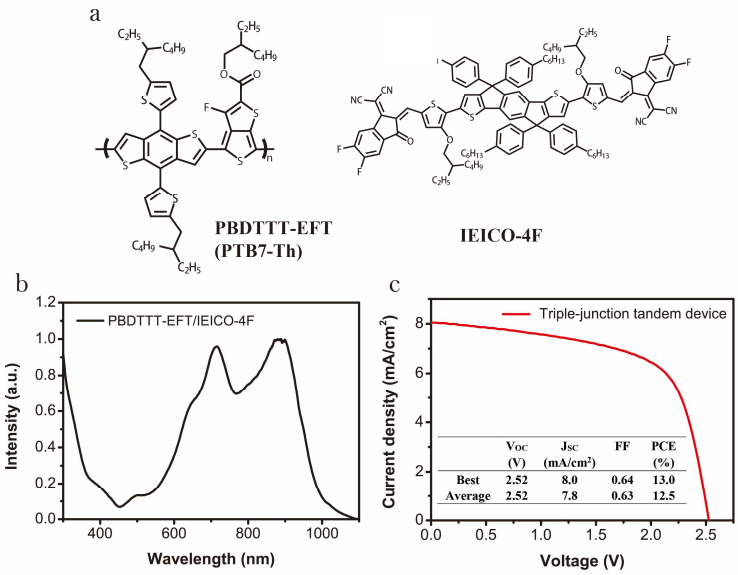

Figure 5-8 (a) Chemical structures of PTB7-Th and IEICO-4F films. **(b)** UV-vis absorption spectra of PTB7-Th:IEICO-4F blend. **(c)** I-V curves of triple-junction organic tandem solar cells (front sub-cell: PDBT-T1:TPH-Se:ITIC, middle sub-cell: PBDBT:ITIC and rear sub-cell: PBDTTT-EFT:IEICO-4F).

5.3 Summary

In summary, we have successfully fabricated high efficiency non-fullerene organic tandem solar cells consisting of ternary non-fullerene acceptor sub-cells. An unique approach that enables the optimization of current matching by tuning the chemical composition of the ternary blend was present. The blend of PDBT-T1:TPH-Se:ITIC was selected as the front sub-cell because of its highly mixed morphology that can suppress severe phase separation upon heat treatment. Therefore, the device based on this blend can largely preserve its original efficiency even after long-term heat treatment, enabling a facile fabrication of high quality ICLs. After optimizing the chemical composition in PDBT-T1:TPHSe: ITIC blend, a more balanced current has been achieved between PDBT-T1:TPH-Se:ITIC ternary front sub-cell and PBDB-T:ITIC rear sub-cell. The efficiency of the champion cells increases from 10.6% to 11.5%. The incorporation of 10 wt.% ITIC not only enhances the light absorption, but also facilitates the charge separation via the cascade energy level. When the third junction PBDTTTEFT: IEICO-4F was applied to further extend the absorption spectra to the NIR region, the efficiency of 13% has been achieved in the champion triple-junction tandem device (with an average efficiency of 12.5%), with an ultra-high open circuit voltage of 2.52 V.

The results presented in this manuscript not only demonstrate the potential of using non-fullerene sub-cells to fabricate a high efficiency organic tandem photovoltaic, but also provide some design rules on the ways of further improving the device performance. First, as most ICLs require a heat treatment to improve their quality, the fabrication of a highly efficient and thermal-stable front sub-cell is necessary. The thermal stability can be significantly improved by suppressing the phase separation during the heat treatment via proper selection of materials and meticulous optimization of the morphology. Second, in addition to varying the thickness of each

sub-cell, the challenge of matching the current can also be addressed by careful engineering chemical composition in a ternary sub-cell. This approach can effectively tune the absorption spectra via chemical composition engineering at the optimized active layer thickness and bypass device performance degradation due to the variation of active layer thickness.

5.4 Experimental Design Method

5.4.1 Chemicals

PDBT-T1 and TPH-Se were synthesized according to the literature.[8,11-14] PBDTTT-EFT, PBDBT, ITIC and IEICO-4F were purchased from 1-Materials. 1,8-diiodooctance (DIO) and chlorobenzene (CB) were supplied from Sigma-Aldrich.

5.4.2 Device Fabrication

The single junction organic solar cell was fabricated in an inverted structure of ITO/ZnO/active layer/MoO3/Ag. The ITO glasses were washed in an ultrasonic bath of acetone and isopropanol and then treated with ultraviolet-ozone for 15 min. The ZnO layer was prepared via sol-gel process with a thickness of 30 nm. The PDBT-T1:TPH-Se:ITIC ternary blends with different ratios were spun from a mixed solvent of CB and DIO (99.25 : 0.75 vol.%) at 1000 rpm for 45 s, followed by thermally annealing at 100 °C for 5 min. The concentration of PDBT-T1 was fixed at 7 mg/ml. The PBDBT:ITIC (11 mg/ml : 11 mg/ml) blend were spin-coated from a mixed solvent of CB and DIO (99.5 : 0.5 vol.%) at 2000 RPM for 45 s, followed by thermally annealing at 100 °C for 1 min. The PBDTTT-EFT:IEICO-4F (10 mg/ml:15 mg/ml) were spin-coated from a mixed solvent of CB and CN (97:3 vol.%) at 1500 rpm for 45 s. MoO3 (10 nm) and Ag (100 nm) were evaporated onto the active layer through a shadow mask. The active area of device was 0.1 cm^2. For the tandem device, after the deposition of the first active layer, MoO3 was thermally evaporated with a thickness of 6 nm. A thin layer of modified-PEDOT:PSS was spin-coated, followed by thermally annealing at 120 °C for 90 s. Another layer of ZnO was deposited from ZnO nanocrystal solution, followed by thermally annealing at 120°C for 90s. After the

deposition of the second active layer, MoO3 and Ag were consecutively thermally evaporated with same thicknesses in the single junction solar cell.

5.4.3 Characterization

Device Measurements The PCEs of solar cells were measured under 1 sun AM 1.5G spectrum with an Oriel 9600 solar simulator. External quantum efficiency (EQE) spectra were measured by using an integrated system (Enlitech). The short circuit was recorded with a lock-in amplifier. The device characterization of tandem solar cells was measured following the previous measurement.[17] In order to avoid parasitic current during device measurements, each device was absolutely isolated from surround devices. For EQE spectra measurement of each sub-cell, a bias light with the selected wavelength was applied.

Optical Characterization

The samples for UV-Vis measurement were prepared on the glass slide. The absorption spectra were collected by using a 4100 Hitachi spectrofluorophotometer.

Microstructural Characterization

GIWAXS experiments were conducted at the beamline 7.3.3. of the Advanced Light Source at Lawrence Berkeley National Laboratory. All the samples were deposited on silicon wafers following the same procedure as device fabrication. All the samples were irradiated by 10 KeV X-ray at a fixed angle of 0.14°. 2D scattering signals were probed by using a Dectris Pilatus 1M detector. The results were analyzed by an altered version of the NIKA 2D based in IgorPro.

References

1. Huang, W.; Cheng, P.; Yang, Y.; Li, G.; Yang, Y. (2018). High□Performance Organic Bulk□ Heterojunction Solar Cells Based on Multiple□Donor or Multiple□Acceptor Components. *Adv. Mater. 30*, 1705706.

2. Lu, L.; Kelly, M. A.; You, W.; Yu, L. (2015). Status and prospects for ternary organic photovoltaics. *Nat. Photon. 9*, 491-500.

3. Yang, L.; Zhou, H.; Price, S. C.; You, W. (2012). Parallel-like Bulk Heterojunction Polymer Solar Cells. *J. Am. Chem. Soc.* 134, 5432-5435.

4. Kan, B.; Yi, Y.Q.Q., Wan, X.; Feng, H.; Ke, X.; Wang, Y.; Li, C.; Chen, Y. (2018). Ternary Organic Solar Cells With 12.8% Efficiency Using Two Nonfullerene Acceptors With Complementary Absorptions. *Adv. Energy Mater. 8*,1800424.

5. Li, Z.; Xu, X.; Zhang, W.; Meng, X.; Genene, Z.; Ma, W.; Mammo, W.; Yartsev, A.; Andersson, M. R.; Janssen, R. A. J.; Wang, E. (2017). 9.0% power conversion efficiency from ternary all-polymer solar cells. *Energy Environ. Sci. 10*, 2212-2221.

6. Gasparini, N.; Jiao, X.; Heumueller, T.; Baran, D.; Matt, G. J.; Fladischer, S.; Spiecker, E.; Ade, H.; Brabec, C. J.; Ameri, T. (2016). Designing ternary blend bulk heterojunction solar cells with reduced carrier recombination and a fill factor of 77%. *Nat. Energy.* 1, 16118.

7. Ameri, T.; Li, N.; Brabec, C. J. (2013). Highly efficient organic tandem solar cells: a follow up review. *Energy Environ. Sci. 6*, 2390-2413.

8. You, J.; Dou, L.; Hong, Z.; Li, G.; Yang, Y. (2013). Recent trends in polymer tandem solar cells research. *Prog. Polym. Sci. 38*, 1909-1928.

9. Che, X.; Li, Y.; Qu, Y.; Forrest, S. R. (2018). High fabrication yield organic tandem photovoltaics combining vacuum- and solution-processed subcells with 15% efficiency. *Nat. Energy*. *3*, 422-427.

10. Zhang, Y.; Kan, B.; Sun, Y.; Wang, Y.; Xia, R.; Ke, X.; Yi, Y. Q. Q.; Li, C.; Yip, H. L.; Wan, X.; Cao, Y.; Chen, Y. (2018). Nonfullerene Tandem Organic Solar Cells with High Performance of 14.11%. *Adv. Mater. 30*, 1707508.

11. Li, M.; Gao, K.; Wan, X.; Zhang, Q.; Kan, B.; Xia, R.; Liu, F.; Yang, X.; Feng, H.; Ni, W.; Wang, Y.; Peng, J.; Zhang, H.; Liang, Z.; Yip, H.-L.; Peng, X.; Cao, Y.; Chen, Y. (2017). Solutionprocessed organic tandem solar cells with power conversion efficiencies >12%. *Nat. Photon 11*, 85-90.

12. You, J.; Dou, L.; Yoshimura, K.; Kato, T.; Ohya, K.; Moriarty, T.; Emery, K.; Chen, C.-C.; Gao, J.; Li, G.; Yang, Y. (2013). A polymer tandem solar cell with 10.6% power conversion efficiency. *Nat. Commun. 4*, 1446.

13. Cui, Y.; Yao, H.; Gao, B.; Qin, Y.; Zhang, S.; Yang, B.; He, C.; Xu, B.; Hou, J. Fine-Tuned Photoactive and Interconnection Layers for Achieving over 13% Efficiency in a Fullerene-Free Tandem Organic Solar Cell. (2017). *J. Am. Chem. Soc. 139*, 7302-7309.

14. Xu, X.; Yu, T.; Bi, Z.; Ma, W.; Li, Y.; Peng, Q. (2018). Realizing Over 13% Efficiency in Green-Solvent-Processed Nonfullerene Organic Solar Cells Enabled by 1,3,4-Thiadiazole-Based Wide-Bandgap Copolymers. *Adv. Mater. 30*, 1703973.

15. Li, W.; Furlan, A.; Hendriks, K. H.; Wienk, M. M.; Janssen, R. A. J. (2013). Efficient Tandem and Triple-Junction Polymer Solar Cells. *J. Am. Chem. Soc. 135*, 5529-5532.

16. Guo, F.; Li, N.; Fecher, F. W.; Gasparini, N.; Quiroz, C. O. R.; Bronnbauer, C.; Hou, Y.; Radmilović, V. V.; Radmilović, V. R.; Spiecker, E.; Forberich, K.; Brabec, C. J. (2015). A generic concept to overcome bandgap limitations for designing highly efficient multi-junction photovoltaic cells. *Nat. Commun. 6*, 7730.

17. Prosa, M.; Li, N.; Gasparini, N.; Bolognesi, M.; Seri, M.; Muccini, M.; Brabec, C. J. (2017). Revealing Minor Electrical Losses in the Interconnecting Layers of Organic Tandem Solar Cells. *Adv. Mater. Inter. 4*, 1700776.

18. Huang, W.; Gann, E.; Chandrasekaran, N.; Prasad, S. K. K.; Chang, S.-Y.; Thomsen, L.; Kabra, D.; Hodgkiss, J. M.; Cheng, Y.-B.; Yang, Y.; McNeill, C. R. (2017). Influence of Fullerene Acceptor on the Performance, Microstructure, and Photophysics of Low Bandgap Polymer Solar Cells. *Adv. Energy Mater. 7*, 1602197.

19. Meng, D.; Fu, H.; Xiao, C.; Meng, X.; Winands, T.; Ma, W.; Wei, W.; Fan, B.; Huo, L.; Doltsinis, N. L.; Li, Y.; Sun, Y.; Wang, Z. (2016). Three-Bladed Rylene Propellers with Three-Dimensional Network Assembly for Organic Electronics. *J. Am. Chem. Soc. 138*, 10184-10190.

20. Huo, L.; Liu, T.; Sun, X.; Cai, Y.; Heeger, A. J.; Sun, Y. (2015). Single-Junction Organic Solar Cells Based on a Novel Wide-Bandgap Polymer with Efficiency of 9.7%. *Adv. Mater. 27*, 2938-2944.

21. Cheng, P.; Li, Y.; Zhan, X. (2014). Efficient ternary blend polymer solar cells with indene-C60 bisadduct as an electron-cascade acceptor. *Energy Environ. Sci. 7*, 2005-2011.

22. Su, W.; Fan, Q.; Guo, X.; Guo, B.; Li, W.; Zhang, Y.; Zhang, M.; Li, Y. (2016). Efficient ternary blend all-polymer solar cells with a polythiophene derivative as a hole-cascade material. *J. Mater. Chem. A 4*, 14752-14760.

Chapter 6 High Performance Organic Tandem Solar Cells Based on Ternary Sub-Cells-2

(This chapter is based on the manuscript submitted to *Joule*)

Herein, a simple strategy to balance the voltage-current trade-off in tandem OPVs by employing mixed non-fullerene acceptors in rear sub-cells was reported. The V_{oc} and J_{sc} of rear sub-cells can be tuned by using the blend of donor/non-fullerene acceptor/ non-fullerene acceptor. This strategy offers an easy approach to balance the V_{oc} and J_{sc} in tandem OPVs towards higher PCE without rational and careful synthesis of new materials. Tandem OPVs based on the mixed non-fullerene acceptors in rear sub-cell exhibited the best PCE of 13.3% in the lab. Importantly, the tandem devices were certified by National Renewable Energy Laboratory (NREL) under the new protocols (asymptotic scans), a PCE of 11.52% was achieved and recognized on the most recent NREL chart (December 2018).

6.1 Motivation

The progress of tandem OPVs was slow down in recent years due to the limitations of the fullerene acceptor (i.e. weak absorption in the NIR regions, insufficient thermal stability caused by easy aggregations, and large V_{oc} losses). Considering the unique advantages of non-fullerene acceptors (NFAs) over the fullerene acceptors,[1-4] the combination of NFAs and the tandem concept shows a great potential for very high performance OPVs: (1) the bandgap of NFAs can be tuned between 1.2 to 2.4 eV which can either broaden the absorption in the NIR region for the rear sub-cell or narrow the absorption to the blue region for the front sub-cell; [5-10] (2) the V_{OC} loss of single-junction NFA-based solar cells can be minimized to 0.4-0.6 V,[11-14] which guarantees small V_{oc} loss of tandem NFA-based solar cells; (3) the improved thermal stability of the NFA-based sub-cells is potentially robust towards the unavoidable thermal treatments of the ICL.[15,16] However, the trade-off between the V_{oc} and the J_{sc} in tandem OPVs is still challenging to balance, which limits further enhancement of efficiency. Concerning the tedious and complex nature of organic synthesis, a simple strategy to balance the trade-off between the V_{oc} and the J_{sc} in tandem OPVs would be highly desirable.

6.2 Result and discussion

6.2.1 Front and Rear Sub-cells for Tandem Solar Cell

In this work, a wide bandgap polymer PBDB-T (Eg = 1.85 eV) and a medium bandgap polymer PTB7-Th (Eg = 1.63 eV) were used as donors. A medium bandgap non-fullerene small molecule IT-M (Eg = 1.63 eV) and two narrow bandgap non-fullerene small molecules FOIC (Eg=1.33 eV) and F8IC (Eg=1.29 eV) were used as acceptors. The molecular structures and absorption spectra of these donors and acceptors are shown in **Figure 6.1.**

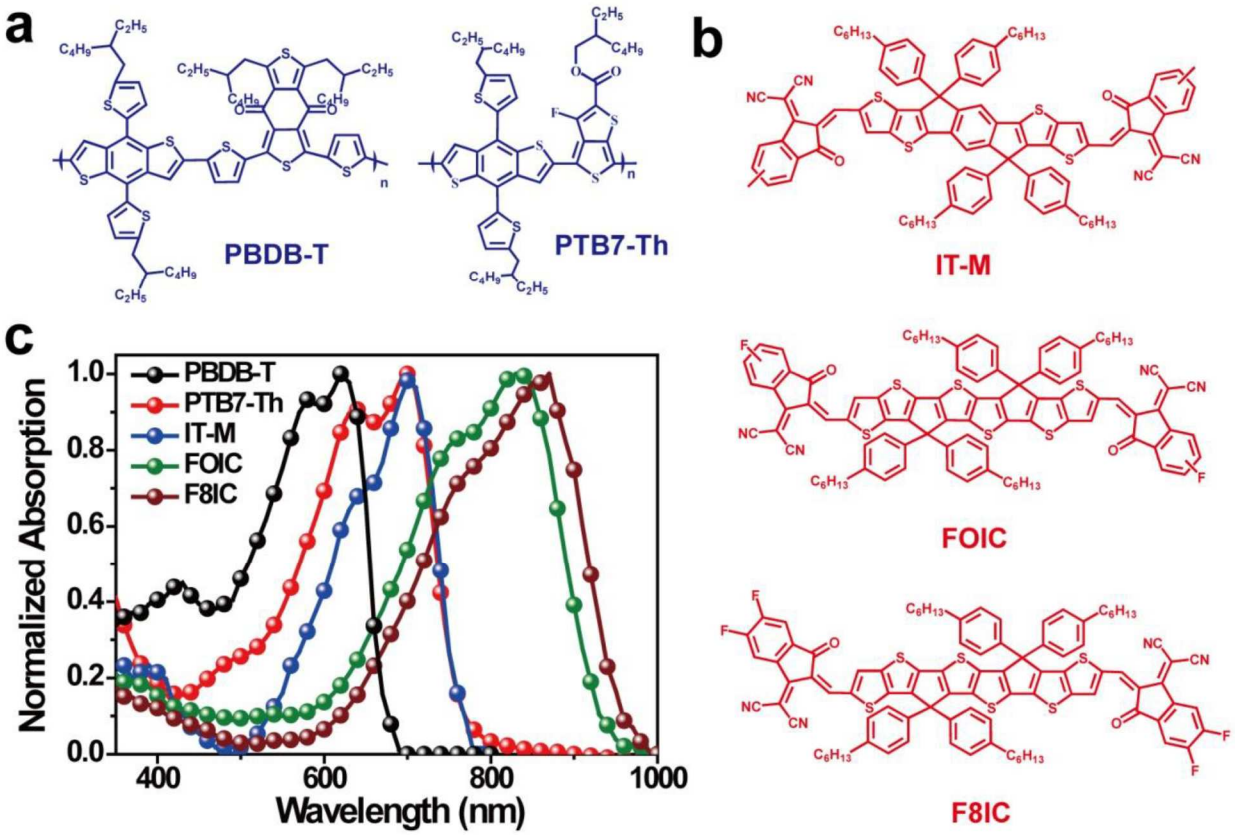

Figure 6-1 (Molecular structures and film absorption **(a)** Molecular (donor) structures of PBDB-T and PTB7-Th. **(b)** Molecular (acceptor) structures of IT-M, FOIC and F8IC. **(c)** Film absorptions spectra of PBDB-T, PTB7-Th, IT-M, FOIC and F8IC.

The J–V curves and EQE spectra of single-junction devices under the illumination of an AM 1.5 G solar simulator (100 mW/cm^2) are shown in **Figure 6-2**. The average (calculated from 15 individual devices) and the best device characteristics are summarized in **Table 6-1**. The geometry of single-junction device is inverted type: ITO/ZnO/active layer/MoO3/Ag. The front sub-cells were fabricated using PBDB-T as a donor and IT-M as an acceptor, resulting in an absorption edge at around 770 nm (Eg = 1.61 eV, extracted by EQE spectrum). The average V_{oc}, J_{sc}, FF and PCE of PBDB-T/IT-M front sub-cells are 0.91 V, 16.3 mA/cm^2, 71.4% and 10.6%, respectively. The rear sub-cells were fabricated by using the blend of PTB7-Th, FOIC and F8IC.

Compared to FOIC, the F8IC has similar chemical structure but contains two more fluorine substituent groups, which can down-shift the LUMO energy level (0.08 eV) and the HOMO energy level (0.04 eV), and finally reduce the bandgap (0.04 eV). In Rear 1 sub-cell (FOIC/F8IC=0/100), the average V_{OC} and J_{SC} are 0.67 V and 22.7 mA/cm^2, respectively. After the increasing of the FOIC content in the mixed acceptors, the V_{oc} increases (0.70 V for Rear 2 (FOIC/F8IC=25/75), 0.72 V for Rear 3 (FOIC/F8IC=50/50), 0.73 V for Rear 4 (FOIC/F8IC=75/25) and 0.75 V for Rear 5 (FOIC/F8IC=100/0)) and the J_{SC} decreases (22.2 mA /cm^2 for Rear 2, 21.9 mA/cm^2 for Rear 3, 21.3 mA/cm^2 for Rear 4 and 20.5 mA/cm^2 for Rear 5). As a result, Rear 1 to 5 exhibit different absorption edges (961 nm for Rear 1, 955 nm for Rear 2, 948 nm for Rear 3, 941 nm for Rear 4 and 932 nm for Rear 5, extracted by EQE spectra) but similar average FFs (ca. 70%) and PCEs (10.6 - 10.8%). In order to study the mechanism that affords the tunability of the bandgap and the V_{OC} of devices, LUMO and HOMO energy levels of FOIC/F8IC mixed acceptors were calculated by electrochemical cyclic voltammetry. The results are shown in **Figure 6-3(a)** and **(b)**. The LUMO and HOMO energy levels increase with the increasing of the FOIC contents. The tunability of the bandgap is attributed to the tuning of LUMO and HOMO energy levels of the mixed acceptors. In addition, the tunable LUMO energy level of the mixed acceptors is the reason for the tunable V_{oc} since the V_{oc} of devices is determined by the gap between the HOMO energy level of donor and LUMO energy level of acceptor.

From the integration of EQE spectra with AM 1.5G reference spectra, the calculated J_{SC} was obtained, which is similar to the *J–V* measurement (the average error is 1.3%, **Table 6-1**). Thermal stress (continuously heating) was employed to investigate the stability of the front and real sub-cells. As a result, the front and rear sub-cells exhibit good thermal stability, preserving

95% and 91% of their original values after continuously heating at 100 °C for 60 min, respectively (**Figure 6-3(c)**).

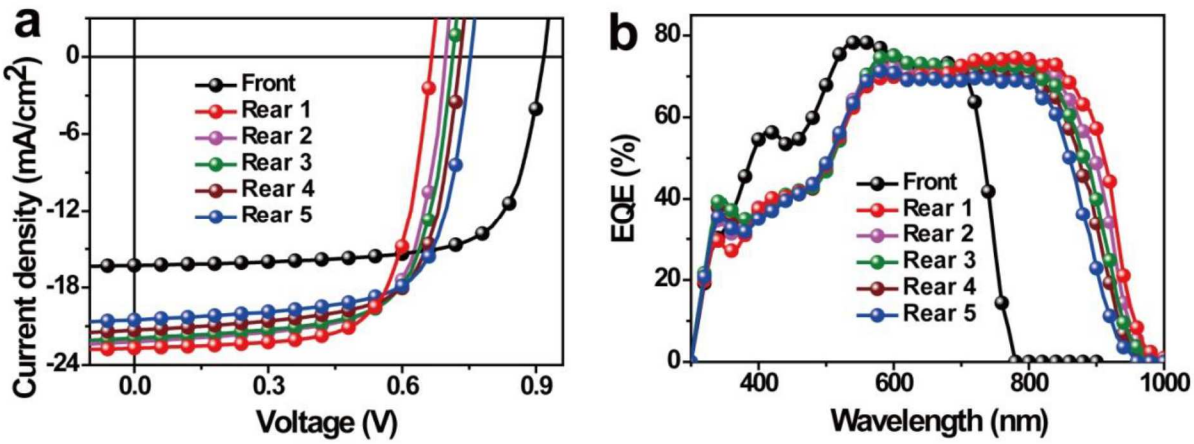

Figure 6-2 (a) J–V curves of single-junction devices under illumination of an AM 1.5G solar simulator, 100 mW/cm^2. (b) EQE spectra of single-junction devices.

Device	**Donor**	**Acceptor (m/m)**	V_{OC} **(V)**	J_{sc} **(mA/cm^2)**	**Calculated** J_{sc} **(mA/cm^2)**	**FF (%)**	**PCE (%)**	
							average	**best**
Front	PBDB-T	IT-M	0.91±0.01	16.3±0.3	16.0	71.4±0.8	10.6±0.3	11.0
Rear 1	PTB7-Th	FOIC/F8IC (0/100)	0.67±0.01	22.7±0.4	22.4	69.5±0.8	10.6±0.2	10.9
Rear 2	PTB7-Th	FOIC/F8IC (25/75)	0.70±0.01	22.2±0.3	22.0	69.0±0.5	10.7±0.2	11.0
Rear 3	PTB7-Th	FOIC/F8IC (50/50)	0.72±0.01	21.9±0.5	21.7	69.1±0.6	10.8±0.2	11.1
Rear 4	PTB7-Th	FOIC/F8IC (75/25)	0.73±0.01	21.3±0.3	21.0	69.6±0.4	10.8±0.2	11.1
Rear 5	PTB7-Th	FOIC/F8IC (100/0)	0.75±0.01	20.5±0.4	20.2	69.5±0.5	10.7±0.2	11.0

Table 6-1 Photovoltaic characteristics of single-junction devices.

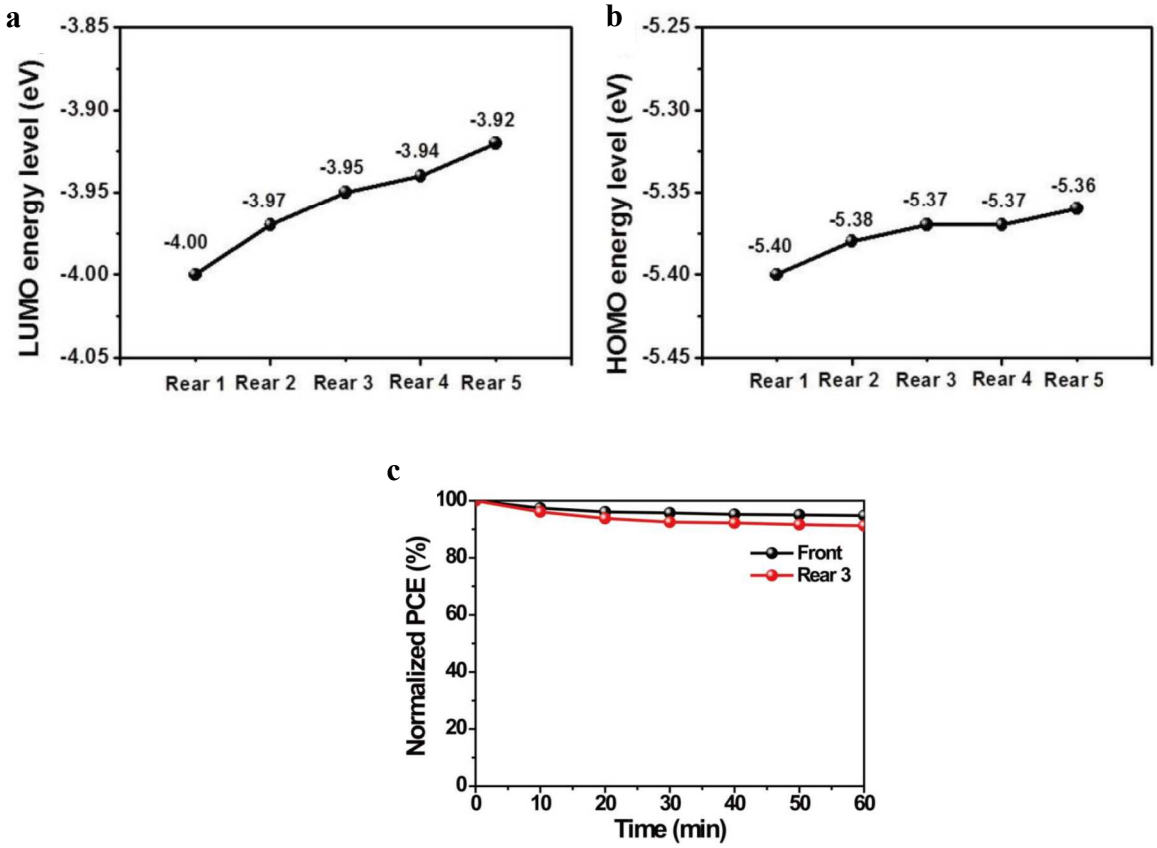

Figure 6-3 (a) LUMO and **(b)** HOMO energy levels of FOIC/F8IC mixed acceptors used in Rear 1 to 5. **(c)** Thermal stability tests of front sub-cell (PBDB-T/IT-M) and rear sub-cell (Rear 3: PTB7-Th:FOIC:F8IC).

6.2.2 Molecular Packing Behaviors of the Active Materials

In order to study the molecular packing behaviors in the active layers of Rear 1 to 5, GIWAXS measurements were carried out. GIWAXS can provide molecular-level structural information such as lattice constant and orientation of material packing. The 2D GIWAXS patterns of PTB7-Th/FOIC/F8IC blends in different rear sub-cells (Rear 1 to 5) and pure F8IC/pure FOIC films are shown in **Figure 6-4**, respectively. The 1D GIWAXS profiles in both out-of-plane and in-plane directions are shown in **Figure 6-5**. The molecular packing in pure

F8IC film is similar to that of pure FOIC film in terms of the orientation of material packing, as indicated by the similar ring-like lamellar peak at q = 0.4 $Å^{-1}$ and similar π–π stacking peak (q = 1.7 $Å^{-1}$) on out-of-plane direction. As shown in **Figure 6-4**, the packing behaviors of FOIC/F8IC are similar in all PTB7-Th/FOIC/F8IC active layers of Rear 1 to 5, which show similar peaks at q = 0.4 $Å^{-1}$ on in-plane direction (face-on) and at q = 1.7 $Å^{-1}$ on out-of-plane direction (face-on). The maintained film morphology of PTB7-Th/FOIC/F8IC active layer in a wide range of FOIC/F8IC ratios (0/100 to 100/0) is attributed to the similarity in chemical structures between FOIC and F8IC (good compatibility), which leads to similar FFs (ca. 70%) of all Rear 1 to 5 devices.

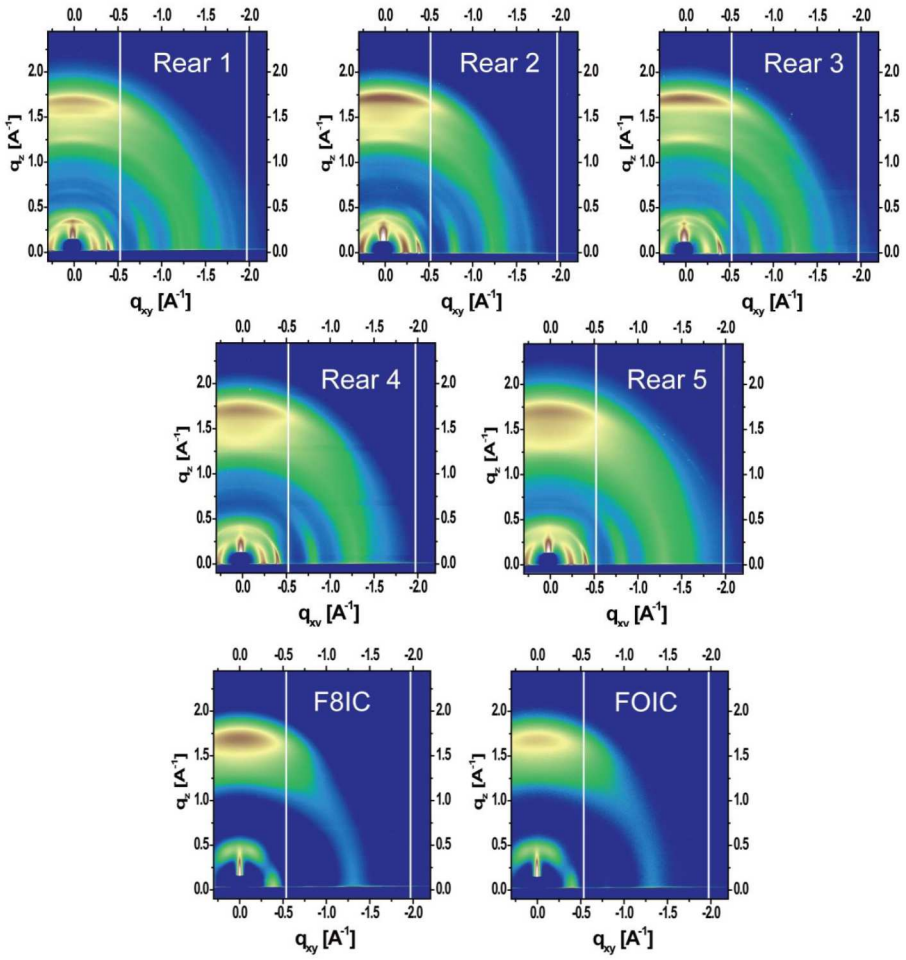

Figure 6-4 2D GIWAXS patterns of PTB7-Th/FOIC/F8IC blends in different rear sub-cells and F8IC as well as FOIC.

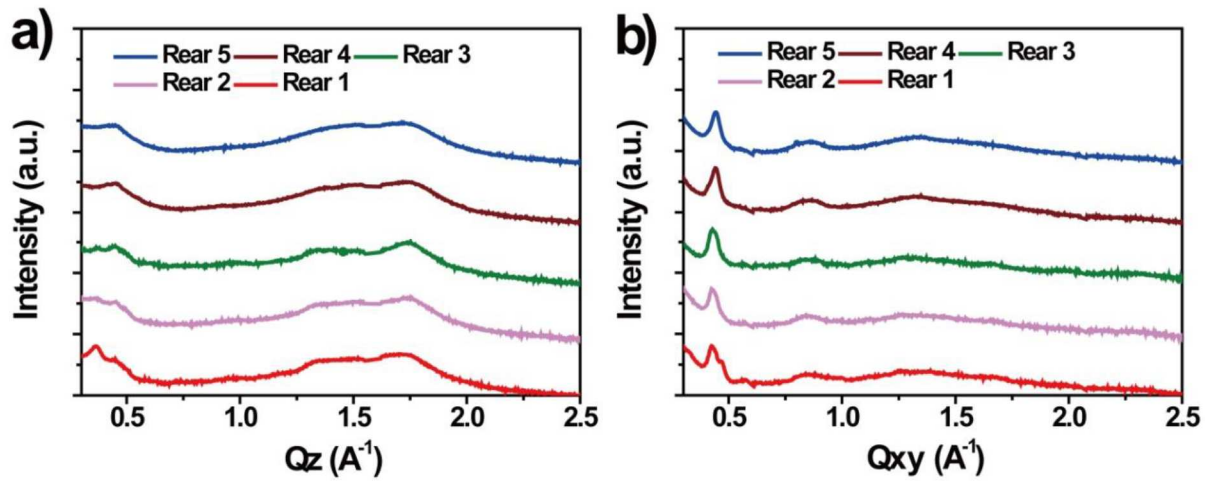

Figure 6-5 (a) Out-of-plane and (b) in-plane 1D GIWAXS profiles of PTB7-Th/FOIC/F8IC blends in different rear sub-cells.

6.2.3 Current Matching Design of The Tandem Solar Cells

The geometry of tandem device is also inverted type: ITO/ZnO/PBDB-T: IT-M/ICL/PTB7-Th:FOIC:F8IC/MoO3/Ag (**Figure 6-6(a)**). The ICL is composed of MoO_3, Mix-PEDOT:PSS (4083 and PH 500, 7:3, v/v) and ZnO. The energy alignments of all materials used in tandem devices are shown in **Figure 6-6(b)**. The energy levels of donors/acceptors were extracted from literature, and the work functions of materials in ICL were calculated using UPS tests (**Figure 6-7**). The average (calculated from 20 individual devices) and the best device characteristics of tandem devices based on different rear sub-cells are summarized in **Table 6-2**. By employing different rear sub-cells (Rear 1 to 5), the V_{oc} and J_{sc} of tandem devices can be easily tuned. The average V_{oc} of tandem devices can be tuned from 1.57 V to 1.66 V (from Rear 1 to Rear 5). The average J_{sc} of tandem devices can also be tuned from 11.1 mA/cm^2 to 9.9 mA /cm^2 (from Rear 1 to Rear 5), since the J_{SC} of front sub-cell can be tuned by thickness of PBDB-T/IT-M active layer to match the JSC of rear sub-cell towards optimized PCE. By this strategy, the V_{OC} and J_{SC} in tandem OPVs can be easily balanced towards higher PCE without a rational

and careful synthesis of new acceptors (with a slight difference in bandgaps). The J–V curves and EQE spectra of tandem devices based on Rear 3 sub-cell under the illumination of an AM 1.5 G solar simulator (100 mW/cm^2) are shown in **Figure 6-6(c)** and **4(d)**. The average (calculated from 20 individual devices) and the best device characteristics of tandem devices based on Rear 3 with different combinations of front/rear sub-cell thickness are also summarized in **Table 6-3**. The average V_{oc}, J_{sc} and FF of tandem devices based on Rear 3 are 1.62 V, 10.6 mA/cm^2 and 73.9%, respectively. The best PCE of tandem devices based on Rear 3 (PTB7-Th/FOIC/F8IC, FOIC/F8IC=50/50) is as high as 13.3%, which is higher than the PCE measured in tandem devices based on PTB7-Th/F8IC binary blend (Rear 1, best PCE=12.7%) and tandem devices based on PTB7-Th/FOIC binary blend (Rear 5, best PCE=12.4%).

More importantly, the encapsulated tandem devices based on Rear 3 were certified by the NREL under the asymptotic scans.[17,18] The regular fast I-V scans ignore the hysteresis effects, depending on scan rates and directions and light bias exposure history etc. These fast scans may have resulted in some exaggerated efficiency reports. Asymptotic scans are measured by holding the cell at each voltage until the current reaches an asymptotic level, which is a tougher and accurate measurement than the fast scans. The I–V measured results and EQE spectra of tandem devices based on Rear 3 certified by the NREL are shown in **Figure 6-6(e)** and **Figure 6-8**, respectively. The V_{oc} and FF measured by the NREL are lower than the results measured in our lab due to the possible slight degradations caused by encapsulation, shipment and the asymptotic scans. The certified devices were re-measured in our lab after the tests by the NREL, similar results were achieved in our lab as the certified results from NREL. Finally, a PCE of 11.52% was certified by the NREL under the new protocols.

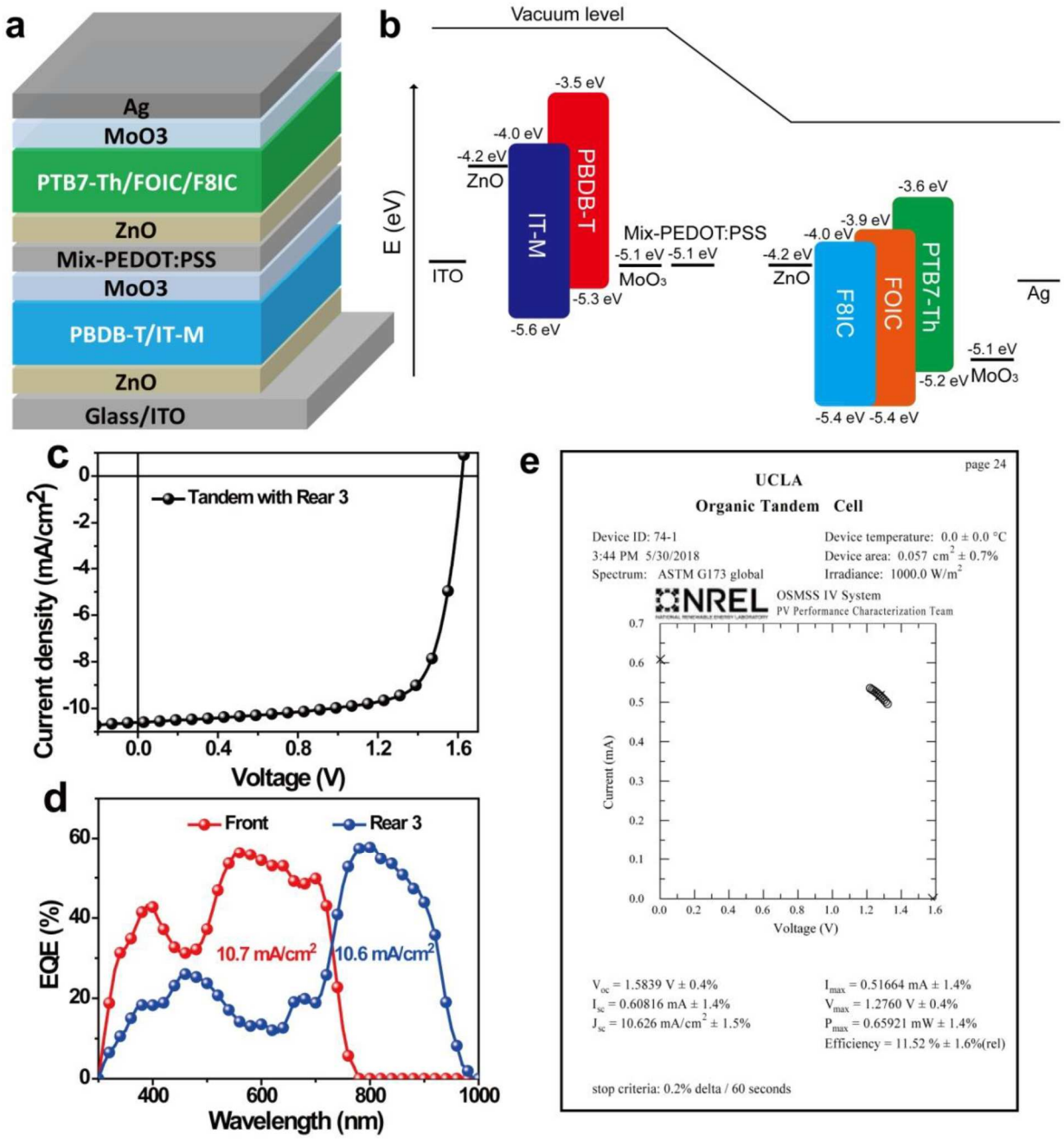

Figure 6-6 Device structure, energy alignments and photovoltaic characteristics of tandem devices **(a)** Device structure. **(b)** Energy levels of donor and acceptor materials, and work functions of inter layers. **(c)** J–V curve of tandem device (based on Rear 3 sub-cell) under illumination of an AM 1.5G solar simulator, 100 mW/cm^2. **(d)** EQE spectra of tandem device (based on Rear 3 sub-cell). **(e)** Photovoltaic characteristics of tandem device (based on Rear 3 sub-cell) with the NREL certification (asymptotic scans on encapsulated devices).

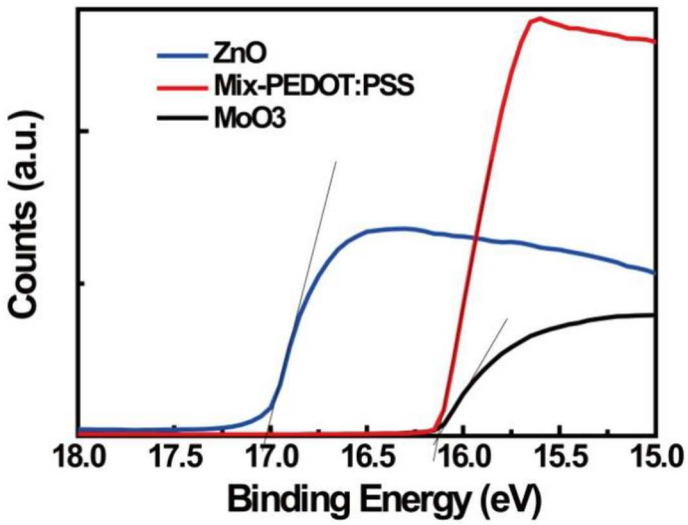

Figure 6-7 The work function data of different transport layers.

Combination	V_{OC} (V)	Measured J_{SC} (mA/cm^2)	Calculated J_{SC} (mA/cm^2) Front/Rear	FF (%)	PCE (%)	
					average	best
Front/Rear 1	1.57±0.01	11.1±0.2	11.1/11.1	71.2±0.6	12.4±0.2	12.7
Front/Rear 2	1.60±0.01	10.8±0.2	10.9/10.8	72.3±0.7	12.5±0.2	12.9
Front/Rear 3	1.62±0.01	10.6±0.3	10.7/10.6	73.9±0.8	12.7±0.3	13.3
	1.5839	10.626	N/A	68.4	11.52[1]	
Front/Rear 4	1.64±0.01	10.3±0.3	10.3/10.3	73.5±0.5	12.4±0.3	12.9
Front/Rear 5	1.66±0.01	9.9±0.2	10.1/9.9	72.9±0.7	12.0±0.2	12.4

[1]Certified by the NREL

Table 6-2 Photovoltaic characteristics of tandem devices based on different rear sub-cells.

Front/Rear Sub-cell thickness (nm)	V_{OC} (V)	Measured J_{SC} (mA/cm^2)	Calculated J_{SC} (mA/cm^2) Front/Rear	FF (%)	PCE (%)	
					average	best
115/80	1.62±0.01	10.3±0.3	10.3/10.8	74.3±0.6	12.4±0.2	12.9
125/80	1.62±0.01	10.6±0.3	10.7/10.6	73.9±0.8	12.7±0.3	13.3
135/80	1.62±0.01	10.3±0.4	11.0/10.3	72.5±0.5	12.1±0.3	12.6
125/70	1.62±0.01	10.3±0.3	10.8/10.3	74.1±0.7	12.4±0.3	12.8
125/90	1.62±0.01	10.5±0.3	10.5/10.8	72.4±0.8	12.3±0.3	12.8

Table 6-3 Photovoltaic characteristics of tandem devices based on Rear 3 with different combinations of front/rear sub-cell thickness.

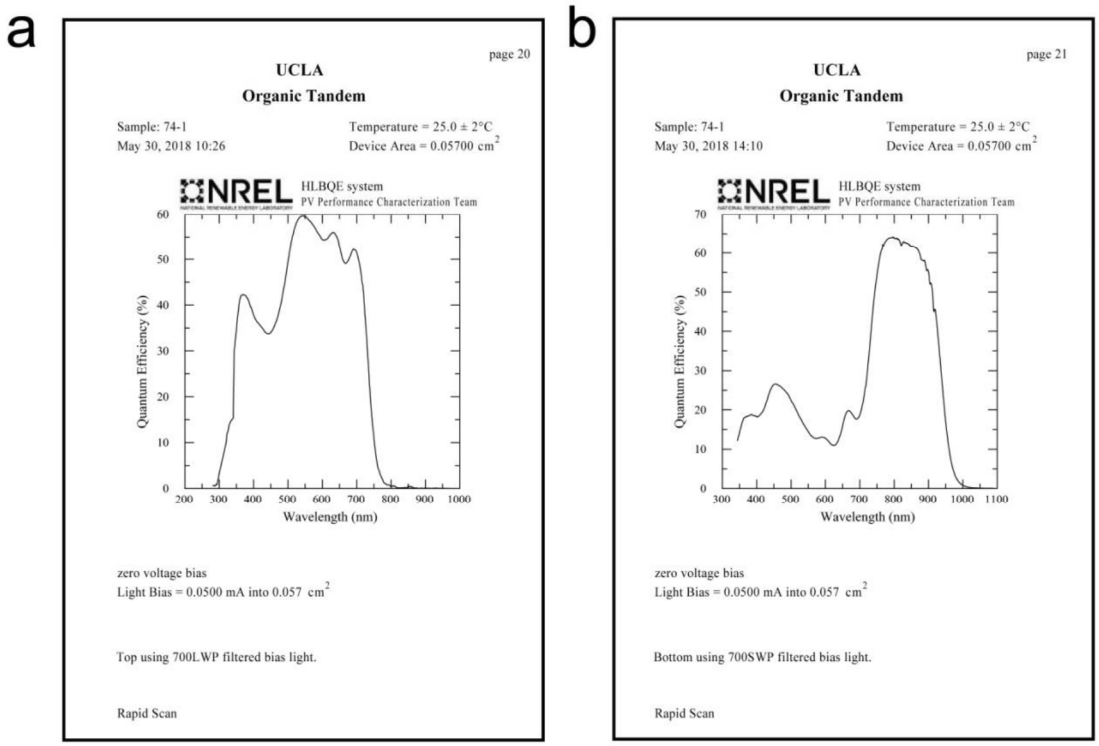

Figure 6-8 EQE spectrum of **(a)** front sub-cell and **(b)** rear sub-cell tested by NREL.

6.2.4 Simulation Results of Tandem Solar Cells

The light field simulations were carried out for studying the appropriate combination of the tandem design and shown in **Figure 6-9**. In the simulation, the front and Rear 3 sub-cells of tandem devices were set to thickness values ranging from 70 to 135 nm. After the optimization of thickness values, the integrated J_{sc} of the front sub-cell (125 nm) and rear sub-cell (80 nm) were able to be matched well (13.7 mA/cm^2 for front sub-cell and 13.7 mA cm^{-2} for rear sub-cell), which is consistent with the trend observed in our J-V tests (**Table 6-3**). The measured JSC (10.6 mA/cm^2) is much lower than the one in the simulation (13.7 mA/cm^2) since the simulation assumes the internal quantum efficiency to be 100% and no energy losses in ICL.

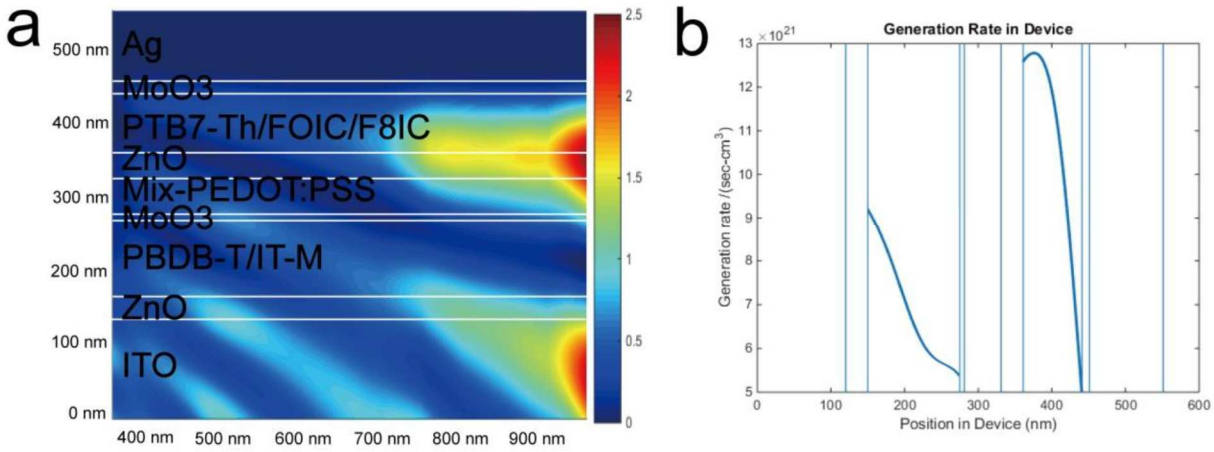

Figure 6-9 (a) The light field distribution of tandem device based on Rear 3 (125 nm for front sub-cell and 80 nm for rear sub-cell). **(b)** Generation rate of tandem device based on Rear 3 (125 nm for front sub-cell and 80 nm for rear sub-cell).

6.3 Summary

In summary, a simple strategy to balance the trade-off between the V_{oc} and the J_{sc} in tandem OPV by employing mixed NFAs in rear sub-cells was reported. The V_{oc} and J_{sc} of the rear sub-cells can be tuned in a wide range by using the blend of PTB7-Th/FOIC/F8IC: the V_{oc} can be tuned (0.67-0.75 V) due to the difference between the LUMO energy levels of two acceptors FOIC (-3.9 eV) and F8IC (-4.0 eV); the J_{sc} can be tuned (20.5-22.7 mA/cm^2) due to the difference between the optical bandgaps of two acceptors FOIC (1.33 eV) and F8IC (1.29 eV). Thanks to the similarity in chemical structures between FOIC and F8IC (good compatibility), the film morphology of PTB7-Th/FOIC/F8IC active layer can be maintained in a wide range of FOIC/F8IC ratios (0/100 to 100/0), which leads to similar FFs (ca. 70%). By this strategy, the V_{oc} and J_{sc} in tandem OPV (PBDB-T/IT-M as the front sub-cells, Eg=1.63 eV) can be easily balanced towards higher PCE without a rational and careful synthesis of new acceptors (with a slight difference in bandgaps). As a result, tandem devices based on Rear 3 (PTB7-Th/FOIC/F8IC, FOIC/F8IC=50/50) with the best PCE of 13.3% is achieved in our lab. More importantly, the encapsulated tandem devices based on Rear 3 were tested by the NREL under the new protocols (asymptotic scans, which are much tougher than regular fast scans), a PCE of 11.52% is achieved and recognized on the most recent NREL chart.

6.4 Experimental Design Method

6.4.1 Chemicals

Unless stated otherwise, solvents and chemicals were obtained commercially and used without further purification. PBDB-T, IT-M and PTB7-Th were purchased from Solarmer Materials Inc. FOIC and F8IC were synthesized according to our previously reported procedures.[19,20] 1,8-Diiodooctane (DIO), chlorobenzene (CB) and chloroform (CF) were obtained from Sigma-Aldrich Inc.

6.4.2 Device Fabrication

Single-junction organic solar cells were fabricated using with the following structure: ITO/ ZnO/active layer/MoO_3/Ag. The ITO glass was pre-cleaned in an ultrasonic bath of acetone and isopropanol, and treated in ultraviolet-ozone chamber (Jelight Company, USA) for 15 min. A ZnO sol-gel solution (100 mg zinc acetate dehydrate and 45 μL ethanolamine were added into 1mL 2-methoxyethanol, followed by stirring at 60 °C for 3 hours.) was spin-coated (3000 RPM) onto the ITO glass to form a thin ZnO film (30 nm) and baked at 200 °C for 60 min. A mixture of PBDB-T/IT-M was dissolved in CB solvent (1:1, 20 mg/ml in total, with 0.75% DIO, v/v) and stirred overnight. A mixture of PTB7-Th/FOIC/F8IC was dissolved in CF solvent (8:x:12-x, 15 mg/ml in total, with 0.25% DIO, v/v) and stirred for one hour. Afterwards, these solutions were spin-coated (1500-2500 RPM) on the ZnO layer to form photosensitive layers. A MoO_3 (ca. 10 nm) and Ag (ca. 100 nm) layers were then evaporated onto the surface of the photosensitive layer under vacuum (ca. 10−5 Pa) to form the back electrode. The active area of the device was 0.1 cm^2 (with mask).

For the tandem devices: the front sub-cells were prepared according to the single-junction procedure (ITO/ZnO/active layer), after which the samples were transferred into the evaporation chamber for MoO3 buffer layer deposition. The thickness of MoO_3 was 6 nm. Mix-PEDOT:PSS solution was prepared by mixing PEDOT:PSS 4083 and PH500 with a ratio of 7:3 (v/v) and ultra-sonicating for 5 minutes. The Mix-PEDOT:PSS solution was then spin-casted (5000 RPM) onto MoO_3 layer and annealed at 100 °C for 2 min. 1.68 g zinc acetate was put into 84 mL methanol followed by adding 600 μL DI water. The solution was heated to 60 °C with stirring. 1 g potassium hydroxide was dissolved into 42 mL methanol and then dropped into the zinc acetate/methanol solution within 15 min with stirring. After 2 h and 15 min, the reaction was stopped and the solution was cooled down overnight to precipitate the product. After that, the upper solution was removed and 80 mL methanol was added again to wash the precipitate product twice. Finally, the white precipitate was dispersed in the chloroform/butanol (3:7, v/v) to form a 10 mg/mL ZnO nanoparticle solution. After, ZnO nanoparticle solution was then spin-casted (2500 RPM) and thermal-annealed at 100 °C for 2 min. The rear sub-cells were also prepared according to the single-junction procedure (active layer/MoO3/Ag). The active area of the device was 0.1 cm^2 (with mask). Encapsulation was applied on the devices for certification, for which the active area of the device for certification was 0.057 cm^2 (with mask).

6.4.3 Characterization

Device Measurements The PCEs of solar cells were measured under 1 sun AM 1.5G spectrum with an Oriel 9600 solar simulator. External quantum efficiency (EQE) spectra were measured by using an integrated system (Enlitech). The short circuit was recorded with a lock-in amplifier. The device characterization of tandem solar cells was measured following the previous

measurement.[17] In order to avoid parasitic current during device measurements, each device was absolutely isolated from surround devices. For EQE spectra measurement of each sub-cell, a bias light with the selected wavelength was applied. Light biases of 550 and 800 nm were selected to excite the front and rear sub-cells, respectively. The unexcited sub-cell was then measured using a Xe lamp passing through a monochromator with a typical intensity of 10mW.

Optical Characterization

The samples for UV-Vis measurement were prepared on the glass slide. The absorption spectra were collected by using a 4100 Hitachi spectrofluorophotometer.

Microstructural Characterization

GIWAXS measurement was performed at Advanced Light Source on the 7.3.3. beamline. All samples were deposited on the silicon wafer with 100 nm silicon oxide. Samples were irradiated by 10 keV at a fixed X-ray incident angle of 0.10°-0.14° with an exposure time of 3 s. The results were analyzed by an altered version of the NIKA 2D based in IgorPro.

Ultraviolet Photoelectron Spectroscopy (UPS) Characterization

Ultraviolet photoelectron spectroscopy (UPS) measurements carried out in this work used a helium discharge lamp emitting photons with energy at 21.2 eV to excite the samples. The onset of the secondary electron edge was used to determine the work function under a −7 V bias applied between samples and detectors. Clean gold was used as a reference. The

Light Field Simulations

The light field simulations were carried out using a program based on the transfer matrix formalism. Light was simulated to be incident from glass substrate side, with optical field calculated in each location in the film stack. Absorption rate in the active layers was calculated every 5 nm together with AM 1.5G spectrum to obtain generation rate and thus short-circuit

photocurrent density. Optical field intensity was simulated and plotted at all wavelengths and locations in the film stack. The layers of tandem organic solar cells were regarded as homogeneous and isotropic with flat interfaces.

References

1. Cheng, P.; Li, G.; Zhan, X.; Yang, Y. (2018). Next-generation organic photovoltaics based on non-fullerene acceptors. *Nat. Photon. 12*, 131-142.

2. Yan, C.; Barlow, S.; Wang, Z.; Yan, H., Jen, A. K. Y.; Marder, S. R.; Zhan, X. (2018). Non-fullerene acceptors for organic solar cells. *Nat. Rev. Mater. 3*, 18003.

3. Hou, J.; Inganäs, O.; Friend, R. H.; and Gao, F. (2018). Organic solar cells based on non-fullerene acceptors. *Nat. Mater. 17*, 119-128.

4. Zhang, J.; Tan, H. S.; Guo, X.; Facchetti, A.; Yan, H. (2018). Material insights and challenges for non-fullerene organic solar cells based on small molecular acceptors. *Nat. Energy 3*, 720-731.

5. Lin, Y.; Wang, J.; Zhang, Z.-G.; Bai, H., Li, Y.; Zhu, D.; Zhan, X. (2015). An electron acceptor challenging fullerenes for efficient polymer solar cells. *Adv. Mater. 27*, 1170-1174.

6. Zhong, Y. et al. (2015). Molecular helices as electron acceptors in high-performance bulk heterojunction solar cells. *Nat. Commun. 6*, 8242.

7. Wu, Q.; Zhao, D.; Schneider, A. M.; Chen, W.; Yu, L. (2016). Covalently bound clusters of alpha-substituted PDI—rival electron acceptors to fullerene for organic solar cells. *J. Am. Chem. Soc. 138*, 7248-7251.

8. Yang, Y.; Zhang, Z.-G.; Bin, H., Chen, S.; Gao, L.; Xue, L.; Yang, C.; Li, Y. (2016). Side-chain isomerization on n-type organic semiconductor ITIC acceptor make 11.77% high efficiency polymer solar cells. *J. Am. Chem. Soc. 138*, 15011-15018.

9. Yao, H.; Cui, Y.; Yu, R.; Gao, B.; Zhang, H.; Hou, J. (2017). Design, synthesis, and photovoltaic characterization of a small molecular acceptor with an ultra-narrow band gap. *Angew. Chem. Int. Ed. 56*, 3045-3049.

10. Brunetti, F. G.; Gong, X.; Tong, M.; Heeger, A. J.;Wudl, F. (2010). Strain and huckel aromaticity: Driving forces for a promising new generation of electron acceptors in organic electronics. *Angew. Chem.-Int. Ed. 49*, 532-536.

11. Liu, J.; Chen, S.; Qian, D.; Gautam, B.; Yang, G.; Zhao, J.; Bergqvist, J.; Zhang, F.; Ma, W.; Ade, H.; Inganäs, O.; Gundogdu, K.; Gao, F.; Yan, H. (2016). Fast charge separation in a non-fullerene organic solar cell with a small driving force. *Nat. Energy 1*, 16089.

12. Cheng, P.; Zhang, M.; Lau, T.-K.; Wu, Y.; Jia, B.; Wang, J.; Yan, C.; Qin, M.; Lu, X.; Zhan, X. (2017). Realizing small energy loss of 0.55 eV, high open-circuit voltage >1 V and high efficiency >10% in fullerene-free polymer solar cells via energy driver. *Adv. Mater. 29*, 1605216.

13. Bin, H.; Gao, L.; Zhang, Z.-G.; Yang, Y.; Zhang, Y.; Zhang, C.; Chen, S.; Xue, L.; Yang, C.; Xiao, M.; Li, Y. (2016). 11.4% Efficiency non-fullerene polymer solar cells with trialkylsilyl substituted 2D-conjugated polymer as donor. *Nat. Commun. 7*, 13651.

14. Qian, D. et al. (2018). Design rules for minimizing voltage losses in high-efficiency organic solar cells. *Nat. Mater. 17*, 703-709.

15. Baran, D. et al. (2017). Reducing the efficiency-stability-cost gap of organic photovoltaics with highly efficient and stable small molecule acceptor ternary solar cells. *Nat. Mater. 16*, 363-369.

16. Holliday, S.; Ashraf, R. S.; Nielsen, C. B.; Kirkus, M.; Röhr, J. A.; Tan, C.-H.; Collado-Fregoso, E.; Knall, A.-C.; Durrant, J. R., Nelson, J.; McCulloch, I. (2015). A rhodanine flanked nonfullerene acceptor for solution-processed organic photovoltaics. *J. Am. Chem. Soc. 137*, 898-904.

17. Moriarty, T.; Levi, D. (2017). NREL's cell and module performance group's asymptotic pmax protocol for perovskite devices. Proceedings 44th IEEE Photovoltaic Specialists Conference, D51.

18. Moriarty, T.; Jablonski, J.; Emery, K. (2012). Algorithm for building a spectrum for NREL's one-sun multi-source simulator. Proceedings 38th IEEE Photovoltaic Specialists Conference, 001291-001295.

19. Li, T.; Dai, S.; Ke, Z.; Yang, L.; Wang, J.; Yan, C.; Ma, W.; Zhan, X. (2017) Fused tris(Thienothiophene)-based electron acceptor with strong near-infrared absorption for high-performance as-cast solar cells. *Adv. Mater. 30*, 1705969.

20. Dai, S.; Li, T.; Wang, W.; Xiao, Y.; Lau, T. K.; Li, Z.; Liu, K.; Lu, X.; Zhan, X. (2018) Enhancing the performance of polymer solar cells via core engineering of NIR-absorbing electron acceptors. *Adv. Mater. 30*, 1706571

Chapter 7 Conclusion and Future Outlooks

To summary, we have successfully adopted several strategies to enhance the photocurrent and overall performance of organic solar cells. These strategies include the utilization of new high mobility metal oxide transport material, work function modifying interconnecting material as well as the combination of ternary and tandem structure. High mobility In_2O_3 not only benefits the charge carrier transport but also helps the crystal growth of the polymer in the following as-cast photoactive layer. Transition metal chelate Zr-Acac possesses more suitable (Ultralow) work function for electron tunneling between each sub-cell so that the current of the device is raised. The problem of current matching in tandem solar cell is well solved by using ternary structure in the active layer to enable comparable current of front cell and rear cell. As predicted, the work function of the ternary sub-cell is also determined by the relative ratio of each polymer or small molecules. This provides more modification option for realizing a better electronic property of the sub-cell in the tandem solar cell. All of these efforts lead in the certified world record organic solar cell device efficiency.

Although the development of organic solar cell has boosted in this decade, there is yet room for performance improvement. The major bottleneck is still the lack of excellent photovoltaic materials. Due to the intrinsic properties (thin film < 200 nm) of organic semiconductors, the absorption spectrum cannot be a square-like shape to fully cover the range between its starting point and cutoff. This indeed limits the maximum photocurrent. Moreover,

the long-term stability of a constant output organic solar cell has not been satisfied ever. Exposing an organic solar cell in a light-intensified environment severely degrades its performance because of the instability of chemical chains under UV attack and the other light sensitizing factors.

Based on the above disadvantages, it seems like the future of massive scale application of organic solar cell is dim compared to the other mature and emerging PV technologies like silicon and perovskite. Nonetheless, there are the other possible scenarios for the application of organic solar cells. As described above, the nature of molecular orbitals makes the absorption spectra of organic semiconductors discontinuous as in inorganic semiconductors. This causes a major shortcoming for single-junction polymer PV in terms of their insufficient light absorption. However, this "disadvantage" of polymer PV can actually open a door to a new opportunity: selective transparent region, or visible region transparency.[1]

In order to achieve both good efficiency and visible transparency simultaneously, reducing the band gap is required to obtain a good IR absorbance. A general approach is to decrease the bond length alternation (BLA) value, which is the average of the difference in length between adjacent carbon-carbon bonds in a polyene chain. As the quinoid contribution in the polymer chain is raised, such as forming a mesomeric structure, the carbon-carbon single bonds between two adjacent rings can adopt more double bond characters and the BLA begins to decrease. The other useful way to decrease the BLA is to incorporate conjugated electron-rich donor (D) units and conjugated electron-deficient acceptor (A) units together in the same polymer backbone, which generate a strong push-pull driving force and, thus, enhance electron delocalization. This is also the most common design strategy for mostly current polymer materials of organic solar cell. Based on the D-A structure, strengthening one of the donor units,

acceptor units or both of them in the same polymer backbone can further reduce the band gap. Additionally, enhancing the intermolecular conjugation, such as strengthening planarization between adjacent aromatic units by forming additional covalent or non-covalent bond, can also decrease the BLA by inducing parallel p-orbital interactions that extend conjugation and facilitate delocalization.

Following these material design rules, the visibly transparent photoactive materials can be achieved. They can be thus utilized in light intensity-sensitive and spectrum-sensitive cases. In the former case, there are indoor applications usually operate at low illuminance and consume very low power. Transparent organic photovoltaics have advantages over the inorganic counterpart under indoor light (0.002 to 0.003 sun, 300 to 500 lux) conditions. Organic material has much higher light extinction coefficient and lower dependence of VOC on illuminance. As a result, the device efficiency degradation from outdoor 0.1-0.5 sun (12000 -60000 lux) to indoor light intensity is much lower for the organic module. Besides, the better capability to be embedded into curved or flexible substrates due to the thinner photoactive layer, also makes organic devices more applicable in a wide range of short-life cycle electronics.

In the spectrum-sensitive case, agricultural plants utilize specialized pigments to intercept and capture photon energy for growth. Within the broad solar light spectrum, the photosynthetically active radiation (PAR) activates the chlorophyll a and b pigments, transforming light energy into chemical energy for production of carbon molecules (such as sugars) within 400 to 700 nm. The products are then used to construct more complex compounds, and ultimately plant cells and organs like roots, leafs, stems, flowers, and fruits. In addition to providing energy for plant photosynthesis, light within specific regions also regulates the plant

growth. This process is called photo-morphogenesis, involving the activation of several red light for flowering, for instance.

Consequently, organic solar cells can be designed to capture electromagnetic energy in regions of the spectrum that are not used, or used less predominantly, for photosynthesis and photo morphogenesis. For example, the 500-640 nm section within the visible region is relatively marginal to plant use, which means organic solar cells can be applied to generate additional power in the greenhouse. Therefore, the photovoltaic spectral response can be tuned to use that section of light as well and maximize the total solar energy conversion efficiency.

References

1. Chang, S.Y.; Cheng, P.; Li, G.; Yang. Y. (2018). Transparent polymer photovoltaics for solar energy harvesting and beyond. *Joule* 2(6), 1039-1054.